



Doctoral Thesis

Understanding drought governing atmospheric processes in the Greater Alpine Region

submitted in satisfaction of the requirements for the degree of
Doctor of Natural Sciences
of the Vienna University of Technology, Faculty of Civil Engineering

as part of the
Vienna Doctoral Programme on Water Resource Systems

by

Mag. Klaus Haslinger

Matrikelnummer 0125500

Hochedlingergasse 44, 3550 Langenlois

Examiner: Univ.Prof. Dipl.-Ing. Dr.Techn. Günter Blöschl
Institut für Wasserbau und Ingenieurhydrologie, TU Wien
Karlsplatz 13, 1040 Wien

Examiner: Univ.Prof. Dipl.-Ing. Dr.Techn. Wolfgang Wagner
Institut für Photogrammetrie und Fernerkundung, TU Wien
Gußhausstraße 25-29, 1040 Wien

Examiner: Prof. Christel Prudhomme
European Centre for Medium Range Weather Forecast
Shinfield Rd, Reading RG2 9AX

Langenlois, October 2018

Dissertation

Dürre im Großraum Alpen – Ursachenanalyse atmosphärischer Prozesse

ausgeführt zum Zwecke der Erlangung des akademischen Grades eines
Doktors der Naturwissenschaften
eingereicht an der Technischen Universität Wien, Fakultät für Bauingenieurwesen

im Rahmen des
Vienna Doctoral Programme on Water Resource Systems

von
Mag. Klaus Haslinger
Matrikelnummer 0125500
Hochedlingergasse 44, 3550 Langenlois

Prüfer: Univ.Prof. Dipl.-Ing. Dr.Techn. Günter Blöschl
Institut für Wasserbau und Ingenieurhydrologie, TU Wien
Karlsplatz 13, 1040 Wien

Prüfer: Univ.Prof. Dipl.-Ing. Dr.Techn. Wolfgang Wagner
Institut für Photogrammetrie und Fernerkundung, TU Wien
Gußhausstraße 25-29, 1040 Wien

Prüfer: Prof. Christel Prudhomme
European Centre for Medium Range Weather Forecast
Shinfield Rd, Reading RG2 9AX

Langenlois, Oktober 2018

Abstract

This thesis investigates the emergence of drought events in space and time in the Greater Alpine Region and their atmospheric drivers. The aim is to better understand the precipitation suppressing atmospheric processes on different spatial scales, from regional weather patterns and local feedbacks to the influence of global atmospheric and oceanic modes of circulation. Investigations on this topic have traditionally been based on models and/or relatively short observational data. This thesis goes beyond these studies by using a unique dataset in terms of record length and data quality that consists of climatic data from 1801 to 2010. Analyses of drought events and their atmospheric drivers on such long records provide an opportunity for understanding a broader spectrum of drought events and related drivers and processes. The thesis involves the following tasks: (i) identifying spatial characteristics of droughts on various time scales, (ii) analysing joint spatio-temporal features of droughts and (iii) linking droughts to atmospheric processes.

Considering the long term perspective of more than 200 years of drought patterns in the GAR we find that the time periods of the 1850s to the 1870s and the 1940s were the driest ones. Analyses of spatial clustering on prescribed accumulation time scales (1, 3, 6, and 12 months) of precipitation deficit show that the Main Alpine Ridge is a major climatic divide for droughts, which does not only apply to daily and monthly but also to multi-monthly time scales. The frequency of droughts on different accumulation time scales shows no trends, but rather exhibits multidecadal variations which are more pronounced at higher accumulation time scales. Interestingly, these variations differ in space. The north and west were more drought prone in the middle of the 19th century, whereas the east was in the last decades.

A new method is proposed for detecting atmospheric drought events and their space-time structure that does not prescribe time scales, which is used for analysing the long term evolution of drought frequency, duration, intensity and severity. Our results show variations of these characteristics on multi-decadal time scales, but no trends over the 210 year period are apparent. The 1860s and 1940s stand out as drought rich periods, although the characteristics of individual droughts in these decades are substantially different, indicating different driving mechanisms. Although air temperatures have increased significantly in the past 200 years, we do not find this increase to be significantly correlated with drought duration, intensity or severity. However, we find that dry springs significantly increase temperatures during subsequent summer droughts, which implies a soil moisture-temperature coupling in the warm season.

To finally assess the link between observed drought events and atmospheric processes, a daily atmospheric circulation type reconstruction tailored to the Alpine region and various indices describing major modes of variability in the atmosphere and the ocean are analysed. Our results suggest positive Eastern Atlantic/Western Russia conditions as the main large scale

atmospheric pattern related to anticyclonic circulation and therefore drought in winter and spring, while the North Atlantic Oscillation has no significant impact. In summer a positive soil moisture - precipitation feedback is detected, which is strongest during weak pressure gradient circulation types that favour local convection. The events of the outstanding dry decades of the 1860s and 1940s were triggered by strong precipitation anomalies during spring and enhanced by soil moisture - precipitation feedbacks during summer. The dry springs of the 1860s were caused by circulation characteristics that were quite different from those of the recent decades as a consequence of the last peak of the Little Ice Age and the related large extent of the Arctic sea ice. The dry springs of the 1940s were related to positive sea surface temperature anomalies in the western subtropical Atlantic, triggering distinct Rossby wave trains leading to persistent positive Eastern Atlantic/Western Russia circulation patterns.

Kurzfassung

In dieser Arbeit wird das Auftreten von Dürre in Raum und Zeit im Erweiterten Alpenraum untersucht, sowie deren atmosphärische Treiber auf globaler oder hemisphärischer Skala bis hin zur regionalen Skala. Ziel ist es, das Wissen über niederschlagshemmende atmosphärische Prozesse welche sich auf unterschiedlichen räumlichen Skalen manifestieren (regionale Wetterlagen, lokale Rückkoppelungen mit der Erdoberfläche und globale Ausprägungen atmosphärischer und ozeanischer Zirkulation) zu erweitern. Traditionell basieren derartige Untersuchungen auf Modelldaten und/oder relativ kurzen Beobachtungsdaten. Ein hinsichtlich Qualität und Länge der Aufzeichnungen (1801-2010) einzigartiger Datensatz ermöglicht es, das Verständnis des Auftretens von Dürreereignissen und deren Treiber in der Atmosphäre gegenüber bisherigen Studien erheblich zu erweitern. Folgende Aufgaben werden in dieser Arbeit erarbeitet: (i) Identifikation von Dürreereignissen und ihren räumlichen Eigenschaften auf unterschiedlichen Zeitskalen, (ii) Analyse raum-zeitlich verknüpfter Dürreeigenschaften und (iii) Verschränkung definierter Dürreereignisse mit den atmosphärischen Prozessen.

Im Langfristkontext der letzten 200 Jahre wurden die Zeiträume 1850 bis 1870 und die 1940er Jahre als die trockensten im Alpenraum detektiert. Die Analyse der räumliche Eigenschaften auf vordefinierten Zeitskalen (1, 3, 6 und 12 Monate) zeigt, dass der Alpenhauptkamm eine wichtige klimatische Trennlinie für Dürre darstellt und das nicht nur auf Zeitskalen von Tagen bis Wochen, sondern auch über mehrere Monate hinweg. Kein Trend ist feststellbar bei der Häufigkeit von Dürren, hier sind Veränderungen auf multi-dekadischen Zeitskalen vorherrschend. Es zeigt sich jedoch, dass sich diese zeitlichen Veränderungen auch im Raum manifestieren. So waren Dürren im Norden und Westen des Alpenraums häufiger in der Mitte des 19. Jahrhunderts, wohingegen der Osten eher in den letzten Dekaden betroffen war.

Eine neue Methode zur Detektion von Dürreereignissen und ihrer raum-zeitlichen Struktur wurde entwickelt, um eine Analyse von Trockenheit unabhängig von vordefinierten Zeitskalen durchführen zu können. Damit ist es möglich, die zeitliche Entwicklung von Häufigkeit, Dauer, Intensität sowie Schweregrad von Dürre zu erfassen. Im Verlauf der letzten 200 Jahre zeigen sich multi-dekadische Variationen dieser Eigenschaften aber keine Trends. Die 1860er und 1940er Jahre stechen hervor als sehr trockene Perioden, jedoch unterscheiden sich die Charakteristika der einzelnen Ereignisse erheblich, was auf unterschiedliche Antriebsmechanismen schließen lässt. Obwohl die Lufttemperatur im Alpenraum in den letzten 200 Jahren erheblich angestiegen ist, korreliert dieser Anstieg nicht mit der Dauer, der Intensität oder dem Schweregrad von Dürren. Es lässt sich allerdings eine signifikant höhere Temperatur während sommerlichen Dürren feststellen, wenn das vorangegangene Frühjahr ebenfalls schon durch Trockenheit gekennzeichnet war, was eine Kopplung der Bodenfeuchte mit der Temperatur impliziert.

Um schließlich die Verbindung zwischen beobachteten Dürreereignissen und damit in Verbindung stehenden atmosphärischen Prozessen zu untersuchen wurde eine für den Alpenraum optimierte Wetterlagenrekonstruktion und unterschiedliche, die wichtigsten atmosphärischen und ozeanischen Zirkulationsmoden erfassenden Indikatoren untersucht. Es konnte gezeigt werden, dass die positive Phase des Eastern Atlantic/Western Russia Indikators einen wichtigen großräumigen Einfluss auf Hochdruckwetterlagen in Mitteleuropa hat und deshalb direkt mit Trockenheit im Winter und Frühjahr in Verbindung steht, während die Nordatlantische Oszillation nur geringen Einfluss hat. Im Sommer konnte eine positive Bodenfeuchte-Niederschlags Rückkoppelung nachgewiesen werden, welche am deutlichsten während gradientschwacher Wetterlagen auftritt, die lokale Konvektion begünstigen. Damit in Verbindung stehen die außergewöhnlichen Trockendekaden der 1860er und 1940er Jahre, welche durch extrem trockene Frühjahre gekennzeichnet waren und durch Bodenfeuchte-Niederschlags Rückkoppelung im Sommer verstärkt wurden. Die trockenen Frühjahre der 1860er Jahre haben ihren Ursprung in wesentlich veränderten Zirkulationseigenschaften in Europa als direkte Konsequenz des Höhepunktes der Kleinen Eiszeit in Verbindung mit einer extremen Ausdehnung des Arktischen Meereises. Die trockenen Frühjahre der 1940er Jahre stehen in Zusammenhang mit positiven Anomalien der Meeresoberflächentemperaturen im subtropischen Atlantik, welche Rossby-Wellen generieren, die einem positiven Eastern Atlantic/Western Russia Indikator entsprechen, und dadurch vermehrt Hochdruckeinfluss in Mitteleuropa zur Folge haben.

Acknowledgement

First and foremost I would like to thank my supervisor Prof. Günter Blöschl for his guidance and support, which goes back before the PhD actually started. I am grateful for having the opportunity to work with him and to share his visions and ideas. His scientific expertise, as well as his broader view on sciences and nature was very inspiring for me.

I would also thank my other two mentors Wolfgang Schöner and Franz Holawe who guided me for many years, encouraged me to go on with my scientific career and to believe in what I'm doing. I am convinced, that without their help, this thesis would not have been achieved.

Furthermore, I would like to thank my current and former colleagues and friends at the climate research department at the ZAMG for their support. First and foremost Ivonne Anders, Konrad Andre and Roland Koch who share the office with me and who were therefore immediately confronted with moments of frustration and exhaustion but also with moments of success and joy. I would also like to thank Michael Hofstätter for the many discussions along the way of his and my PhD. A big thank you goes out to the rest of my colleagues for providing an inspiring, supportive and friendly environment which is one most important thing to do good science.

I would like to acknowledge all the data providers, in particular Mikhael Schwander who provided the CAP7 circulation type reconstructions upon personal request, the Climate Research Unit of the University of East Anglia (CRU), the Central Institute for Meteorology and Geodynamics (ZAMG), the European Climate Assessment and Dataset (ECAD) and the NOAA Earth System Research Laboratory.

The Austrian Academy of Sciences, the Austrian Science Fund and the Austrian Climate Research Program is acknowledged for their financial support.

At last but not least I would like to thank my wife Elisabeth, my kids Katharina and Peter and the rest of my family for their love, patience and support throughout this intense time.

Content

- 1. Introduction1

- 2. Spatial characteristics of precipitation shortfalls in the Greater Alpine Region – a data-based analysis from observations4
 - Abstract 4

 - 2.1 Introduction..... 4

 - 2.2 Data..... 6

 - 2.3 Methods..... 8

 - 2.4 Results..... 11
 - 2.4.1 Drought Areas and their severity 11
 - 2.4.2 Spatial Patterns..... 15
 - 2.4.3 Spatial Patterns in time 19

 - 2.5 Discussion..... 20

 - 2.6 Conclusions 22

- 3. Space-time Patterns of Meteorological Drought Events in the European Greater Alpine Region over the past 210 Years24
 - Abstract 24

 - 3.1 Introduction..... 24

 - 3.2 Data..... 26

 - 3.3 Methods..... 28

 - 3.4 Results..... 32
 - 3.4.1 Temporal Evolution of drought characteristics 32
 - 3.4.2 Spatial Patterns..... 36
 - 3.4.3 The drought - temperature nexus..... 38

 - 3.5 Discussion..... 42

 - 3.6 Conclusion..... 44

4. Disentangling drivers of meteorological droughts in the European Greater Alpine Region during the last two centuries	46
Abstract	46
4.1 Introduction.....	46
4.2 Data and Methods	48
4.3 Results.....	54
4.3.1 Drought driver #1: Atmospheric circulation	54
4.3.2 Drought driver #2: Precipitation efficiency.....	57
4.3.3 Similarities and differences of the drought decades of the 1860s and 1940s	61
4.4 Discussion.....	66
4.4.1 General remarks.....	66
4.4.2 Implications for understanding future climate change	69
4.5 Conclusions	70
5. Summary and Conclusions	72

1. Introduction

Droughts are among the main processes causing climate-related damage to human systems including agriculture, water supply and energy production. Droughts also strongly impact on the environment and can severely damage ecosystems. Recent droughts have demonstrated such devastating effects. A severe drought hit Central Europe in the summer of 2003 causing agricultural damage on the order of € 15 Billion (De Bono et al., 2004). More recently, the drought in Europe in 2015 (van Lanen et al., 2016) and the droughts in the United Kingdom in the winters of 2010 and 2012 (Kendon et al., 2013) also caused immense damage in various societal sectors.

In contrast to other climate related hazards such as floods and thunderstorms, which develop on relatively short time scales of hours to days, drought is a phenomenon that evolves over a much longer time scale of weeks, months or even years. A drought event starts as a meteorological drought, expressed through precipitation deficit, which is a negative anomaly relative to a defined reference period, for a given time span. A prolonged meteorological drought leads to an agricultural drought, which relates to a soil moisture deficit. An agricultural drought occurs if soil moisture falls below a critical threshold and plants start to suffer from water stress. Persistent agricultural drought then gives rise to the formation of a hydrological drought when the atmospheric drought signal of lacking precipitation reaches streamflow and reservoir storage resulting in low flow and empty reservoirs. Hydrological drought is of course linked to the atmospheric drivers, although the signal is dampened and perturbed when propagating through the terrestrial part of the hydrological cycle (see Haslinger et al., 2014).

In order to reach this rather extreme stage of hydrological drought, a meteorological drought has to persist over a considerable time span to carry the signal all along through the hydrological cycle to reach streamflow. Persistence of precipitation suppressing atmospheric patterns is therefore key to understanding the evolution of droughts over time. Although there are different drought stages as denoted above, this thesis focusses explicitly on meteorological drought, all other stages involve land surface processes (evapotranspiration) which may only have indirect influence on the atmospheric controls regarding precipitation deficit.

There are many studies in the scientific literature assessing the temporal variability and trends of drought conditions on global (Dai, 2011; Sheffield and Wood, 2008), continental and regional scales (Lloyd-Hughes and Saunders, 2002; Spinoni et al., 2015 are two examples in Europe). However, these investigations have generally aimed at a broad assessment of dryness and wetness, and did not focus on single events and their potential drivers. On the other hand, there are many studies that thoroughly describe the driving processes of single drought events, for example the Central European drought of 2003 (Black et al., 2004), the drought that affected the Iberian Peninsula in 2004/2005 (García-Herrera et al., 2007) and the European summer drought of 2015 (Ionita et al., 2017; van Lanen et al., 2016), yet assessments on a larger

sample of events are rather sparse. Furthermore, drought or low flow indicators have been linked to atmospheric patterns in Europe, but mostly only for distinct regions such as France (Giuntoli et al., 2013) and Hungary (Pongrácz et al., 2003). Both studies focused on large scale patterns and demonstrated the existence of a link between atmospheric or oceanic modes such as NAO or ENSO and droughts in their region of interest. Fleig et al. (2010) related hydrological drought occurrence to weather patterns in Denmark and the UK, but the aim of their study was to identify the most suitable weather type classification rather than gaining process understanding on the atmospheric conditions of drought.

There is a considerable body of literature on the long term climate variability in the Greater Alpine Region (GAR, Auer et al., 2007), such as Böhm (2012), Brunetti et al. (2009) and Auer et al. (2005) as well as on soil moisture variability (van der Schrier et al., 2007) and large scale drivers of climate variability (Efthymiadis et al., 2007). However, a large sample of individual drought events in the GAR during the last two centuries has not been investigated yet to understand their relationship to atmospheric forcing on different spatial and temporal scales. In this respect the GAR constitutes an ideal test region, since the HISTALP database (Auer et al., 2007) entirely covers the GAR and provides high quality, homogenized station-mode and grid-mode data covering the period of 1760-2010 which makes HISTALP a worldwide unique database regarding record length and data quality. Analysing long records in the GAR with respect to drought drivers therefore promises a substantial increase in the understanding of drought evolution and drought drivers.

There is another reason why the GAR is an ideal test bed for investigating meteorological drought drivers. The GAR comprises a rather diverse climatological setting between the Mediterranean and Central Europe with different precipitation regimes and trends (Haslinger et al., 2012; Brunetti et al., 2006), bearing the chance to generate astonishing dipoles between wet and dry areas. This was most recently the case in winter/spring of 2014 where the north-eastern parts of the GAR experienced an outstanding drought and the southern rim of the Alps experienced record-breaking precipitation. The drivers of climate and particularly precipitation in the GAR are manifold as they involve Atlantic influence, continental climate regimes as well as Mediterranean influence, resulting in highly diverse climatological patterns.

The overall aim of this thesis is to assess the emergence of meteorological drought in space and time and to gain a better understanding of drought inducing atmospheric processes across multiple scales in the Greater Alpine Region over the last two centuries. First of all, multiple climatic influences are explored to reveal the characteristics of drought in spatial, temporal and seasonal terms. Based on these findings a broader assessment of the atmospheric controls of drought development is examined. The main hypothesis is that droughts are forced on multiple scales through persistent atmospheric conditions which may be steered by large scale atmospheric and oceanic circulation patterns, and by locally induced feedback mechanisms. This work will furthermore shed light on the potential influences of large scale drivers on the propensity for dry conditions which may favour the build-up of an excessive drought event. To this end, the exceptionally dry decades of the 1860s and 1940s are investigated to reveal the

drought drivers in these two periods which had considerable impact in the GAR. For example, the last time Lake Neusiedl, a large steppe lake at the Austrian-Hungarian border, fell dry was between 1864 and 1870. Understanding the processes and atmospheric forcings of individual events and distinct periods is highly relevant in the context of global climate change and possibly altered climate conditions in the future. The Special Report on Extreme Events (SREX; IPCC, 2012) emphasised that there is only medium confidence in increasing droughts in Europe, so enhancing our knowledge of the atmospheric processes driving droughts in the GAR is of essence.

Following the general aims of this study, three main research topics are addressed, each involving a number of specific aims:

1) Spatial patterns of precipitation deficit

- (i) Detecting areas under drought using accumulated precipitation on different time scales and quantifying the drought severity of the area
- (ii) Assessing similarities of these drought areas to obtain the main drought patterns
- (iii) Investigating possible changes of drought patterns over the past 200+ years

2) Space-time emergence of drought events

- (i) Developing a new method of space-time drought event detection
- (ii) Analysing the temporal evolution of drought event characteristics (duration, intensity, severity) in the GAR over the past 210 years
- (iii) Analysing the spatial patterns of droughts as a function of severity and duration
- (iv) Investigating the influence of recent air temperature increases on the three main drought characteristics

3) Atmospheric drivers of drought events

- (i) Quantifying the relationship between precipitation deficit during drought events and atmospheric circulation anomalies on a daily basis
- (ii) Evaluating seasonal differences between atmospheric forcing and soil moisture feedbacks
- (iii) Understanding the atmospheric drivers of the exceptionally dry decades of the 1860s and 1940s
- (iv) Assessing these in the context of possible future climate change

2. Spatial characteristics of precipitation shortfalls in the Greater Alpine Region – a data-based analysis from observations

Abstract

In this chapter, we investigate spatial patterns of meteorological drought events in the Greater Alpine Region (GAR) of Europe. A long term gridded dataset of monthly precipitation sums spanning the last 210 years is used to assess abnormally dry states using a shortfall below a monthly precipitation percentile threshold. These anomalies are calculated for 1, 3, 6 and 12 monthly moving averages. Contiguous areas of grid points below the threshold are indicating drought areas which are analyzed with respect to their drought severity. The severity is quantified by taking the average deviation from the threshold and the size of the drought area into account. The results indicate that the most severe dry anomalies in the GAR occurred in the 1860s, 1850s and the 1940s. However, no significant trends of dry anomaly severity are found over the last 210 years. A spatial clustering analysis of the detected drought areas shows distinct spatial patterns, with the Main Alpine Crest as a frequent divide between dryer areas in the North and wetter areas in the South, or vice versa. The patterns are highly significant and similar for all averaging time scales. The clusters are more clearly defined in winter than in summer. Droughts in the North are most frequent in the second half of the 19th century, while in the South and East they are most frequent in the late 20th century.

2.1 Introduction

From a first snapshot the Greater Alpine Region (GAR, Auer et al., 2009) is a water-rich area, exhibiting annual precipitation totals from 400 to even beyond 3000 mm/year (Isotta et al., 2014). However, water scarcity is a serious issue in some parts of the area in some years which may cause substantial threats to drinking water supply, irrigation water supply, energy production (through cooling water and hydropower generation) and river navigation.

Within the last decades several droughts struck large parts of Europe and the GAR (Spinoni et al., 2015; Hoerling et al., 2012; Parry et al., 2012; Bradford, 2000; van der Schrier et al., 2006), e.g. the summer droughts of 2003 and 2015 as two of the most recent occurrences. They were caused by prolonged periods with below average precipitation which led, in combination with high temperatures, to severe drought related impacts (van Lanen et al., 2016; García-Herrera et al., 2010) not only in the GAR, but in large areas across Europe. However, not only in the warm season has an accumulated precipitation deficit has large impacts on society. In the Alps winter sports are a major economic branch, depending heavily on sufficient snowfall in winter.

A succession of three extremely dry winters in a row (1987/88 to 1989/90) substantially affected winter tourism (Abegg et al., 2007). Additionally, there is a close link between winter precipitation (e.g. via melt of the snow pack) and flow characteristics of rivers with a snow covered catchment during summer since insufficient snow pack might trigger low flows in the warm season downstream (Jenicek et al., 2016; Nester et al., 2012; Parajka et al., 2008). Especially a deficit of accumulated precipitation during winter may lead to low flow events of such rivers (Parajka et al., 2016).

Besides any formal way to calculate any kind of indicator the term drought itself must be clarified. For example Wilhite and Glantz (1985) discusses the issue of drought severity extensively and identifies four types of drought: meteorological, agricultural, hydrological and socioeconomic drought. Within this chapter, we focus on meteorological droughts (precipitation deficit) as they trigger all other drought types (van Loon, 2015; Stagge et al., 2015; Haslinger et al., 2014). Several studies have investigated long-term precipitation characteristics and change in the GAR, e.g. the studies of Brunetti et al. (2006, 2009) and Auer et al. (2005), who found increasing trends in precipitation north of the Alps and slightly decreasing trends south of the Alps from 1800 to 2003. These trends are connected to a dipole like feature of precipitation from North to South which strengthened somewhat over the past 200 years. Additionally, they reported a slight shift in precipitation seasonality with positive trends in winter and spring, counteracted by negative trends from July to November.

Brunetti et al. (2006) also analysed spatial patterns of precipitation in the GAR, based on Principal Component Analysis (PCA) of the precipitation time series. They found four homogeneous sub-regions in the GAR in terms of their inter-annual precipitation variability. The PCA of Brunetti et al. (2006) uses all the data of the probability distribution of precipitation, thus that patterns for the dry tail of the distribution might look different. Van der Schrier et al. (2007) investigated soil moisture variability in the GAR, based on the self-calibrating Palmer Drought Severity Index (scPDSI, Wells et al., 2004). They used the previously defined sub-regions of Brunetti et al. (2006) regionalization to assess dry and wet episodes. Van der Schrier et al. (2007) left it open whether the predefined sub-regions are suitable for a dry episodes analysis.

Several studies investigated spatial and temporal patterns of drought occurrence globally or in other regions of the world. General assessments of drought characteristics and trends from global data sets are given for example in Sheffield and Wood (2008), Trenberth et al. (2014) or Dai (2011) highlighting regional differences in drought trends and large uncertainties considering the input data but on average increasing trends due to increased evapotranspiration. Spatial patterns of droughts on a global scale are investigated for example by Sheffield et al. (2007) or Spinoni et al. (2014). Particular interest on spatial patterns on a regional scale was given by Soulé (1990) who analyzed various kinds of the Palmer Drought Severity Index through a PCA for the United States. The results showed more regions with smaller extent for faster responding indices (e.g. Palmer's Z-Index) and less individual regions with larger extent for slower reacting indices (e.g. Palmer Hydrological Index), which implies

that the spatial characteristics are dependent on the time scale of the droughts. Similar results were found for the Iberian Peninsula by Vincente-Serrano (2006) who conducted an analogous analysis based on the Standardized Precipitation Index (SPI, McKee et al., 1993) comparing different accumulation time scales from 1 to 36 months. Other examples are Cai et al. (2015) who performed a regionalization of drought characteristics based on a modified version of the Reconnaissance Drought Index (RDI, Tsakiris and Vangelis, 2005) for the Beijing-Tianjin-Hebei metropolitan areas, and the work of Patel et al. (2007) who investigated spatial drought patterns based on the SPI in the region of Gujarat (India).

From the existing literature no complete picture can be drawn on the spatial patterns of meteorological drought in the GAR. The most comprehensive work on drought in the GAR conducted by van der Schrier et al. (2007) did not analyze the spatial aspects of observed droughts. Consequently, an investigation of drought patterns in the GAR is still missing. Yet the GAR provides the possibility to investigate the spatial dimension of drought in a world-wide unique long term (200+ years) assessment, enabling to investigate spatial patterns of droughts and changes of those over the last two centuries. Particularly considering global climate change it is of utter importance to enhance our understanding of past droughts to better assess possible future developments. Stepping into these detected research gaps we aim to analyze the long term (200+ years) characteristics of drought patterns in the GAR. The more specific aims of this chapter are (i) to detect areas under drought using accumulated precipitation on different time scales and to quantify the drought severity of the area; (ii) to assess similarities of these drought areas in order to obtain main drought patterns and (iii) to investigate possible long term changes of drought patterns over the past 200+ years.

2.2 Data

The spatial domain of this investigation is the European Greater Alpine Region (GAR, Auer et al., 2001) which stretches from 4°-19°E and 43°-49°N (Figure 2.1). The GAR is known for high quality, long term climate information back to 1760, the so called HISTALP database (Böhm et al., 2009). In this chapter gridded data of monthly precipitation sums covering the whole GAR are used. This dataset was created by Efthymiadis et al. (2006) by gridding the available HISTALP stations with precipitation measurements, which are at maximum density nearly 200 stations. For the purpose of this chapter, the data set was updated until 2010 using similar techniques as for the original dataset described in the following section. The data set therefore covers the period 1801-2010. It has a spatial resolution of 10', which is roughly 15 km.

The gridding is performed by the “anomaly approach” (e.g., Jones et al., 1996), which splits the precipitation field in two components. One is the long term mean component, the climatology fields. Efthymiadis et al. (2006) used a high resolution monthly precipitation climatology of the ETH Zürich (Schwarb, 2000) from 1971-1990 which utilizes a very dense station network in order to capture the complex spatial features of precipitation in the GAR. The second component is the anomaly field. It is derived by interpolating station anomalies

relative to the averaging period of the climatology (1971-1990) using the angular distance weighting approach. The combination of the high resolution climatology and the smoother anomaly fields yields the final absolute precipitation fields. However, it should be noted, that only stations up to 2000 m.a.s.l. are used, thus uncertainties of the gridding in the high elevated areas of the GAR should be kept in mind.

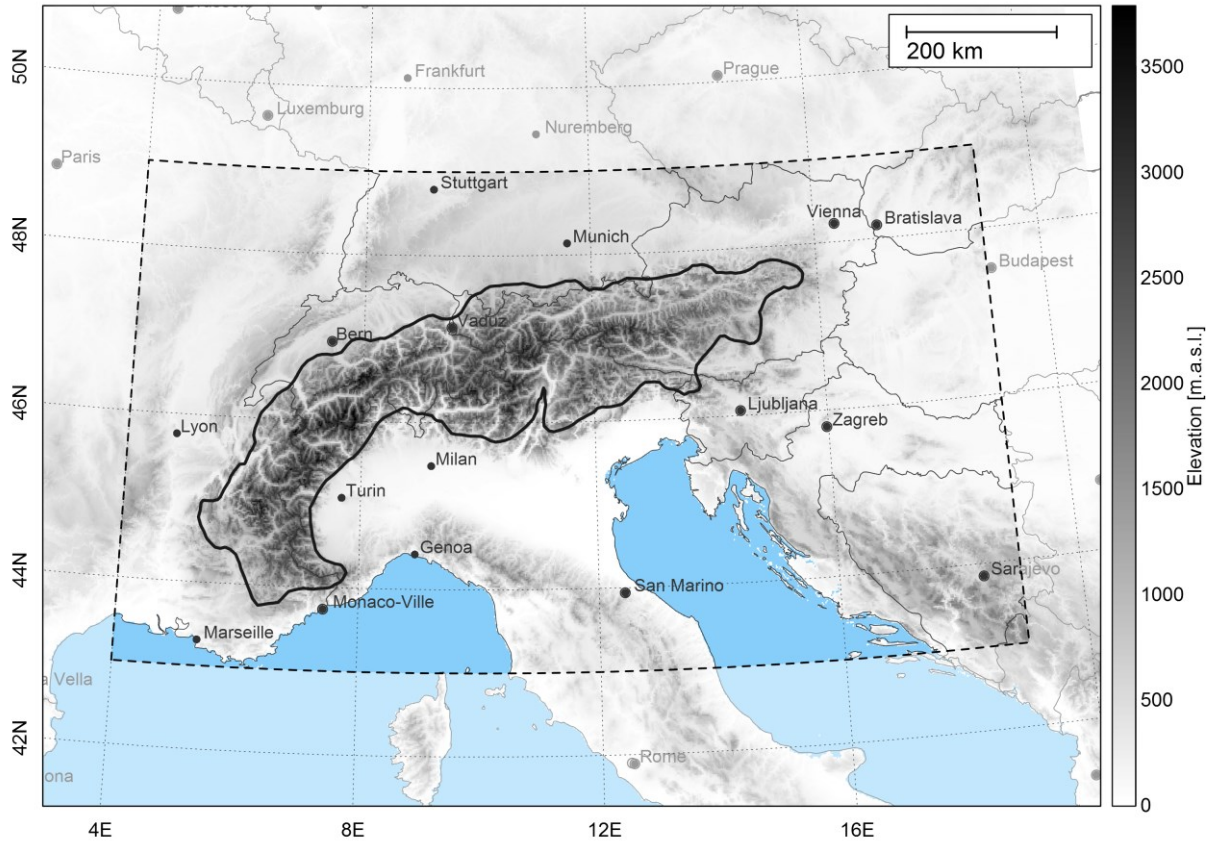


Figure 2.1. Map of Central and Southern Europe; the broken line indicates the boundaries of the Greater Alpine Region, the solid line represents a generalized outline of the 1000 m a.s.l. isoline of the Alps which should help locating the mountainous areas of the domain in the following figures.

In this chapter, we use the gridded precipitation data to assess abnormally dry states in space which could subsequently lead to soil moisture, streamflow or groundwater drought. To account for the different time scales on which these effects may arise, the precipitation values are summed up by a moving window approach over a 3 month (3M), a 6 month (6M) and a 12 month (12M) time scale, similar to the procedure to calculate the Standardized Precipitation Index (SPI) on different accumulation time scales (see McKee et al., 1993).

2.3 Methods

Depending on the available data, different approaches have been used so far to depict drought (Zagar et al., 2011; Mishra and Singh, 2010; Heim, 2002; Wilhite and Glantz, 1985). During the last decades especially three indices are in use for research and operational applications, the Palmer Drought Severity Index – PDSI (Palmer, 1965) the Standardized Precipitation Index – SPI (McKee et al., 1993) and the Standardized Precipitation Evapotranspiration Index – SPEI (Vincente-Serrano et al., 2010). The SPI can be calculated from precipitation data alone, for the calculation of the PDSI and SPEI potential evapotranspiration (PET) would be required. We intentionally do not use the PDSI or the SPEI, because (i) the incorporation of a temperature based PET (other variables are not available for the GAR for this time period) introduces additional uncertainty (e.g. Sheffield et al., 2012) and (ii) we are interested in understanding the spatial patterns of precipitation deficit, investigating the climatic water balance would introduce more aspects and processes e.g. land-atmosphere interaction which might obscure the original intensions.

Instead of using the SPI we use precipitation quantiles on four different accumulation time scales (1, 3, 6 and 12 months) to quantify meteorological drought conditions in the GAR. Quantiles introduce a lower boundary (zero), which makes a severity assessment, as described below, much more straight forward. As highlighted by Naresh Kumar et al. (2009) the SPI underestimated the severity of dry and wet extremes due to distribution fitting issues which underpins the advantage of using quantiles.

The procedure to identify dry areas is displayed in Figure 2.2. Figure 2.2a shows an example of a precipitation field, the December of 1829. The spatial patterns of this field are characterized by low precipitation in the Northwest of the domain, well below 50 mm/month. In contrast, in some coastal areas of Croatia precipitation sums exceed 300 mm/month. In the same manner as for calculating the SPI, a Gamma-distribution (Wilks, 2011) is fitted to the time series at every grid point. The parameters of the distribution are individually estimated for all the Januaries, Februaries and so on, and repeated for all three accumulation time scales. This procedure ensures comparability of anomalies across seasons, independent of the climatological mean of the precipitation sum.

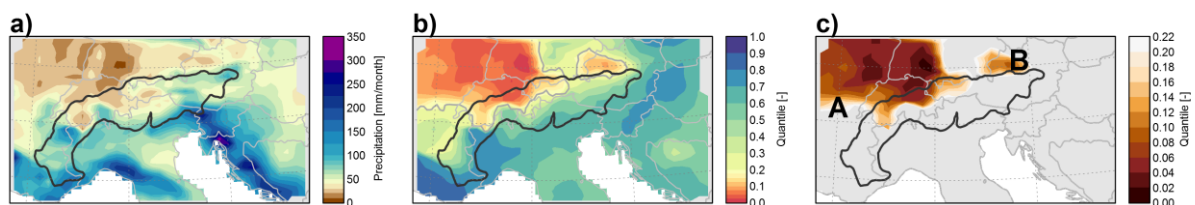


Figure 2.2 Example of a precipitation field of December 1829 (a), the corresponding quantiles; the grey contour line represents the 20th percentile (b) and the detected contiguous drought areas at that particular time step A and B (c).

From the estimated Gamma distribution the precipitation values (e.g. for the example of 1829 in Figure 2.2a) are assigned to percentile values (Figure 2.2b). Obviously, regions in the Northwest faced rather low values, well below the 10 % percentile, indicating a relatively unusual month. As a next step, a threshold of the percentile values is determined to separate dry areas from non-dry areas. We chose the 20 % percentile, which is a widely used threshold for drought identification (e.g. Svoboda et al., 2002). The threshold is indicated as a grey outline in Figure 2.2b. As a next step, all spatially neighboring grid points below the threshold are aggregated to regions, which we term Drought Areas (DAs). In Figure 2.2c two identified DAs, A and B, of December 1829 are displayed. All key-attributes of a detected DA are summarized by a lookup table covering the region ID, the grid point IDs, longitudes, latitudes, quantile values and the month and year of occurrence. For further analysis throughout the chapter we use only DAs with a minimum size of 20% relative to the whole GAR.

For our study the affected area of a drought by itself is an important drought measure. Therefore we decided to define also the severity of a detected drought area by scaling the mean deviation from the threshold level by the number of affected grid points. The severity of a DA is given by equation (2.1)

$$S = \sum_{i=1}^n (-1(q_i - t)) / t \quad (2.1)$$

where S is the Severity which is a dimensionless measure, n is the number of all grid points i, detected within a DA, q is the quantile value and t the threshold (fixed at 0.2). This implies that the severity is higher, if either the DA or deviation from the threshold is large. Highest severities are given, if the DA as well as the threshold deviation is large.

In Figure 2.3 examples of four individual DAs are displayed. Figure 2.3a shows a meteorological drought on a 1M time scale in February 1814, affecting mostly the southern part of the GAR. The affected area is rather large, while the mean quantile value is rather low (0.077), resulting in a larger value of the overall Severity of 982. In contrast, the DA from February to April 1930 (Figure 2.3b, 3M time scale) is considerably smaller, impacting mostly the western part of Austria. In combination with a mean quantile value of 0.125, the Severity is only 39. However, this DA is not considered in the further analysis since it is below our chosen area threshold (20% of the GAR). Another example with large spatial extent, but low mean quantile deviation from the threshold is displayed in Figure 2.3c. This DA on a 6M time scale (May-October 1822) covers large areas in the East, but the mean quantile value is 0.141, yielding a Severity of 299, which is considerably lower than the Severity of February 1814 (Figure 2.3a). A last example, for the 12M time scale, shows the DA from July 1954 to June 1955 in Figure 2.3d. The spatial extent is not large, but the mean quantile value is low, which gives a Severity of 258, comparable to the Severity in Figure 2.3c, but affecting not nearly half of the area. Some guidance on the probability distribution of the Severity is shown by Table 2.1 which displays the Severity values associated with certain quantiles. In general the Severity is somewhat decreasing with higher accumulation time scale. The median ranges between 648

and 571, whereas the 95% quantile lies between 1879 and 1621. There is indeed a theoretical upper bound of the Severity which relates to the size of the grid. If all the grid points would show no precipitation at all at a given time step, equivalent to a quantile value of zero, the Severity would be 2895, which is the number of all land surface grid points in the GAR.

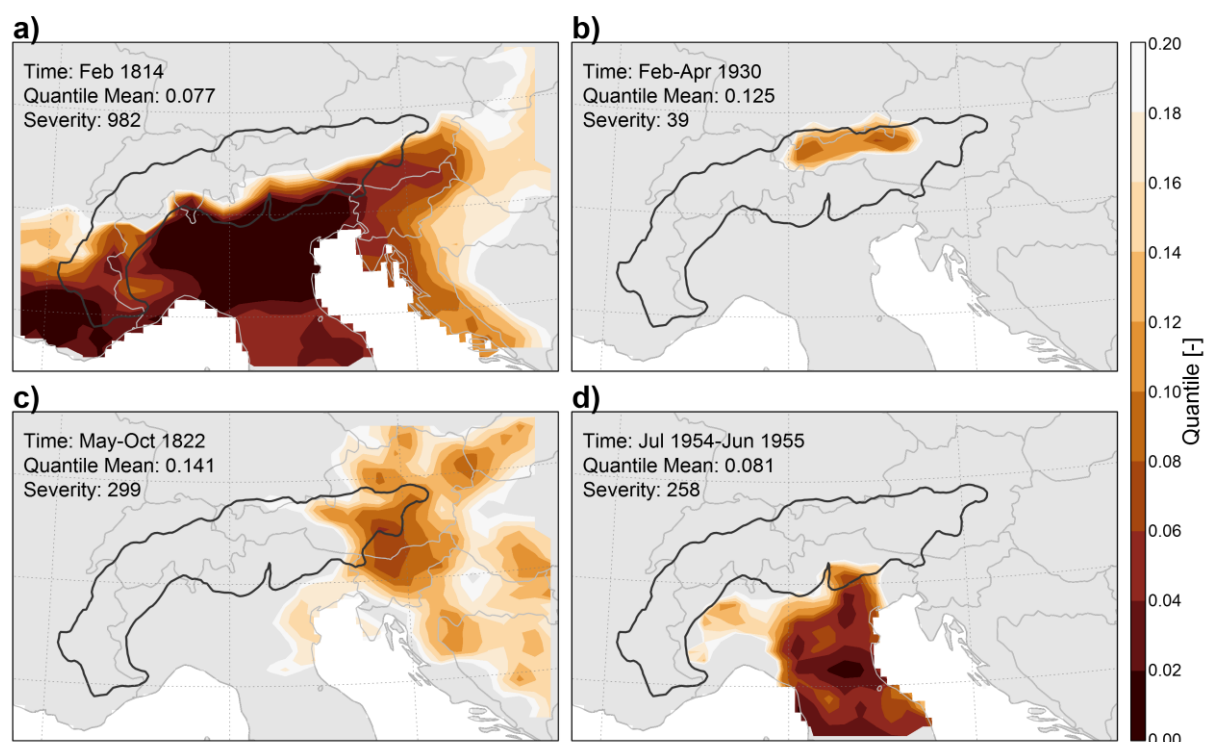


Figure 2.3 Four examples of DAs on a 1 month (a), 3 months (b), 6 months (c) and 12 months (d) time scale. Every DA is described through four attributes exemplarily: a time period of occurrence (Time), the quantile mean of the DA and the Severity.

Table 2.1 DA Severity associated with different quantiles stratified by accumulation time scale

Percentile	Severity			
	1 Month	3 Months	6 Months	12 Months
50 %	648	604	583	571
80 %	1160	1112	1040	960
90 %	1557	1437	1335	1285
95 %	1879	1699	1629	1621

The main methodological framework of this investigation is the clustering of spatial patterns of DAs in order to gain information on the spatial behavior of meteorological drought. We identify similarity patterns of DAs by a k-means clustering approach. We use the monthly DA-fields, where all grid points with percentile values outside the 0-0.2 range are set to zero, in order to avoid biases arising from prominent wet features in space, and all grid points below

the threshold boundary are set to one. Within the k-means approach, Euclidian distances (Wilks, 2011) between data points are calculated, which are matrices with binary information on drought (one) and no drought (zero). The distances are iteratively minimized through the sum-of-squares criterion for a previously defined number of clusters (Bishop, 1995). The crucial part of the clustering algorithm is the determination of an optimal number of clusters. In this chapter we use the silhouette width approach (Rousseeuw, 1986) which describes the similarity of an object to the assigned cluster as well as the dissimilarity to all other clusters. It ranges between -1 and +1, with higher values indicating better clustering solutions. The significance and stability of a given clustering solution is assessed through the Clustering Stability (Hennig, 2007) approach.

2.4 Results

2.4.1 Drought Areas and their severity

Figure 2.4 shows the top 100 DAs in terms of their severity, stratified by the accumulation time scale. The DAs cluster around the middle of the 19th, as well as the 20th century and in the 1890s if only the 1M time scale is considered. On a 1M time scale 13 DAs of the topmost ones are detected in the 1860s, 9 in the 1850s and 8 in both the 1920s and 1940s. Decades with rather low numbers of extreme DAs are the 1820s (0 DAs) and the 1810s (1 DA) for example. Time periods of prolonged dry conditions are revealed considering higher aggregation levels. On a 3M and 6M time scale the 1940s show highest DA occurrence (12 and 16 DAs respectively), followed by the 1920s on a 3M time scale with 9 DAs and the 1860s on a 6M time scale with 13 DAs. On a 12M time scale, the 1830s (20 DAs), 1850s (18 DAs) and the 1860s (17 DAs) are identified as periods of maximum drought occurrence.

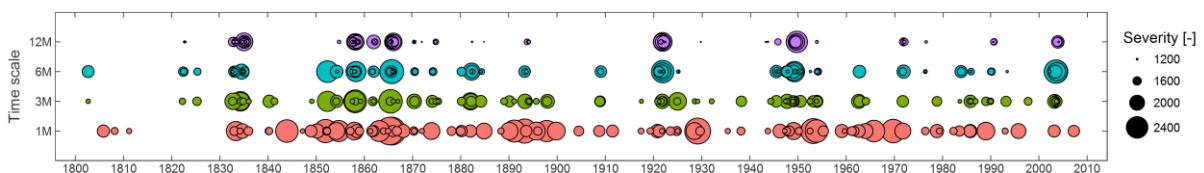


Figure 2.4 Time of occurrence and magnitude of the top-100 Drought Areas (DAs) at different time scales (indicated by different color shading); the size of the circles indicates the severity of the event.

It should be noted that, as an additional effect of using moving averages of the monthly precipitation sums in the time domain, DAs tend to cluster around similar years for different time scales. This is apparent mostly for the 12M line in Figure 4. For example, the outstanding DA of October 1949 is surrounded by other, but smaller DAs along time.

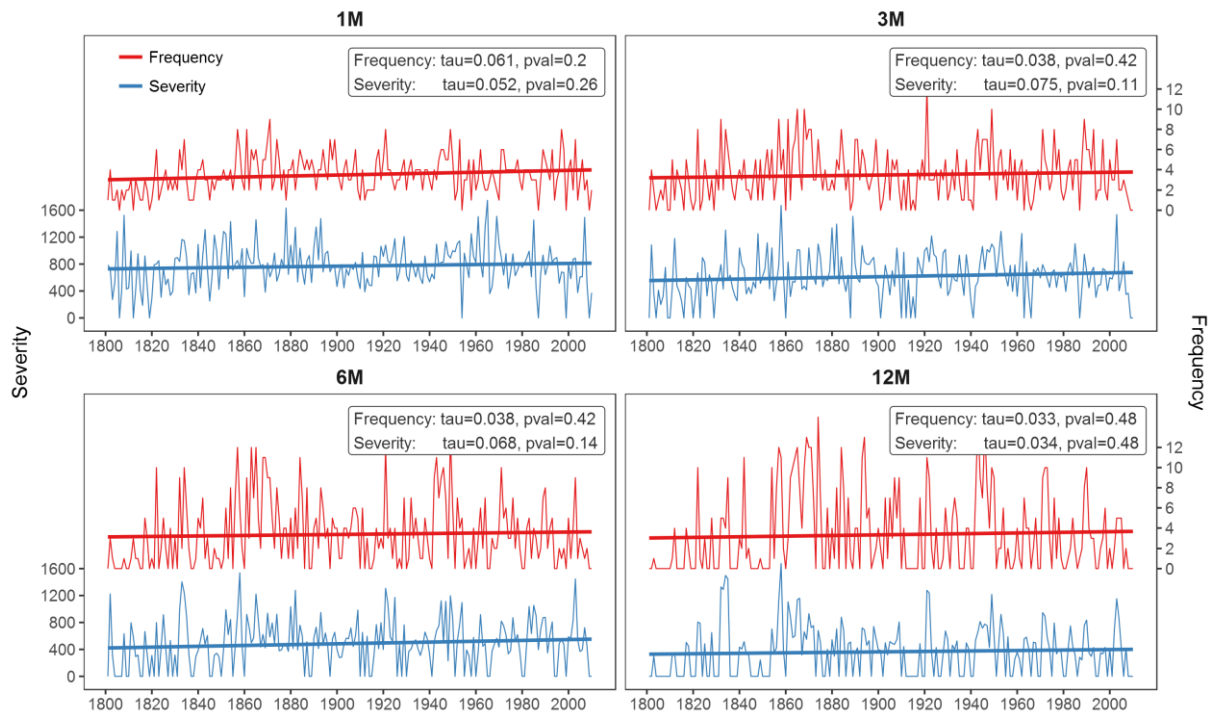


Figure 2.5 Time series of annual averages of DA Severity (blue) and Frequency (red) stratified by accumulation time scale and the estimated trend line; respective values of Kendall's τ and the significance of the trend given by the p-value are given in the upper right corner.

The presented occurrence diagrams in Figure 2.4 show a distinct decadal to multi-decadal scale variability of DA frequency. However there is no apparent trend in the occurrence of droughts. We analysed time series of annual averages of DA severity and frequency using the non-parametric Mann-Kendall trend test for estimating the significance of the trend in the given time series. Since the accumulation procedure might introduce autocorrelation in the time series these were pre-whitened before significance assessment. As can be seen in Figure 2.5 both the frequency and the severity show in general no significant trend, no matter what time scale is considered with p-values ranging between 0.11 and 0.48.

Table 2.2 lists the top 5 DAs in terms of their Severity per time scale. The overall driest month on record was September 1865, followed by April of the same year. This DA affected 99.5 % of the whole GAR and shows an average precipitation anomaly of -90 mm which equals 9% with respect to the long term (1801-2010) mean. The overall deficit volume in this particular month is 61 km³ of water. The driest 3M period was April to June, again in 1865. The area under dry conditions covers 98.4 % and the overall precipitation anomaly is -144 mm, resulting in a deficit volume of 97 km³. The second and third driest 3M periods occurred in winter 1857/1858, with similar precipitation anomalies of -139 and -152 mm respectively. Also on a 6M time scale the year of 1865 reaches the top position with the period from April to September. Within these 6 months, only 60 % of average precipitation was observed, resulting in a deficit volume of 158 km³. On ranks two and three a more recent event is recorded, namely the time from February

to August 2003, with a deficit volume of nearly 150 km³. Considering a 12M time scale the driest period occurred from November 1948 to October 1949, followed by the time from January to December in 1921. Both show similar deficit volumes of 240 and 241 km³, respectively.

Table 2.2 Characteristics of the top-5 Drought Areas (DAs) per accumulation time scale

Time scale	Time period	Severity	Affected area	Mean percentile value	Absolute Anomaly	Relative Anomaly	Deficit volume
		[-]	[%]	[-]	[mm]	[%]	[km ³]
1 Month	Sep. 1865	2782	99.5	0.007	-90	9	61
	Apr. 1865	2765	100.0	0.009	-73	14	50
	Mar. 1929	2663	100.0	0.016	-61	14	42
	Mar. 1953	2602	97.7	0.016	-63	12	42
	Apr. 1893	2556	96.0	0.016	-71	16	46
3 Months	Apr.-Jun. 1865	2520	98.4	0.023	-144	50	97
	Dec. 1857-Feb. 1858	2477	97.2	0.024	-139	36	93
	Nov. 1857-Jan. 1858	2342	98.0	0.035	-152	41	102
	Mar.-May 1852	2315	100.0	0.040	-119	53	82
	Feb.-Apr. 1834	2278	99.6	0.042	-121	45	83
6 Months	Apr.-Sep. 1865	2546	99.4	0.023	-232	60	158
	Feb.-Jul. 2003	2505	99.4	0.026	-214	59	146
	Mar.-Aug. 2003	2504	97.8	0.023	-219	60	148
	Jul.-Dec. 1921	2449	99.0	0.029	-264	55	180
	Dec. 1851-May 1852	2403	100.0	0.034	-206	56	142
12 Months	Nov. 1948-Oct. 1949	2389	98.7	0.022	-376	65	240
	Jan.-Dec. 1921	2229	90.1	0.029	-389	64	241
	Feb. 1852-Jan. 1835	2174	92.1	0.037	-347	68	220
	Feb. 1865-Jan. 1866	2156	91.4	0.037	-325	70	204
	Nov. 1920-Oct. 1921	2107	90.4	0.039	-347	68	216

Considering drought occurrence stratified by seasons, somewhat different patterns are observed as can be seen in Figure 2.6. We defined the cold season (warm season) as the half year spanning October to March – ONDJFM (April to September – AMJJAS). In addition, we considered the core season within these half years: winter (DJF) and summer (JJA). DAs in the cold season are clearly more likely in the second half of the 19th century, although the biggest event on a 1M time scale occurred in March 1929 and on a 6M time scale in March 1949. The decades with the highest number of DAs in the cold season are the 1850s on a 1M time scale (6 DAs), the 1880s on a 3M time scale (7 DAs) and the 1850s, 1880s, 1890s and 1970s on a 6M

time scale. The warm season experiences most DAs in the 1940s on a 1M time scale (7 DAs), in the 1920s on a 3M time scale (9 DAs) and in the 1860s on a 6M time scale (8 DAs). Considering the core season winter and summer, the patterns are similar. In winter (DJF) DAs are most frequent in the 1850s and 1860s on a 1M time scale (6 DAs) and in the 1850s on a 3M time scale (6 DAs). In summer (JJA) the 1850s and 1940s show highest frequency of DAs on a 1M time scale (6 DAs), whereas the 1860s, 1920s and 1940s show the highest number of DAs on a 3M time scale (5 DAs).

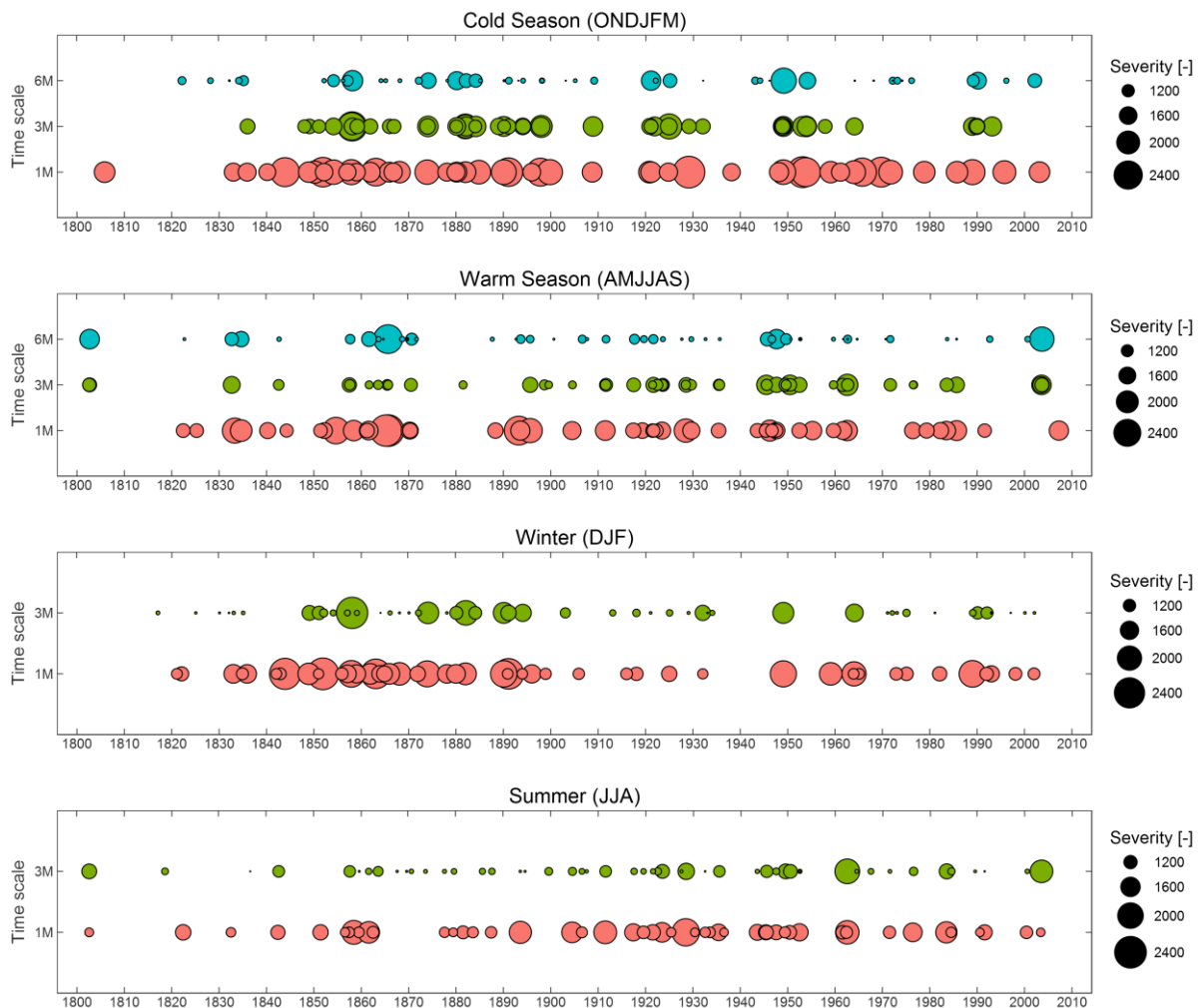


Figure 2.6 Time of occurrence and magnitude of the top-50 Drought Areas (DAs) at different time scales (indicated by different color shading) stratified by season; the two top most panels show the DAs in the half-years (cold season ONDJFM and warm season AMJJAS), the two bottom most panels show the DAs in seasons (winter DJF and summer JJA); the attribution of a DA to a distinct season follows strictly their defined boundaries, for example 6M DAs in the cold season are only those detected in March, since the 6M time scale refers to an accumulation from October to March; for this reason there are only three time scales displayed in the half-year plots and two time scales in the seasonal plots.

2.4.2 Spatial Patterns

In this section the spatial patterns of DAs are analyzed using a k-means clustering approach. The aim is to allocate every detected DA (c.f. Figure 2.3) to a cluster of DAs with similar spatial properties. The result of the k-means clustering is a flag for the DAs indicating their spatial affiliation; e.g. all DAs covering the Northwest of the GAR are assigned to the same cluster.

As described in the Methods section the optimal number of clusters has to be defined beforehand, which is carried out with the silhouette width approach (Rousseeuw, 1987).

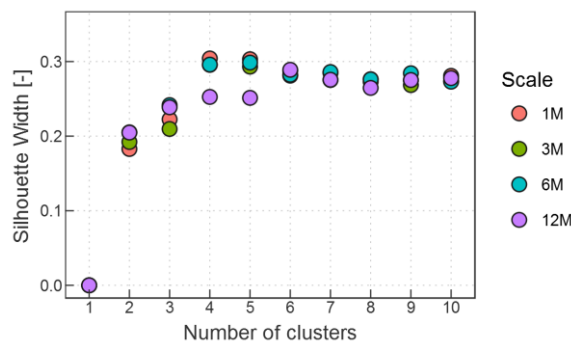


Figure 2.7 Silhouette widths for different cluster solutions and different time scales of the DAs.

Figure 2.7 shows the silhouette width of different clustering solutions stratified by different time scales. First of all, silhouette widths of the clustering on different time scales is rather similar. If averaged over all time scales the peak is at 4 clusters with silhouette widths of 0.30 for the 1M, 3M and 6M time scales and 0.25 for the 12M time scale (c.f. Table 2.3) indicating optimal clustering with 4 clusters. These values can be interpreted, following Kaufmann and Rousseeuw (2005), as “weak structures which may be artificial”, which is consistent with the present analysis, since the objects for the clustering are binary fields which may overlap to some degree, but may be assigned to different clusters. For further analysis we choose four clusters. To further assess the quality of the clustering solution we calculated the Cluster Stability (Hennig, 2007). In this approach, the data is resampled by a bootstrapping approach and the similarities (using the Jaccard coefficient) of the original to the resampled clusters are calculated. The mean of these similarities indicates the stability of a given cluster. The results for the clustering using four clusters is summarized in Table 2.3. The Cluster Stability ranges between 0.97 and 0.68, with higher values found at lower accumulation time scales. Values above 0.85 can be interpreted as “highly stable” (Hennig, 2007); here we have only two clusters below this threshold, indicating that the clustering solution is highly stable and significant, although silhouette widths are low, given the fact that cluster objects tend to overlap to some degree.

Table 2.3 Silhouette Width and Cluster Stability of the k-means approach

Time Scale	1 Month	3 Months	6 Months	12 Months
Silhouette Width [-]	0.30	0.30	0.30	0.25
Cluster Stability [-]				
Northwest	0.95	0.96	0.86	0.89
Southwest	0.95	0.94	0.81	0.68
East	0.97	0.93	0.85	0.86
All Dry	0.97	0.94	0.78	0.94

The obtained clusters are termed after the region within the GAR they are mostly affecting: Northwest, Southwest, East and a cluster termed All Dry which contains DAs covering very large parts of the GAR. Figure 2.8 shows the clusters displayed as a fraction value which indicates how often grid points from a DA are assigned to a given cluster (e.g. Northwest) in relation to the overall size of the cluster (e.g. how often DAs are assigned to cluster Northwest in total).

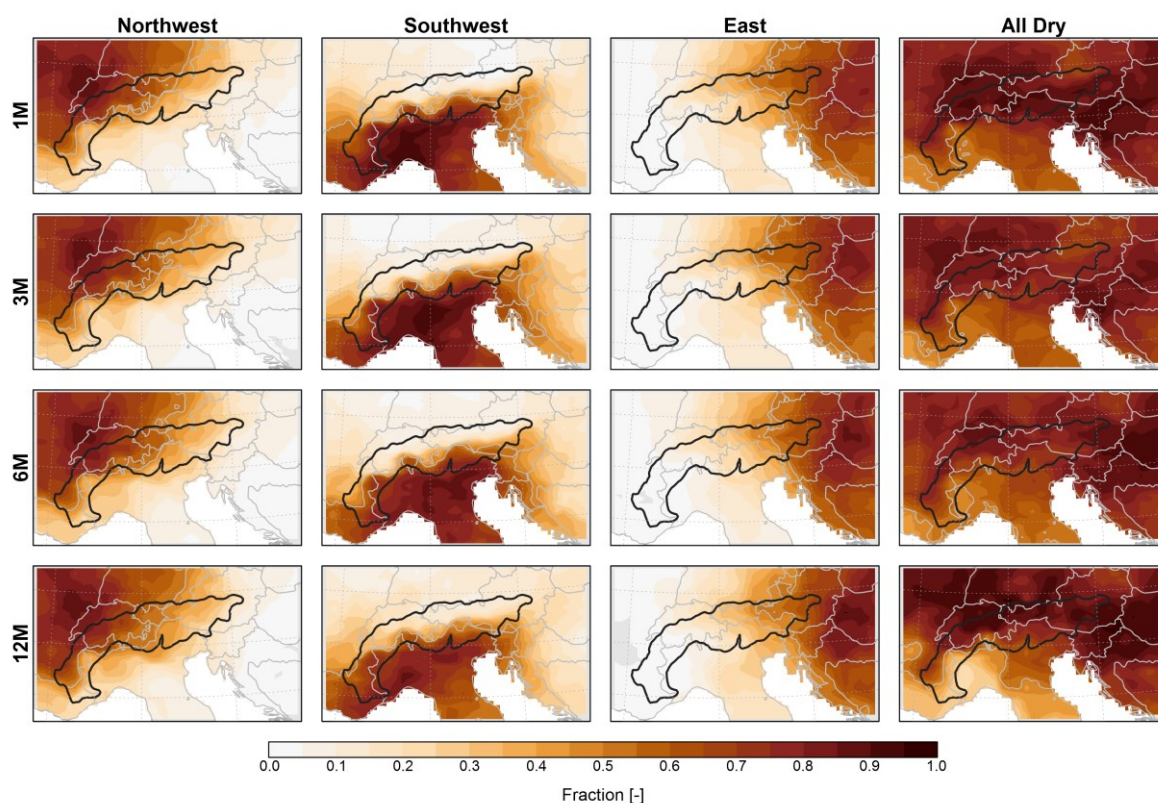


Figure 2.8 Spatial patterns of clusters on different time scales; the Fraction value indicates how often grid points from a DA are assigned to a given cluster (e.g. Northwest) in relation to the overall size of the cluster (e.g. how often DAs are assigned to cluster Northwest in total); higher Fraction values indicate higher accordance of DAs assigned to the given cluster.

The most striking feature of this figure is the similarity of spatial patterns independent of the accumulation time scale. All of these cluster composites show rather similar shapes and nearly identical locations of the center of mass. For example, the Northwest cluster always shows highest fractions near the border triangle of France, Germany and Switzerland, whereas the center of cluster Southwest is located in the Po Plain. The cluster East tends to dominate the whole eastern half of the domain with a center in western Hungary. Moreover, the lower Cluster Stability at 12M time scale (cf. Table 2.3) is also reflected in the lower Fraction gradient from North to South compared to the lower time scales 1M and 3M. The remaining cluster is the All Dry cluster, which indicates DAs where large parts of the domain are below the 20th percentile threshold. The similarity of cluster composites across time scales indicates that DAs are caused by persistent atmospheric circulation patterns leading to precipitation deficit in one of the three sub parts or the whole domain. Our choice of four clusters is based on the mean silhouette widths across all time scales. However, Figure 2.7 also indicates that for a 12M time scale, compared to the other time scales, more clusters (six) would lead to slightly enhanced cluster results. Additional investigations of the patterns with six clusters on a 12M time scale (not shown) revealed consistent results, as two additional clusters emerge from a splitting of cluster Northwest into a western and a eastern part and a splitting of cluster East into a northern and a southern part.

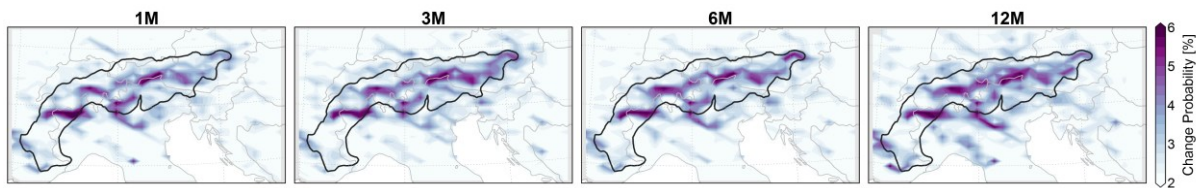


Figure 2.9 Mean of the change probability between a pair of grid points within a DA outside a DA in North-South and West-East directions on different accumulation time scales.

From the above analysis, it becomes clear that the Alps are a major divide between dry and wet conditions under certain circumstances. To underpin these results we performed an additional analysis assessing the probability of change from dry to non-dry conditions in space. Therefore all grid points identified as DAs per time step were flagged as 1 and all the others were flagged as zero. We then calculated the probability for the change in space from dry conditions (grid point value = 1) to near normal or wet conditions (grid point value = 0) between pairs of grid points in the North-South direction as well as in the West-East directions. The number of times a pair of grid points shows a 1/0 (dry/non-dry or vice versa) combination is counted and related to the whole number of time steps. The result is a percentage probability for a change from dry to wet in one direction between pairs of grid points. The mean of these calculations for both directions (North-South, West-East) is displayed in Figure 2.9.

The maps support the results from the k-means clustering, clearly showing a band along the main alpine crest with the highest change probabilities, which are somewhat larger at higher

time scales. The change probabilities in space reach up to 6 % along the main Alpine Ridge and some areas at the southern rim of the Alps where the mountainous terrain gives way to the Po-Plain. The role of the Alps as a boundary of a North-South divide is rather clear, also seen in the k-means clustering results, but more restricted to the western part of the area. However, there is no similar boundary in a West-East direction. Although the clustering revealed an East cluster, the boundary is fuzzier and not as marked as for the North/South clusters. This fuzziness is also confirmed by the spatial change probability assessment, showing no clear areas with enhanced probability in a West/East direction.

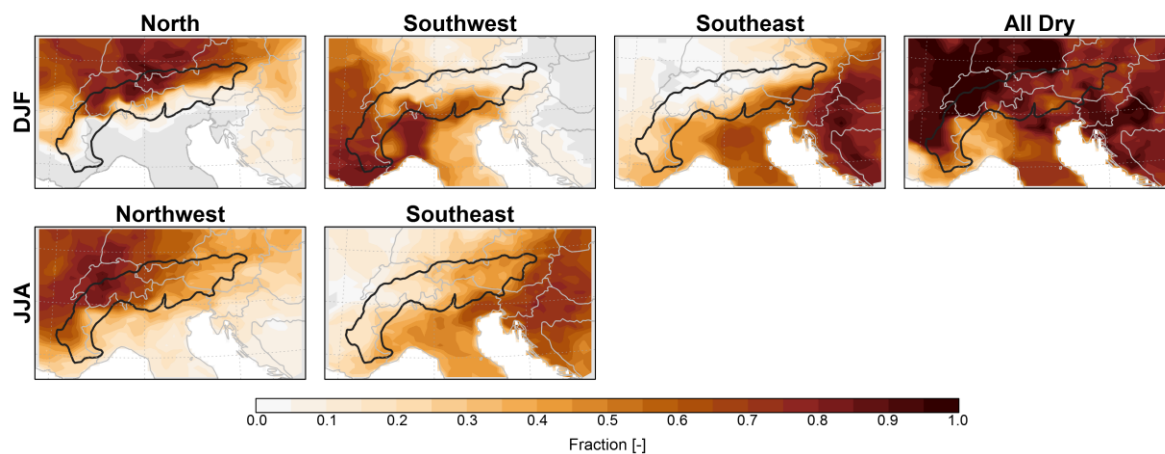


Figure 10. Spatial patterns of clusters on a 3M time scale for winter (DJF) and summer (JJA); the Fraction value indicates the number of cluster assignments of a grid point to a distinct cluster in relation to the overall size of a cluster; higher Fraction values indicate higher accordance of DAs assigned to the given cluster.

In order to assess seasonal differences of spatial drought patterns, the clustering approach was carried out for winter (DJF) and summer (JJA) DAs separately, where we used a subsample of the 3M DAs detected in February (covering December through February) and in August (covering June through August). Following the silhouette width approach the optimal number of clusters is 4 for winter and 2 for summer, cluster stability is again high with a mean value across clusters in winter of 0.72 and in summer of 0.84.

In Figure 2.10 the cluster composites for winter and summer are displayed. Winter shows some similarities with the all year cluster solutions; the first cluster dominates the North of the domain, again with a clear boundary along the Alpine crest, clusters two and three are more in the South and along the western and eastern fringe of the Alps. There is again an All Dry cluster indicating widespread drought across the GAR. In summer the characteristics of the patterns are different. In general, the two clusters show a Northwest - Southeast contrast too, but the region boundaries are rather fuzzy and the Alpine crest is not as clear a separating feature as in the all year analyses or in winter. This might be due to the different mechanisms of precipitation formation in summer which is usually a mixture of stratiform precipitation through cold and warm front passages and convective precipitation which is either triggered by frontal systems or generated locally. Therefore, the precipitation patterns in summer on

monthly or even multi-monthly averages tend to be more heterogeneous than those in other seasons with lower convective activity, resulting in fuzzier cluster boundaries.

2.4.3 Spatial Patterns in time

The occurrence of the identified drought patterns in section 2.4.2 varies over time. Temporal variations are apparent from the overall frequency of DA and also in the partitioning between clusters as can be seen in Figure 2.11. On a 1M time scale DA frequency is peaking in the period from 1860 to 1890 with an overall amount of about 130 DA/30yrs. The strong increase of DAs at the beginning of the time series can be explained by decreasing precipitation sums following the very wet years within the first decades of the 19th century, with a rather low number of DAs. This pattern is also seen on longer accumulation time scales, but in addition other characteristics emerge. Particularly at the 6M and 12M time scales two periods clearly stand out in terms of DA frequency, the time windows from 1850 to 1880 and from 1920 to 1950, showing isolated peaks of 140-160 DA/30yrs.

The fraction of clusters for these 30 year periods is not homogeneous over time. As it was the case for the entire region's frequency, the differences in the frequency of the single clusters are more pronounced at longer time scales. On the 12M time scale, there is no occurrence of DAs in the Northwest region at the beginning of the 19th century. Afterwards a steep increase is visible until the period from 1860 to 1890 showing, around 80 DAs/30 years. The Northwest cluster is the one with highest temporal dynamics along with the East cluster. Both of them trigger the peaks in cluster frequencies in the middle of the 19th and 20th century.

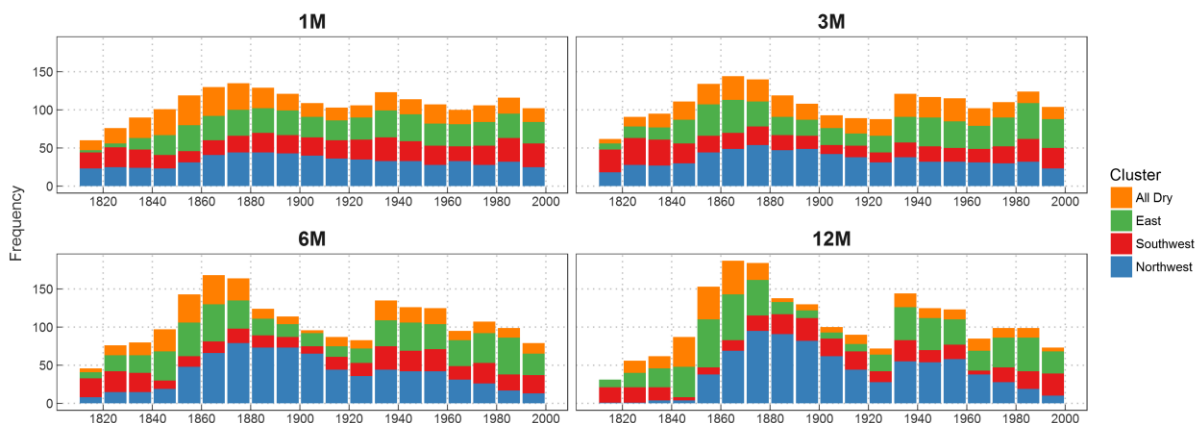


Figure 2.11 Absolute Frequency of clusters within 30-year periods at different accumulation time scales; bars are centered at the given 30-year period, e.g. the first bar at 1815 represents the 1801-1830 period.

In terms of seasonal variability, the results are not as coherent as for the all year analyses. In Figure 2.12 the relative cluster frequencies on a seasonal basis for winter and summer are shown. In winter two pronounced peak periods are visible, one from 1851 to 1870 (16

DAs/30yrs) and another from 1971 to 2000 (15 DAs/30yrs). However, the two main peaks are different with respect to their cluster fraction. The peak in the 19th century is composed of the occurrence of all four clusters with the least contribution from the Southeast cluster, whereas the late 20th century peak is dominated by the Southeast cluster, and the All Dry cluster is not at all present.

Less variation over time of DA frequency is visible in summer. After a steep increase during the beginning of the 19th century the frequencies range between 9 and 12 DA/30yrs. However, the small overall variation is counteracted by periodical changes of the cluster fractions. From 1851 to 1890 as well as from 1911 to 1960 the Southeast cluster is dominating, whereas in the other periods the Northwest cluster occurs more frequently.

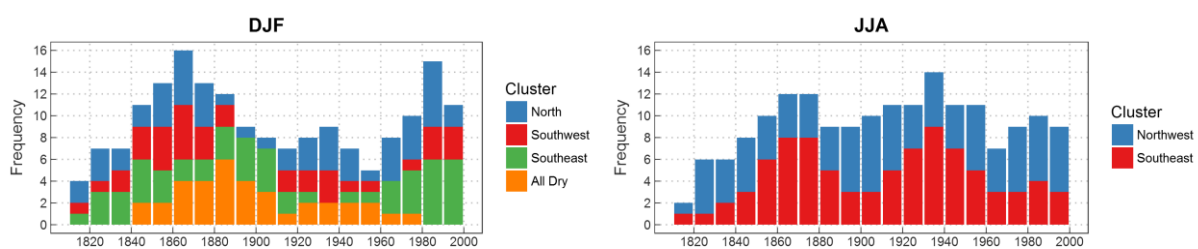


Figure 2.12 Absolute seasonal Frequency of clusters on a 3M time scale enveloping winter (DJF) and summer (JJA); bars are centered at the given 30-year period, e.g. the first bar at 1815 represents the 1801-1830 period.

2.5 Discussion

The analyses of this chapter suggest that the time periods of the 1850s through the 1870s and the 1940s were the driest in the GAR during approx. the last 200 years. This result is in line with the findings of van der Schrier et al. (2007) who assessed the moisture variability based on the scPDSI. Particularly the year 1865 clearly stands out in terms of severity of DAs. The associated DAs developed on different time scales (1M, 3M and 6M, c.f. Table 2) and led to severe drought impacts as some historical evidence shows (c.f. Soja et al., 2013). Interestingly, the year of 1865 is not known for severe drought impacts on agriculture. Although 1865 shows the most severe DA on a 6M time scale from April to September, it were the enveloping months April and September that were the most severest overall (c.f. Table 2). However, the aftermaths of these strong anomalies emerged later in winter. A historical Viennese report on January 1866 stated: „In Leopoldstadt (a part of Vienna) water scarcity is becoming noticeable. Many wells fell dry.“ And: „Increasing water scarcity. The streambed of the Danube Channel is covered with thousands of dead fish.“ (BILKNÖ, 1866; originally in German language, translation by the authors). But not only on a local scale was the severe dry anomaly noticeable. In a study by Pekarova et al. (2006), who investigated long term streamflow trends across

Europe, the authors found the 1860s and 1940s as outstanding dry periods for Western and Central European major river systems. Unfortunately, no North/South distinction among catchments has been carried out in their study. Investigations of more recent drought events in Europe shows increasing dry and continental conditions during the last 20 years in the Carpathian Region (Spinoni et al., 2013) and also increasing drought conditions in the Balkans and Italy, whereas in Central Europe no general trend is noticeable (Spinoni et al., 2015). The results of these papers underpin our results which show increased DA frequency in the Southeast of the GAR, particularly in winter and no (1M and 3M) or even decreasing (6M and 12M) DA frequency in the Northwest cluster during the second half of the 20th century.

However, it is important to assess also the spatial characteristics of meteorological droughts in the GAR, since climate variability and precipitation regimes are rather diverse. Regional aspects have been considered, for example in van der Schrier et al. (2007) who analysed moisture variability in four different regions in the GAR. But the regionalization was based on the PCA of Auer et al (2007) which treated all available climate variables of the HISTALP data base at once (temperature, precipitation, sunshine duration, cloudiness and air pressure). As a consequence, this regionalization might not be useful for deriving homogenous drought regions. With our clustering approach, we were able to show that meteorological droughts tend to develop in three sub-regions and one region covering most of the domain. The results are partly consistent with the PCA of Auer et al. (2007), since our clusters Northwest and Southwest are to some extent comparable to regions Northwest and Southwest of Auer et al. (2007). However, cluster East is in our case not separated into a Northern and a Southern part as is the case in Auer et al. (2007), which is a fundamental difference. Interestingly, accumulating the precipitation on different time scales does not usually affect these patterns in contrast to investigations for e.g. the Iberian Peninsula (Vincente-Serrano, 2006).

These findings along with the change probability assessment in space from dry to non-dry states suggest that the Main Alpine Crest is a distinct boundary between different manifestations of the climate in the GAR. We found that the change probability from North to South for a dry to normal/wet condition is even enhanced if longer accumulation time scales are considered. This indicates that precipitation anomalies are persistent over several months, which may be related to re-occurring weather conditions, enhancing the spatial differences in anomalies. This dipole like feature of precipitation in the GAR was initially detected by Böhm et al. (2003) and analysed in more detail by Brunetti et al. (2006). They found that the North-South (N-S) dipole feature is more prominent than the West-East (W-E) feature, which is in line with the findings of our study. However, they also found an increasing trend in N-S dipole, which they attribute to negative precipitation trends in the southern part and mostly positive trends in northern parts of the GAR. This reflects our finding of dominating South and East clusters on higher accumulation time scales in the second half of the 20th century.

With respect to seasonal aspects, the spatial patterns in winter (DJF) based on a 3M time scale are to some extent similar to the all year analyses indicating, again, a pronounced border along the Alpine Crest between dry and normal/wet conditions based on an optimal cluster solution

of four clusters. For summer, however, this picture is not as clear. The quantitative assessment of an optimal clustering suggested two clusters to be the best following the silhouette width approach, resulting in a Northwest and a Southeast cluster. Furthermore, the cluster borders are much fuzzier and the Alpine Crest is not as strong a boundary as in the all year and winter clusters. The reason for this may lie in the dominance of convective precipitation which is either embedded in frontal systems or generated locally, producing heterogeneous spatial patterns of precipitation.

2.6 Conclusions

Considering the long term perspective of more than 200 years of drought patterns in the GAR we conclude that the time periods of the 1850s through the 1870s and the 1940s were the driest ones, as they showed both highest DA frequency and highest severities. The assessment of the similarity between DAs by the k-means clustering approach revealed three dominant sub-regions for drought occurrence which differ from the previous regionalizations of Auer et al. (2007), for example. We also conclude that the Main Alpine Ridge is a major climatic divide for droughts, which does not only apply daily or monthly accumulation scales (c.f. Böhm et al., 2003), but also to multi-monthly time scales. The frequency of DA occurrence shows no trends, but rather exhibits multidecadal variations which are more pronounced at higher accumulation time scales. Interestingly, these also manifest differently for cluster regions, the North and West were more drought prone in the middle of the 19th century, whereas the East of the GAR shows higher DA frequency within the last decades. These findings indicate the importance of internal climate variability which seems to impact long term spatial precipitation characteristics. This in turn implies that the general warming trend in the GAR (Auer et al., 2007) has either yet no detectable effect on drought patterns in space, or the processes involved are manifold, non-linear, seasonally dependent and therefore not straightforward to analyse.

To better understand the processes driving the results of this chapter it is suggested to examine the circulation characteristics of the atmosphere during the occurrence of DAs. By investigating atmospheric features such as blockings, zonal and meridional wind patterns and jet stream location, the atmospheric conditions leading to dry anomalies within the GAR should be explored and thus better understood.

3. Space-time Patterns of Meteorological Drought Events in the European Greater Alpine Region over the past 210 Years

Abstract

Droughts may have tremendous impacts on humans. However, the space-time characteristics of droughts are not very well understood, as case studies usually focus on individual drought events. Here we investigate the spatiotemporal drought characteristics of a large sample of events over the past 210 years in the Greater Alpine Region of Central Europe. We use monthly precipitation data, and flag, for each grid point, time steps with precipitation below a 20% percentile. We then propose a new method that detects drought events by connecting the flagged elements to space-time drought regions. In contrast to the traditional drought indices that are based on a fixed, prescribed time window, this method is able to identify droughts of different durations in an objective way. The data show multi decadal variations of drought frequency, duration, intensity and severity, but no consistent trends over the 210 year period. The top 5% of events in terms of their severity show a shift in seasonality from winter/spring events in the late 19th century towards autumn events during the last decades of the 20th century. The most severe events center either in the Northwest or the Southeast of the region analyzed. We found no significant correlations of drought frequency, duration, intensity and severity with the temperature increases in the past three decades. Dry springs significantly enhance temperatures during summer droughts, suggesting a soil moisture-temperature feedback.

3.1 Introduction

Droughts are natural hazards with the potential to cause immense damage to agriculture, water supply and energy production, and they can severely affect ecosystems (Vincente-Serrano et al., 2012). The European summer drought of 2003 (García-Herrera et al., 2010) caused economical losses of around €15 Billion (De Bono et al., 2004). The 2015 drought (van Lanen et al., 2016) and a series of winter droughts in the United Kingdom from 2010 to 2012 (Kendon et al., 2013) had similarly negative effects.

However, the understanding of long term drought variability has been hampered by the relatively short time periods analyzed. Studies usually focus on individual events and/or records of 100 years or less. The SREX report (IPCC, 2012) stated that drought trends in Central

Europe are either inconsistent or statistically insignificant and that there is low confidence in the attribution of changes in droughts at the level of individual regions. Gaining knowledge on past drought behavior in Europe over a longer period is therefore of utmost importance (Mishra and Singh, 2010).

Several global to continental scale analyses of past drought trends have been performed. Using various variants of the Palmer Drought Severity Index – PDSI (Palmer, 1965), Dai et al. (2011) found trends towards dryer conditions over Southern Europe, with an increasing trend during recent decades, which they attributed to increasing evapotranspiration associated with increasing air temperatures. These results are not fully consistent with soil moisture trends from simulations by the VIC model (Sheffield and Wood, 2008), which showed no significant changes in soil moisture over the 1950-2000 period (Northern Europe +0.096 % year⁻¹, Southern Europe -0.048 % year⁻¹). Using the self-calibrating Palmer Drought Severity Index – scPDSI (Wells et al., 2004), van der Schrier et al. (2013) found an increase in the percentage area under moderately dry conditions in the Mediterranean and a trend towards wetter conditions in the North of Europe, although these trends were not significant.

More specific analyses focusing on Europe were carried out by Lloyd-Hughes and Saunders (2002) who found an increasing frequency of extreme droughts in continental Eastern Europe during the 20th century period, based on the PDSI, and similar results when considering the SPI on a 12 month accumulation time scale. The most extreme droughts in Europe from 1950-2012 were analyzed by Spinoni et al. (2015) based on a combined indicator that takes precipitation and evapotranspiration into account, considering 3 and 12 month accumulation time scales over predefined European sub-regions. They concluded that the 1950s were the time period with exceptionally long, widespread and intense droughts and that Western and Southern Europe showed highest drought frequency and severity in the past two decades.

A joint assessment of precipitation and temperature quantiles of nine stations across Europe (Beniston, 2009) showed a significant increase in warm-dry conditions from 1901-2009, exceeding the overall warming in Europe. The author argues that this might be related to soil moisture temperature feedbacks (Seneviratne et al., 2006). Van der Schrier et al. (2006) detected negative trends of the scPDSI, indicating dryer summer conditions in Europe until the 1990s with a decline afterwards, which is not fully consistent with the results of Dai et al. (2004). van der Schrier et al. (2006) conducted a regionalization based on Empirical Orthogonal Teleconnections (van den Dool, 2000), and found persistent dry summers in the Balkans from 1983-1994 and from the beginning of the 2000s, only minor changes in Northwestern Europe and very dry conditions in the 1940s in Southern France/Northern Italy. In another study, van der Schrier et al. (2007) analyzed droughts in the Greater Alpine Region (GAR) of Central Europe from 1801-2003, using spatially averaged time series of the scPDSI based on predefined sub-regions (Auer et al., 2007). They found that the 1850s-1870s and 1940s-1950s were exceptionally dry, however, long term trends were not significant.

Drought is a phenomenon that emerges in space and time, and can be characterized by attributes such as duration, spatial extent and intensity (Sheffield and Wood, 2007). Yet many

studies, choose regions a priori and analyze (1-dimensional) time series of regional averages of various drought variables (precipitation, drought indices, streamflow...), even though these regions may not be tailored to drought analyses (e.g. Dai, 2011; Spinoni et al., 2015; van der Schrier et al., 2007; Sheffield and Wood, 2008). On the other hand, there are studies investigating the spatial structure (a 2-dimensional assessment) of drought patterns (e.g. Vicente-Serrano, 2006; Patel et al., 2007) but most of them utilize drought indicators on fixed accumulation time scales (moving averaging time windows). Neither of these two groups of studies considers droughts as a (3-dimensional) space-time phenomenon.

One method that does consider space and time jointly is the Severity-Area-Duration (SAD) method of Andreadis et al. (2005) that evaluates soil moisture and runoff as a function of prescribed areas and prescribed durations (Andreadis et al., 2005; Sheffield et al., 2009; Samaniego et al., 2013; Zhai et al., 2017). Its focus on the areal extent may mask the temporal evolution of droughts which prompted Lloyd-Hughes (2012) to evaluate the space-time structure and similarity of droughts. However, this method is less well suited for analyzing the general characteristics of droughts and their long term evolution in a region.

This chapter proposes a new method for detecting atmospheric drought events that fully accounts of the dynamic space-time behavior of droughts. We use the method to analyze precipitation data in the Greater Alpine Region (GAR) over the past 210 years to detect space-time drought events. Specifically, the aims of the chapter are: (i) to develop a new method of space-time drought event detection, (ii) to analyze the temporal evolution of drought event characteristics (duration, intensity, severity) in the GAR over the past 210 years; (iii) to analyze the spatial patterns of droughts as a function of severity and duration and (iv) to investigate the influence of recent air temperature increases on the three main drought characteristics.

We are interested in meteorological drought events in Central Europe, considering precipitation deficit as the variable of interest. Our region of interest is the European Greater Alpine Region (Auer et al., 2007). Although it is only part of Europe, it covers three main climate divisions in Europe (Mediterranean, temperate oceanic and continental climates) and the three main spatial modes of drought identified by van der Schrier et al., (2006) in the Balkans, Eastern France/Southern Germany and Southern France/Northern Italy, respectively.

3.2 Data

We use gridded data of monthly precipitation totals covering the area from 4°-19° East and 43°-49° North, known as the Greater Alpine Region (GAR, Figure 3.1). This dataset was created by Efthymiadis et al. (2006) in the frame of the HISTALP activities (Auer et al., 2007). HISTALP is a database covering the GAR containing long term (from 1760), high quality, homogenized station time series of various climate variables such as air temperature, air pressure, sunshine duration and precipitation as well as gridded products of air temperature, solid and liquid

precipitation. The dataset of Efthymiadis et al. (2006) has a spatial resolution of 10 arc minutes (~ 16 km) and covers the time period from 1801-2010. The original dataset ended 2003, and was updated for the purposes of this chapter. Auer et al. (2007) homogenized the station data the gridded data set is based on and conducted a comprehensive quality check. Efthymiadis et al. (2006) performed a skill assessment of the gridding process and showed that the skill increases during the first decades of the 19th century and reaches a plateau around 1850. The remaining uncertainties in the gridding process during the first decades of the 19th century have to be kept in mind when interpreting the results of this chapter.

Droughts are considered from different perspectives across disciplines. In this study we focus on meteorological droughts, defined as below average precipitation totals. In a humid climate such as the GAR, precipitation deficit is the main driver for drought development, altered by enhanced evapotranspiration (e.g. Burke and Brown, 2008). We therefore consider precipitation a meaningful variable for analyzing the space-time variability of droughts.

Gridded monthly mean temperature data of the GAR (Chimani et al., 2013) are used as well. They have a spatial resolution of 5 arc minutes (~ 8 km), and cover the period from 1780-2014.



Figure 3.1 Study domain and orography. The dashed box indicates the Greater Alpine Region (GAR) which is the area of interest. For reference the generalized 1000 m.a.s.l. elevation contour is shown as a solid black line.

3.3 Methods

In contrast to the traditional drought indices, such as the SPI, that are based on a fixed, prescribed accumulation time windows and a fixed region, we propose a new method that detects drought events by connecting space-time elements to a coherent space-time drought region. Although widely used, the SPI has some limitations, particularly in terms of a severity assessment of extremes at the tails of the distribution (Naresh Kumar et al., 2009). Stagge et al. (2015) also highlight the uncertainties associated with the distribution fitting at the tails. This uncertainty would translate into the SPI estimates of the most extreme quantiles thus making the severity assessment noisy, particularly if adjacent pixels are compared. For example, the most extreme value at the dry side of the distribution might be -4 at one grid point, but may be -5 at the neighboring one. Both show their most extreme quantile values close to zero, but the SPI itself would be different, simply due to distribution-fitting uncertainty. The use of quantiles instead of the SPI has the advantage of having a fixed lower boundary for the most extreme values, which allows us to identify droughts of different durations in a more robust way. The proposed method consists of four steps:

In a first step, we calculate moving averages of monthly precipitation data over a 3-month time window (centered on the actual month) on every grid point in the domain. This smoothing of the precipitation data is necessary to retrieve meaningful space-time structures of droughts. Alternatively using monthly precipitation totals, for example, would cause interruptions of events along the time axis. A Gamma distribution is fitted to the averaged precipitation, separately for every month of the year and every grid point, in a similar way as in the Standardized Precipitation Index (SPI) (McKee, 1993). The choice of the Gamma distribution is based on Stagge et al. (2015) who found that it provides better fits to precipitation data in Europe than alternative distributions. To separate dry from non-dry areas we chose the 0.2 quantile as a threshold. Although this value is not very extreme (equivalent to a 5 year return period, and an SPI-value of -0.84), it is commonly used to identify dry precipitation anomalies, for example in the US drought monitor (Svoboda et al., 2002). For a more intuitive assessment of drought intensity, these quantiles are scaled in order to get higher values with higher drought intensity using equation 3.1:

$$q_{\text{int}} = (\xi - p) / \xi \quad (3.1)$$

where q_{int} is the quantile drought intensity, p is the probability of non-exceedance and ξ is the threshold of the quantile of 0.2. The intensity measure q_{int} ranges between -4 (probability of non-exceedance of 1) representing wettest conditions and 1 (probability of non-exceedance of 0) representing the most severe drought of a particular location and month. Step two deals with the spatial component of the detection algorithm, where contiguous areas with drought intensity values q_{int} larger than 0 are identified. We use an algorithm starting from the first grid point with positive drought intensity detected in the field, searching for neighboring grid

points with dry conditions ($q_{int} > 0$, grid points joining only diagonally at their corners are not considered). Once a contiguous drought area (DA) is detected, the field is further scanned for dry condition areas until all grid points are checked. The result is a table with all individual drought areas, their time of occurrence (year and month), and location of every grid point and their intensity value q_{int} .

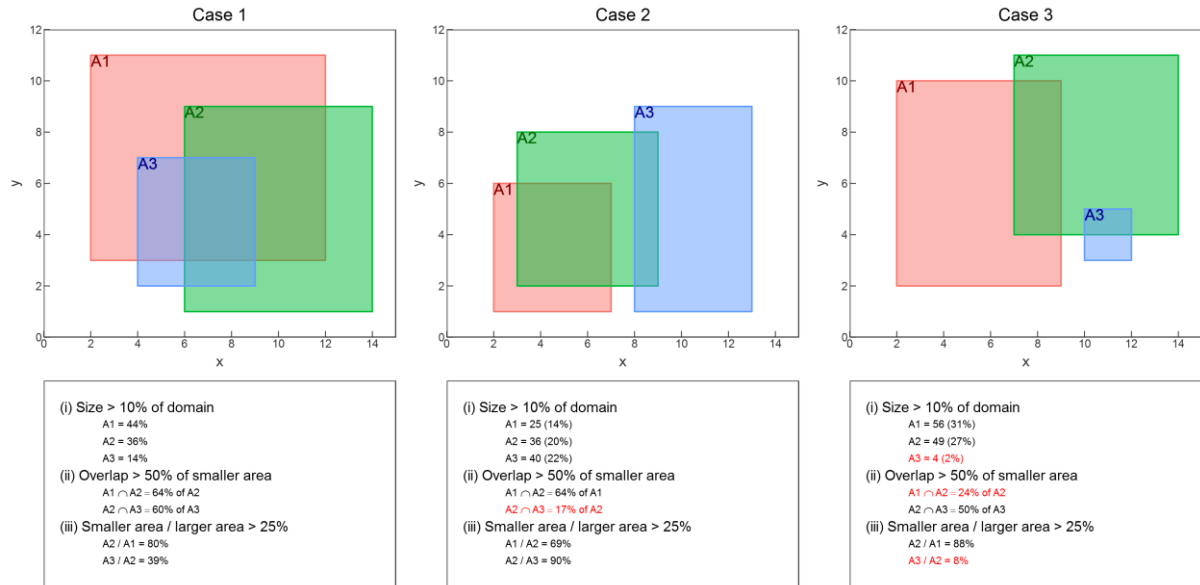


Figure 3.2 Schematics of three cases of drought event detection; upper panels: idealized drought areas as rectangles (A1, A2 and A3) within a region of 15x12 length units; lower panels: check of the three criteria (i), (ii), (iii) that have to be met if the areas are to be joined (see text for details); criterion violations are indicated by red font.

Step three focuses on the temporal component of the detection algorithm. Identified drought areas are compared with the drought areas of the subsequent time step. If these areas do overlap, they are considered to belong to the same drought event (DE), an entity in both space and time. However, we apply three criteria that have to be met for a space-time region to be considered a drought event: (i) single drought areas must be larger than 10% ($\sim 77,000 \text{ km}^2$) of the GAR; we decided for this criterion in order to ensure that only areas with a reasonable size and therefore impact are considered as drought event candidates; (ii) the overlap of the areas must be at least 50% of the smaller area; and (iii) the smaller area must be at least 25% of the larger area. These criteria were identified on the basis of test runs, comparing the detected events with those from the literature. Figure 3.2 shows three hypothetical cases of three subsequent time steps with overlapping drought areas (DAs) (top) and the outcome of the criterion assessment (bottom). In case 1, all criteria are met, yielding an event consisting of all three DAs. In case 2 the overlap criterion is violated for areas A2 and A3, which results in two separate events, the first one including DAs A1 and A2 and the second including A3. In case 3 all three criteria are violated. The size criterion is violated by A3, the other two DAs

(A1 and A2) are big enough, but their overlap is too small. Consequently A1 and A2 are assumed to be separate events and A3 is not considered at all.

Figure 3.3 shows a real event identified from December 1862 to March 1863. The DAs of subsequent months overlap with each other according to the three criteria given above.

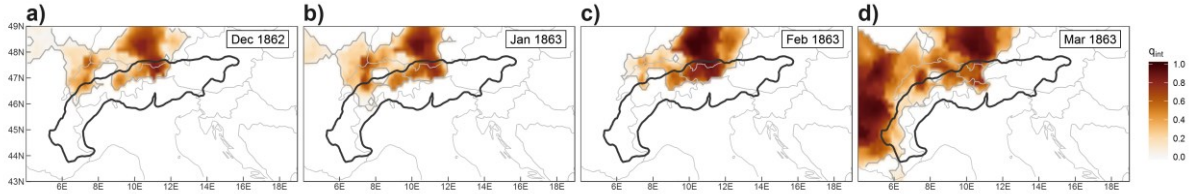


Figure 3.3 Example of a detected meteorological drought event in space and time. The event is identified from January 1863 (a) to April 1863 (d). The grey lines mark zero contour lines of the quantile drought intensities (q_{int}). The colors refer to the quantile drought intensities, darker colors referring to drier areas (larger q_{int}).

The last step consists of evaluating the drought characteristics. One important part is the assessment of the drought event severity. We assume that an event is more severe if (i) the quantile drought intensity q_{int} is large, (ii) the area under drought is large, and (iii) the duration of the drought is large. The first two components are combined into an intensity measure for every time step over the drought duration using equation 3.2:

$$I = \sum_{i=1}^n q_{\text{int}} \quad (3.2)$$

where I is the intensity, n is the number of grid points i within the drought area (DA), q_{int} is the quantile drought intensity. Consequently I increases with both the number of drought grid points and their quantile drought intensity. Figure 3.4a shows the temporal evolution of the intensity from the example in Figure 3.3. From the onset of the drought in December 1862, intensity is around 150 with no large variation until February. As can be seen, the intensity depends on the grid size of the utilized dataset, so it has to be assessed in relation to the whole grid. One could also use the area of the grid which would introduce units of km^2 , but this would overemphasize the spatial component, although the threshold deviation (q_{int} , dimensionless) is equally important. So in the case of December 1862 we have $I=150$ which could either be an area of 150 grid points ($\sim 38,000 \text{ km}^2$) all in most extreme drought conditions ($q_{\text{int}}=1$) or 300 grid point ($\sim 76,000 \text{ km}^2$) with $q_{\text{int}}=0.5$. In our case $q_{\text{int}}=0.3$ and the number of grid points is 492. Comparing this evolution with Figure 3a-c, the areas under drought of the first two time steps are similar in size and in terms of q_{int} . However, in February q_{int} is larger, but the area is smaller, resulting in rather similar intensity values. The peak of the drought intensity was reached in March 1863 with an intensity in excess of 400, which is a consequence of the large area and the large values of q_{int} (Figure 3d). Finally we calculate the overall drought severity using equation 3.3:

$$S = \sum_{i=1}^n I_{i \in DE} \quad (3.3)$$

where S is the severity, which is the sum of all intensities I within the same drought event, and n is the number of time steps comprising the drought event. Consequently, summing up areas in terms of grid points has the same implications as mentioned above considering the intensity assessment, meaning that the interpretation of S is dependent on the grid resolution. For the further analysis the following event characteristics are used: severity, the monthly intensity as well as the mean intensity (severity divided by duration) and duration.

In addition to the temporal evolution of droughts we are interested in their spatial characteristics. As illustrated by the example in Figure 3.3, one time step may contribute disproportionately to the overall drought affected area of an event. It may therefore not be useful to consider the overall drought affected area in a spatial analysis. Instead, we defined Drought Core Regions (DCRs) as shown in Figure 3.4b. Grey areas denote regions not affected by the drought, brown areas the overall extent of the drought (see Figure 3.3) and red areas the Drought Core Region. We define a DCR as those grid points of an identified event with a time-average q_{int} of at least 0.5, which represents a quantile value of 0.1 or an SPI of -1.29. This choice is based on the assumption that the area most affected by the drought has to have a sustained signal of drought during the whole event with a high value of q_{int} . A comparison of Figure 3.3 and Figure 3.4b illustrates that the DCR comprises those areas with the most sustained and intense drought signal during the drought event.

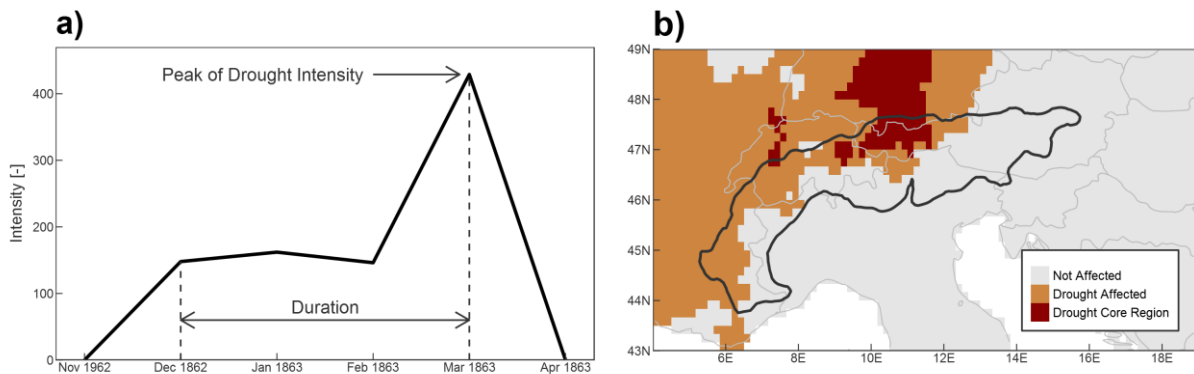


Figure 3.4 Temporal evolution of a drought event (referring to Figure 3.3): the thick black line represents the drought intensity, bounded by the start (Dec 1862) and the end (Mar 1863), indicating a duration of 4 months, and the drought intensity peaking in March 1863 (a); representation of three different spatial entities during the event: areas not affected by drought, areas affected by drought and the drought core region (b).

One further aspect we considered is the temperature anomaly during an event. Similarly to precipitation, we calculated 3-month moving temperature averages. From these, anomalies were calculated for each month individually, with respect to the long term (1801-2008) mean.

Intersecting these temperature anomaly grids with the detected areas of the drought events we obtained the temperature anomalies corresponding to the identified drought areas.

3.4 Results

3.4.1 Temporal Evolution of drought characteristics

A total of 663 drought events were detected in the time period from 1801-2010. 30-year averages of the three main attributes of all drought events (duration, severity and mean intensity) as well as 30-year frequencies are displayed in Figure 3.5a. Frequency shows a continuous increase from the beginning of the data set with a first peak around the 1880s and a second, more pronounced one, around the 1940s with 120 events per 30 years followed by a decrease to around 80 events per 30 years. Duration shows a similar increase until the mid-19th century towards to 3 months, a secondary minimum in the 1930s, and a slight increase during the rest of the 20th century.

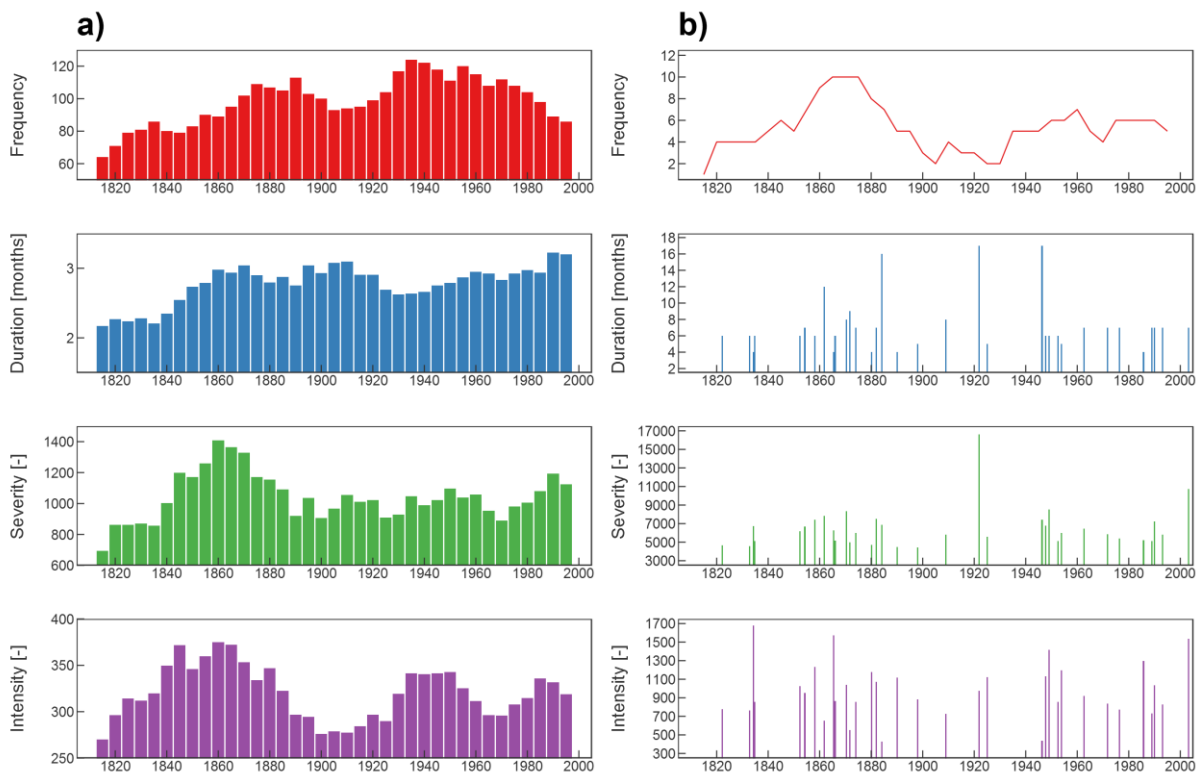


Figure 3.5 Column a): Frequency, duration, severity and mean intensity (overlapping 30-year averages for duration, severity and intensity and overlapping 30-year counts for Frequency with a step of 5 years) of all identified drought events. Column b): The top 5% of the events (34 events) in terms of severity, where Frequency is again the absolute count over 30-year windows with a step of 5 years, and duration, severity and mean intensity are shown for the actual events.

Severity shows the most prominent peak in the middle of the 19th century with mean values up to 1400. During the 20th century, severity varies around 1000. The mean intensity shows even stronger fluctuations with a prominent peak of 370 around the 1860s, very similar to the peak in severity. A sharp decrease follows reaching a minimum of around 270 at the beginning of the 20th century. There is a secondary maximum around the 1940s, and a secondary minimum around the 1970s.

If one analyses only the top 5% of the events in terms of their severity (34 drought events) a somewhat different time evolution of the event characteristics emerges (Figure 3.5b). Frequency shows a clear peak around the middle of the 19th century, indicating 10 of the most severe events occurred in this time period. On the other hand, the lowest frequencies are found from the end of the 19th century until the 1930s. Interestingly, the most severe event on record (Oct. 1920 – Feb. 1922, the 1921-event in Table 1) occurred right in that time period, suggesting that a large frequency does not necessarily imply the occurrence of very large events, and vice versa. In terms of drought duration there are only four of the most extreme drought events that lasted one year or longer, most of them show durations between 6 and 8 months. Only one of these three long-lasting droughts, the 1921-event, has high severities, which is due to the rather low intensities of the other two events.

Table 3.1 Top 10 drought events in the Greater Alpine Region ranked by Severity.

Rank	Period	Duration [months]	Peak	Severity [-]	Mean intensity [-]
1	Sep. 1920 – Jan. 1922	17	Oct. 1921	16610	977
2	Feb. 2003 – Aug. 2003	7	Mar. 2003	10742	1534
3	Oct. 1948 – Mar. 1949	6	Jan. 1949	8513	1418
4	Jan. 1870 – Aug. 1870	8	Apr. 1870	8322	1040
5	Dec. 1860 – Nov. 1861	12	Sep. 1861	7819	652
6	Nov. 1881 – May. 1882	7	Dec. 1881	7517	1074
7	Aug. 1945 – Dec. 1946	17	Apr. 1946	7442	438
8	Oct. 1857 – Mar. 1858	6	Jan. 1858	7403	1234
9	Aug. 1989 – Feb. 1990	7	Nov. 1989	7258	1037
10	May. 1883 – Aug. 1884	16	Feb. 1884	6856	429

The 1921-event is ranked #1 in terms of its severity (Table 3.1). The 2003-event is ranked #2; it gained its severity from the high mean intensity (1534) rather than its duration (7 months). This is also the case for the 1948/49-event on rank #3 with a mean intensity of 1418, duration of 6 months and severity of 8513. Out of the top 10 events, four last 12 months or longer and 6 events have durations between 6 and 8 months. Even though their severities may be similar, their other event characteristics may be very different, as illustrated by the events ranked #7 (1946-event, severity: 7442) and #8 (1858-event, severity: 7403), which have durations of 17 and

6 months, respectively, and mean intensities of 438 and 1234, respectively. These dissimilarities suggest fundamental differences in the emergence of droughts which may be related to different manifestations of weather patterns and their persistence.

These results indicate that duration is a crucial drought feature. Indeed, Figure 3.6 shows a quite different evolution of drought frequency over time when stratifying the events into short (< 4 months), intermediate (4-6 months) and long (> 6 months) events. The frequency of short events is highest, clearly showing two peaks, one minor during the end of the 19th century and a major peak around the 1930s, indicating over 90 events per 30 years, with a subsequent decrease. Events with intermediate durations (4-6 months) show a constant increase in frequency peaking around the 1950s and 1960s, with a subsequent decrease. Long events occur more rarely, and show a distinct peak around 1870, a flat minimum in the middle of the 20th century and a subsequent increase. There is therefore a shift from short/intermediate to long droughts in the past decades.

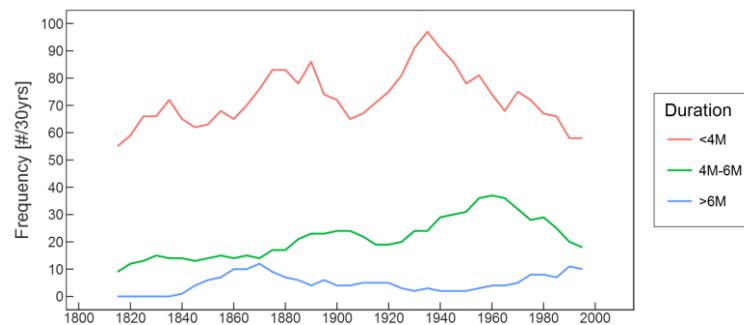


Figure 3.6 30-year running mean (5 year step) drought event Frequency stratified by duration: short (< 4 months), intermediate (4-6 months), and long (> 6 months) events, based on all 663 events.

The seasonal behavior of the top 5% of the droughts is displayed in Figure 3.7. The monthly intensities (Figure 3.7a) highlight the absence of droughts in the first decades of the 19th as well as the 20th century, whereas the rather wet beginning of the 20th century was interrupted by the most severe 1921-event. The intensities averaged over 30-year periods (Figure 3.7b) shows highest values in winter and spring in the middle of the 19th century, peaking from 1851-1880 (late winter/early spring regime). In the following decades until the 1890s, winter months show increasing intensities, while the intensities in spring decrease (winter regime). During the first 40 years of the 20th century, the relatively low extreme drought frequency is apparent, apart from the 1921-event and two cold-season events. From the 1940s a general increase in intensity all year round is visible, but since the 1950s, autumn events (peaking in September) have become more frequent changing into a late summer/early autumn regime from 1961-1990.

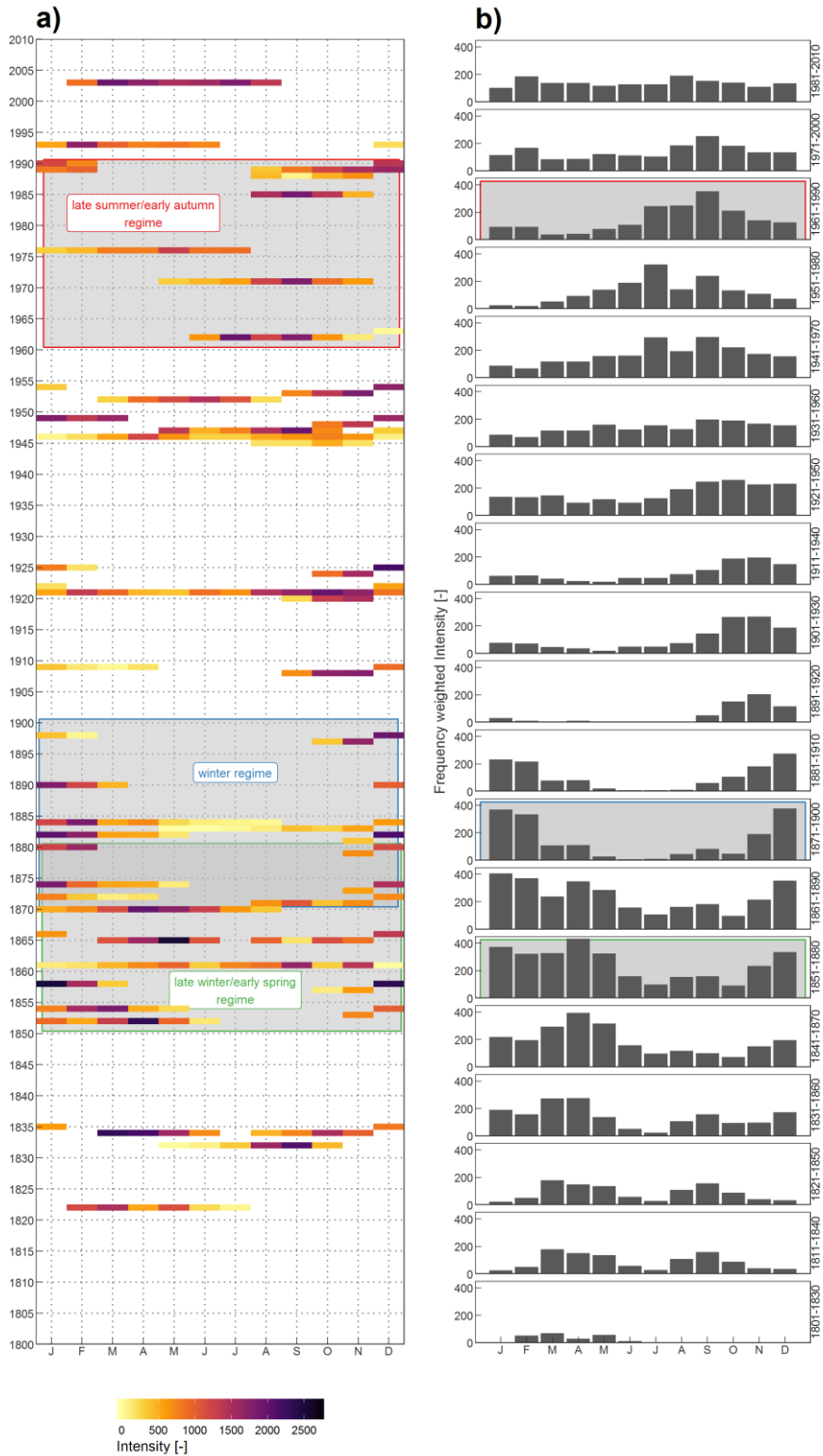


Figure 3.7 Time of occurrence of the top 5% events in terms of their severity (a), colors indicate Intensity of a given time step, horizontal axis is month, vertical axis is year. Frequency-weighted monthly Intensities in 30-year periods calculated for steps of 10 years (right); grey boxes indicate sub-periods with strong seasonal regime differences.

3.4.2 Spatial Patterns

The spatial patterns of the detected drought events are assessed by the ratio of the number of times a grid point is considered as a DCR and the number of all events. For example a ratio of 0.10 at a given grid point indicates that 10% of the whole number of events this grid point is part of a DCR. Figure 3.8a shows these fractions as maps for every grid point using all 663 detected events. There is a tendency for DCR to occur in northern Italy, particularly the Po-Plain (fraction of up to 0.10), and the French Riviera as well as in southern Hungary and parts of the Balkans. If one considers only the top 5% events in terms of severity, a different picture emerges (Figure 3.8b), and DCRs are more clearly separated and emerge predominantly in the Northwest of the domain as well as in the East. In both centers of mass of these two DCR hotspots the fraction goes up to nearly 0.5, which means that during half the events these grid points are part of a DCR. The blue dashed line in Figures 8a and 8b indicates the approximate borders between the different drought regions by visual inspection. These are in line with the Alpine crest being a major climate divide in Europe. Subsequently these sub-regions are referred to according to their location: Northwest, Southwest and East.

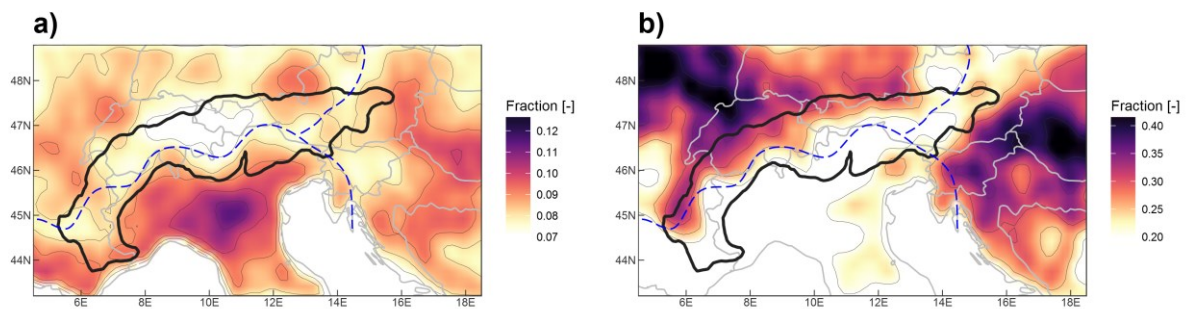


Figure 3.8 Spatial patterns of DCRs for all events (a) and the top 5% events in terms of severity (b). The color shading indicates the fraction value which relates the number of times a grid point is part of a DCR relative to the total number of events considered (for a): all events (663), for b) top 5% (34)). The higher the fraction (darker color) the more often a grid point is part of a DCR). The dashed blue line indicates approximate borders of drought regions.

DCRs rarely occur solely within one of these three sub-regions. More often they cross borders of the region boundaries, although Figure 3.8b clearly shows a Northwest and East concentration of DCRs. Thus as a next step the fraction of DCRs covering the sub-regions is determined and plotted for the top 5% events in Figure 3.9. Most DCRs cannot be attributed to one single region, but there are preferred regions. The fraction of DCRs covering the Southwest region tend to be smaller than those of the other two. This is consistent with Figure 3.8b where the rather low fractions are given in the Southwest considering the most extreme events.

The drought-intense time period around the middle to the late 19th century mostly consists of events with DCRs predominantly covering the Northwest (7 events), with only two events contributing mainly to the Southwest and East. Typically, northwest occurrence is also apparent during the few events in the first decades of the 20th century. However, in the period from 1940-1950, with increased extreme event frequency, DCRs move towards the East, where all events show the highest fraction of DCR coverage.

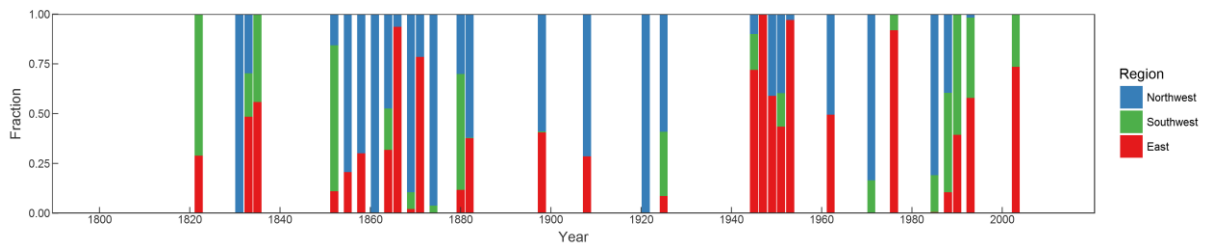


Figure 3.9 Fraction of DCRs covering sub-regions. Vertical bars indicate the time of occurrence of the top 5% events by severity. The color of the bars indicates the fractional overlap over sub-regions. The horizontal positions of the bars have been slightly adjusted for them to plot without overlap.

In the light of this spatial analysis, the previously described seasonal shift of extremes from winter/spring (end of 19th century) towards autumn (end of 20th century) has to be considered as a shift in space as well as a shift in seasonality, implying a fundamental feature of drought occurrence in the GAR. This could be due to changes in the mid latitude circulation since the end of the Little Ice Age as indicated by Schwander et al. (2017). They found increased frequencies of high pressure patterns over Central Europe from 1960 onwards, which could explain the dominance of Eastern droughts in that period, and increased frequencies of Northern Cyclonic patterns and Westerly flow over Southern Europe patterns during the period from 1850-1880, which may be related to the droughts predominantly affecting the Northwest.

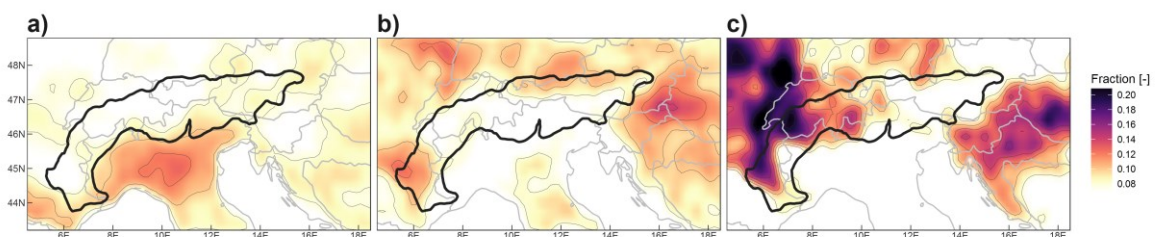


Figure 3.10 Spatial patterns of DCRs for short events (a, duration < 4 months), intermediate events (b, duration 4-6 months) and long events (c, duration > 6 months). The color shading indicates the fraction value which relates the number of times a grid point is part of a DCR relative to the whole number of events considered (for a): short events (481), for b) intermediate events (148), for c) long events (34)). The higher the fraction (darker color) the more often a grid point is part of a DCR).

Figure 3.10 shows the DCR fractions for events considering different durations, independent of the severity. Short term events (Figure 3.10a) are most abundant which explains the similarity with Figure 3.8a. As can be seen in Figure 3.10b, the spatial patterns of intermediate events (148 events) show their DCRs mostly in the North and East of the domain, and the long events (Figure 10c, 34 events) show the preferred location in the Northwest and the East.

3.4.3 The drought - temperature nexus

The large sample of droughts over the last two centuries offers the opportunity to assess the long-term relationship between air temperatures and drought characteristics. In the GAR, air temperatures in the period 1900-2000 have increased, on average, by 1.2°C based on linear trend analysis (Auer et al., 2007). We calculated annual average air temperatures over the whole domain of the GAR and identified the coolest and warmest 30-year period, which turned out to be 1876-1905 and 1981-2010, respectively. The corresponding temperatures are 7.86 °C and 9.27°C, respectively (Table 3). The difference thus is 1.41°C, which is slightly above the 20th century temperature change of Auer et al. (2007) as mentioned above. The average drought characteristics (duration, mean intensity, severity and 30-year frequency) of the coolest and the warmest periods are given in Table 3.2. Duration shows an increase from the cool to the warm period from 2.75 to 3.20 months which is consistent with Figure 3.6. Mean intensity increased from 297 to 319, and Severity from 921 to 1125, although these changes are not significant. However, frequency decreased from 113 to 86 detected events. These results suggest that the recent warming climate has, so far, not significantly affected the drought characteristics in the GAR.

Table 3.2 Mean Temperature, Duration, Mean intensity, Severity and Frequency of drought events in the coolest and warmest 30-year periods in the GAR.

Note. Significance of the difference between the two periods expressed by the p-value of the Wilcoxon test statistic. ** denotes for significance at the 5% level ($p < 0.05$).

	Coolest Period		Warmest Period	
	1876-1905		1981-2010	p-value
Temperature [°C]	7.86		9.27	0.00**
Duration [months]	2.75		3.20	0.10
Mean intensity [-]	297		319	0.66
Severity [-]	921		1125	0.24

The seasonal aspects of the drought - temperature nexus are displayed in Figure 3.11. Each event emerging in the three winter months (DJF) and the three summer months (JJA) is shown as a circle (having events with durations > 3 months only these three seasonal months are extracted); drought intensity during these three months is indicated by the size of the circle, and vertical position and color indicate the associated temperature anomaly of this event.

In winter (Figure 3.11a) droughts with both positive and negative temperature anomalies occur. This behavior is related to air temperatures in winter mainly being forced by the advected air masses in the GAR, either cold or warm, dependent on the large scale circulation characteristics (Auer et al., 2007). This is not only true of the overall temperature characteristics, but also of those during droughts. Really cold winter droughts with temperature anomalies below $-3\text{ }^{\circ}\text{C}$ occurred mostly in the late 19th century and the first half of the 20th century. From the 1950s onwards there is an absence of such events. Running correlation of mean intensity and temperature anomaly (30 year window, Figure 3.11c) reveal no relationship until the 1970s, however, afterwards a steep increase in correlation is apparent, indicating higher mean intensities associated with higher temperature anomalies in the recent past.

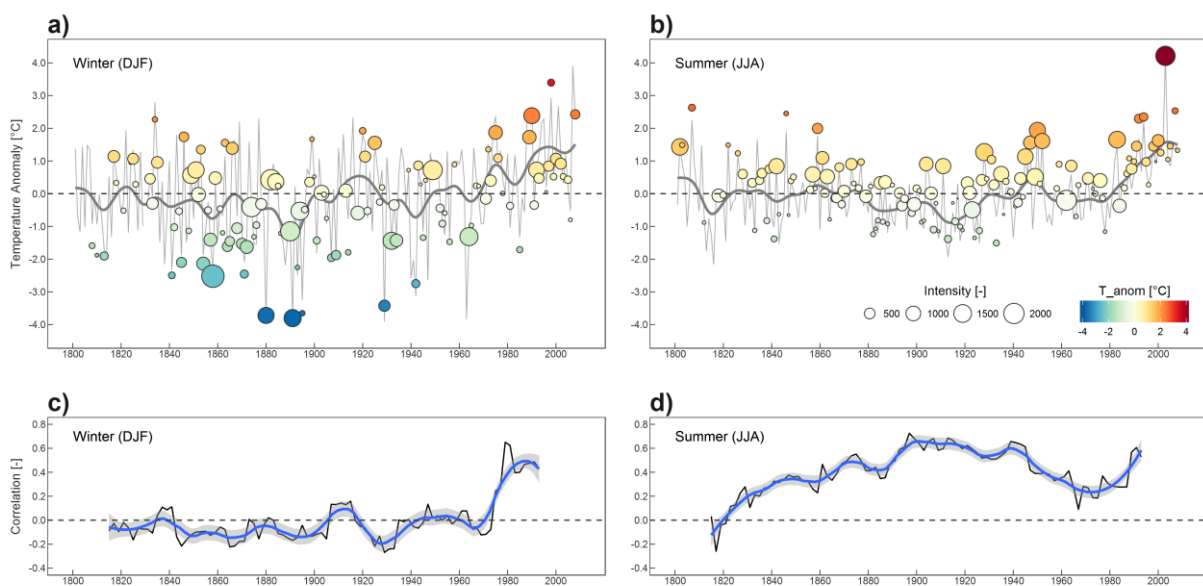


Figure 3.11 Upper panel: Mean intensities and corresponding temperature anomalies of drought events of a minimum duration of 3 months covering winter (DJF) and summer (JJA) (a, b). Size of circles indicates intensity; location along the vertical axis and the color shading indicate temperature anomaly. In the background the seasonal mean temperature anomalies of the whole GAR are plotted in grey (thin line: seasonal means, thick line: 20-year Gaussian filtered seasonal means). Lower panel: Running correlation (Spearman rank correlation) of Mean intensity and temperature anomaly over 30-year periods with a step of 2 years (c, d).

Summer temperatures (Figure 3.11b) show a smaller year to year variability, and droughts are more likely associated with above average temperatures. This would be expected as the absence of rainfall is usually accompanied by lack of clouds, high sunshine duration and therefore higher temperatures. However, there is no clear indication that high positive temperatures are also associated with high intensities, although the 2003-event stands out as a single event where this is the case (Wetter et al., 2014). Interestingly, the 2003-event was not the most intense summer drought, it was the summer of 1962 which was even drier than 2003,

although its temperature anomaly was slightly below average ($-0.4\text{ }^{\circ}\text{C}$). This suggests that dry summers are not necessarily hot. Additional analyses (not shown) indicate, that the circulation patterns during these two summers were rather different; in 2003 a blocked weather situation governed the drought with increased subtropical warm air advection, while in 1962 westerly (cool) airflow from the Atlantic into the GAR dominated. However, the running correlation analysis (Figure 11d) shows an increase from zero at the beginning of the 19th century up to 0.6 around the late 19th/early 20th century, and a decrease afterwards until the 1970s, followed again by an increase in correlation. These results suggest that the positive relationship between mean intensity and temperature anomaly is stronger during periods with cooler climate conditions, as summers tended to be coolest at the beginning of the 20th century.

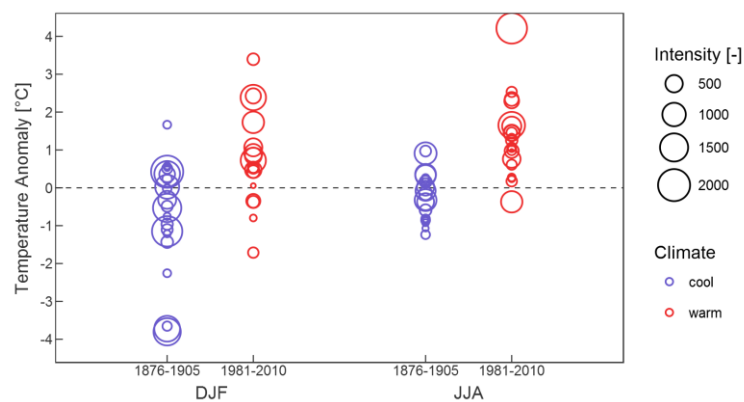


Figure 3.12 Intensity and respective temperature anomaly of drought events of a minimum duration of 3 months covering winter (DJF) and summer (JJA), during 30-year periods of coolest/warmest climate conditions (cool: 1876-1905, warm: 1981-2010).

The drought – temperature relationship is further analyzed in Figure 3.12 which shows the drought intensity and temperature anomaly for the two periods from Table 3, stratified by season similar to Figure 3.10. During cool climate conditions (1876-1905), some major winter events had very low temperatures while the summer events show smaller temperature anomalies compared to the long term mean. As mentioned earlier, events with high mean intensity and considerable negative temperature anomalies did not occur in recent decades. In the cool decades at the end of the 19th century high mean intensities are apparent for very cold, as well as for slightly above temperature anomalies, indicating a large spread of temperature characteristics during droughts, which is consistent with the running correlation analysis of Figure 3.11c. All these findings point towards major changes in the weather patterns leading to droughts, particularly the location of precipitation-inhibiting high pressure systems and the associated air mass advection into the GAR. During warm climate conditions (1981-2010), the summer events, again, show smaller temperature anomalies if one does not count the 2003 event which has been extraordinary. It is interesting that the cold period featured two cold outliers while the warm period featured a warm outlier.

The distribution properties of the mean intensity on a seasonal basis are evaluated by Empirical Cumulative Distribution Functions (ECDFs) of the mean intensity stratified by temperature anomalies (Figure 3.13). In winter (DJF) higher drought intensities are associated with near normal or below average temperatures. The less pronounced tail of the intensity distribution for the warm events indicates less potential for warm winter droughts with high intensities. Cold winter droughts are likely to be caused by continental high pressure systems which tend to be very persistent, which may not be the case for the warm winter droughts. In spring (MAM), no clear shift in the intensity distribution of different temperature stratifications is apparent. However, in summer (JJA) rather different ECDFs are apparent, indicating that higher drought intensities are associated with higher temperature anomalies and, conversely, cool summer droughts are usually not very intense. The same signal is apparent in autumn (SON), but is less distinctive.

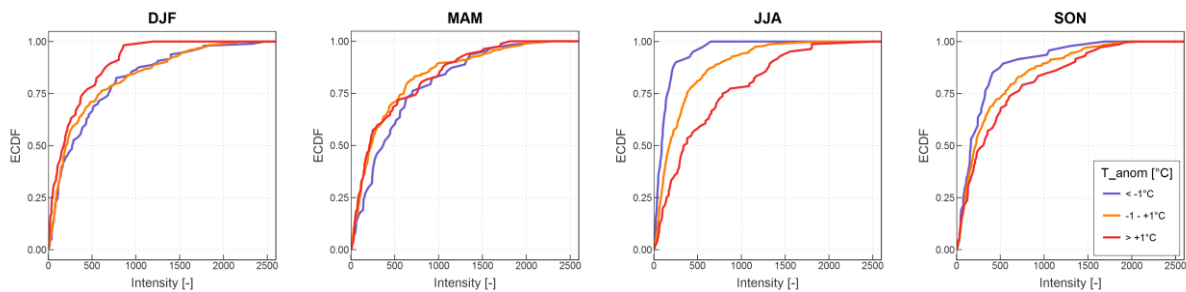


Figure 3.13 Empirical Cumulative Distribution Functions of drought Intensities (over three months) stratified by seasons: winter: DJF, spring: MAM, summer: JJA and autumn: SON, and stratified by the corresponding temperature anomaly; below average: blue, near average: yellow, above average: red.

While intense summer droughts (such as the 2003-event, see Figure 3.10b) tend to be warmer than average, this was not the case for the 1962-event. The two events also differed in terms of their temporal evolution. The 2003-event started in February (see Figure 7a), whereas the 1962-event started in June with normal precipitation conditions during spring. This suggests that the summer temperature anomaly during droughts may be related to preceding spring precipitation. We therefore analyzed summer droughts and separated those with dry springs from those where the drought did not start before summer. The Probability Density Functions of the monthly temperature anomalies from May to August for both samples are plotted in Figure 3.14. A distinct shift towards higher temperature anomalies during summer with dry spring preconditions (mean temperature anomaly: $+0.73^{\circ}\text{C}$) is apparent compared to those events where spring was wet (mean temperature anomaly: $+0.30^{\circ}\text{C}$). This difference in the mean is significant according to the Wilcoxon test on the 5% level (p-value: 0.042). Also noticeable is a broader right tail of the distribution (positive temperature anomalies).

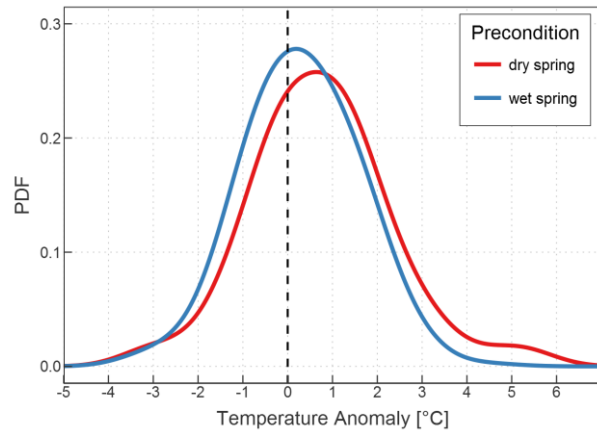


Figure 3.14 Probability Density Function (PDF) of monthly temperature anomalies during May-August, stratified by drought conditions of the preceding spring. Red: drought event covering spring and summer (dry spring precondition); blue: drought event covering only summer (wet spring precondition).

3.5 Discussion

In this chapter we present a new method for identifying meteorological drought events based on connected space-time regions. We analyze a 210-year precipitation data set to explore drought event durations, intensities, severities and frequencies. As would be expected, well-known severe droughts rank highly in the results, such as the 2003-event (Fink et al., 2004) (Wetter et al., 2014), the 1921-event (Brooks and Glasspoole, 1922) and the 1946-event (Brazdil et al., 2016).

Our results on the temporal evolution of droughts during the last two centuries is in close agreement with previous studies that have tagged the 1940s and the period from 1850 to 1880 (the 1860s period) as drought prone time periods (e.g. van der Schrier et al., 2007; Lloyd-Hughes, 2012; Lloyd-Hughes and Saunders, 2002). Here we were able to clearly distinguish these two periods from their spatio-temporal features. The 1860s period shows the highest values in both severity and mean intensity as well as in frequency of the major (top 5%) droughts. At the same time, the analysis of frequency stratified by duration revealed that this period shows a peak in the occurrence of long (> 6 months) droughts. In contrast, the 1940s show only slightly lower mean intensities, but severity is not peaking. This is related to the low frequency of long droughts, while short (< 4 months) and intermediate (4-6 months) events show rather high frequencies.

The seasonal patterns exhibited a major shift of the extreme droughts from a winter/spring dominated regime in the 1860s towards an autumn regime in the 1960s, whereas the period around the 1940s shows no strong seasonality. A possible mechanism of the 1940s droughts could be the expansion of the tropical belt and the Hadley cell during that time period (Brönnimann et al., 2015) which may have caused more subtropical high pressure systems to affect Central Europe. This would also be consistent with the joint drought/temperature

assessment showing a clear peak in the intensity and temperature anomaly of summer droughts in the 1940s (see Figure 3.10). However, this is not consistent with the results of Schwander et al. (2017) who showed that high pressure weather patterns over Europe did not peak during this period. Their results indicate weather patterns with easterly or northerly flow to dominate.

Whereas in the 1940s it was predominantly the East of the domain which was most affected by droughts, in the 1860s it was the Northwest. While the reasons for these differences are not fully clear due to data limitations, the features of the 1860s with their highest mean intensities, long durations and winter/spring dominance point towards high frequency and/or high persistency of high pressure weather patterns over Central Europe which might be introduced by a wavier jet stream bearing the potential for excessive blocking situations. We also found a transition in seasonality from the 1860s (high winter/spring intensities) towards the end of the 20th century (higher autumn intensities). Interestingly, this seasonal shift is accompanied by a spatial change from the Northwest to the Southeast. The location of drought centers is primarily driven by the location of the drought inducing weather patterns (e.g. high pressure systems). Schwander et al. (2017) found higher frequencies of high pressure systems over Central Europe from the 1960s to the 1990s, which would confirm the higher drought intensities in that period. In contrast, no such peak is apparent during the middle of the 19th century, the period with the highest drought intensities. Above average high pressure situations are therefore not likely the main cause. It is possible that the location of the high pressure pattern does not have to be over Central Europe, given that the Northwest is the area most affected by droughts during this period. Extensive highs over the British Isles could also affect the Northwestern GAR and would be accompanied with northerly airflow. Increased frequencies of weather patterns with Northerly airflow have been found by Schwander et al. (2017) during the 1860s and could explain the frequent high intensity droughts in the Northwestern GAR. There is, however, room for better understanding the atmospheric drivers in this period.

The evaluation of the temperature increase in the GAR in relation to drought characteristics yielded no significant relationships, although previous studies (van der Schrier et al., 2006; van der Schrier et al., 2007; Dai, 2011) did report increasing drought conditions over Central Europe during recent decades. This is mainly due to fact that drought indices, such as the PDSI where a temperature based parameterization of evapotranspiration is used, imply a relationship between droughts and temperature. Trends of changing weather patterns in the mid-latitudes over the last decades (Weusthoff, 2011) point towards an increased frequency of high pressure weather patterns over Central Europe, but this does not seem to manifest itself in more severe or frequent droughts. We did find a significant shift in the temperature anomalies during summer droughts dependent on the spring preconditions (wet/dry). Mueller and Seneviratne (2012) identified a positive relationship between preceding negative SPI values and the occurrence for hot days in Europe and other parts of the world. These and our findings suggest that soil moisture - temperature coupling is of major importance for

drought development in the warm season, as it could increase drought stress through enforced evapotranspiration. Although there is no clear signal of increased summer drought intensity or frequency apparent from the precipitation analysis in this chapter, further increasing trends of high pressure pattern frequency over Europe in winter and spring (Weusthoff, 2011) may have implications on summer droughts in a warming climate.

The new method of drought detection proposed in this chapter allowed for an objective analysis of drought characteristics, including drought duration. However, the method does have its limitations. It is based on a connectivity approach where connected space-time elements of below threshold precipitation are connected to a coherent region, i.e. the space-time drought event. While the connectivity approach is attractive as it is able to identify events, rather than minima of an index, it is not fully independent of the space and time resolution used in the analysis (see Western et al. (1998, 2001) for a discussion of grid resolution in the context of soil moisture connectivity). The smaller the space-time discretization, the smaller tend to be the regions identified, as a coarser resolution averages out any small scale features that may interrupt a coherent space-time region. We used a 3-month temporal averaging and a spatial resolution of 10 arc minutes (~16 km). It would be interesting to analyze the effect of the resolution on the results. Preliminary analyses suggest that there is an effect on the absolute value of the drought characteristics, but the space time patterns of the results (long-term variability, spatial patterns of drought core regions) change very little. Future work could be directed towards more quantitatively analyzing the atmospheric drivers of the space-time drought patterns, both in Europe and elsewhere. Finally, the method could be readily applied to drought realms other than meteorological droughts (agricultural, hydrological droughts) by using soil moisture and streamflow in addition to existing pooling methods for obtaining temporally coherent hydrological drought events (e.g. Laaha et al. (2017)).

3.6 Conclusion

In this chapter we proposed a new method for detecting atmospheric drought events and their space-time structure. We used the method to analyze the long term evolution of drought frequency, duration, intensity and severity over the past 210 years in the Greater Alpine Region (GAR) in Central Europe. Our results show variations of these characteristics on multi-decadal time scales, but no trends over the 210 year period are apparent. Two periods (the 1860s and 1940s) stand out as drought periods, although the characteristics of individual droughts in these decades are substantially different, indicating different driving mechanisms. The most extreme droughts show their centers either in the Northwest or the Southeast of the GAR, with a larger number of Northwest events in the 19th century and a shift towards Southeast events in the second half of the 20th century. Although temperatures increased significantly during the period, we did not find the increase to be significantly correlated with drought duration, intensity or severity. However, we found that dry springs significantly increase temperatures during subsequent summer droughts, which implies soil moisture-

temperature coupling in the warm season. Further research should be directed towards better understanding the drivers of long-term drought fluctuations.

4. Disentangling drivers of meteorological droughts in the European Greater Alpine Region during the last two centuries

Abstract

This study investigates the atmospheric drivers of precipitation deficit of the most severe meteorological droughts in the Greater Alpine Region during the last 210 years. We use a daily atmospheric circulation type reconstruction tailored to the Alpine region with precipitation as the focus variable. Precipitation deficit tends to be higher during periods with more frequent anticyclonic (dry) and less frequent cyclonic (wet) circulation types, as would be expected. However, circulation characteristics are not the main drivers of summer precipitation deficit, when preceding soil moisture conditions are more important. Dry soils tend to limit precipitation, which is particularly the case for low air pressure gradient circulation types that enhance the propensity for local convection. This mechanism is of specific relevance in explaining the major drought decades of the 1860s and 1940s. Both episodes show large negative anomalies in spring precipitation followed by increasing frequencies of circulation types sensitive to soil moisture precipitation feedbacks, enhancing the drought signal in summer. The dry springs of the 1860s were likely caused by circulation characteristics that were quite different from those of recent decades as a consequence of the large spatial extent of Arctic sea ice at the end of the Little Ice Age. On the other hand, the dry springs of the 1940s developed under a persistent positive East Atlantic/Western Russia pattern, triggered by positive sea surface temperatures in the western subtropical Atlantic.

4.1 Introduction

A prolonged lack of precipitation may have serious impacts on various aspects of human society, including water supply, agriculture, hydro power production and river navigation, as the drought signal tends to propagate through the hydrological cycle from the surface to the soils, rivers, lakes and the groundwater (Van Loon et al., 2012; Sheffield & Wood, 2011; Tallaksen, 2006).

While it is essential to better understand droughts in a changing climate, whether and why droughts in Europe have changed in the past centuries is still under debate. Some studies have identified an increase in drought frequency and severity (e.g. Dai, 2013) while others suggest no significant changes have occurred (Sheffield et al., 2012). IPCC (2012, SREX) concludes that due to inconsistent signals of the various drought indicators no clear trends for Central Europe

can be inferred. Yet, there is evidence for an intensification of the water cycle with global warming (Huntington et al., 2018; Held & Soden, 2006) which might involve an intensification of drought conditions, especially in the summer when soil moisture-precipitation feedbacks are strongest (Seneviratne et al., 2010).

Several studies investigated the atmospheric drivers of individual extreme drought events in Europe. For example Ionita et al. (2017) analyzed the severe summer drought of 2015 (Laaha et al., 2017; Van Lanen et al., 2016) in a climatological context. They found that the drought event was triggered and enhanced by four heat waves caused by persistent blocking events and a deflection of the Atlantic storm tracks towards the North. Similarly, the extreme precipitation deficits of the Iberian drought in 2004/2005 (García-Herrera et al., 2007) and the devastating summer drought of 2003 (Black et al., 2004) were caused by anticyclonic activity in combination with a positive soil moisture-precipitation feedback.

There have also been studies that jointly analyzed drought mechanisms for a number of events. For example Kingston et al. (2006) and Lavers et al. (2013) investigated precipitation and streamflow anomalies across Northern Europe and found that the North Atlantic Oscillation (NAO) is a principal driver, which implies dry conditions during its negative phase, particularly in the winter. On the other hand, Linderholm et al. (2009) found that the NAO also plays in the drought development of Northern Europe during summer. These findings are in line with other studies that highlight the NAO phases as an important cause of dryness/wetness variability over Europe (Hannaford et al., 2011; López-Moreno & Vicente-Serrano, 2008; Vicente-Serrano et al., 2016). According to these studies, Northern Europe tends to exhibit strong positive correlations between NAO and droughts, Southern Europe strong negative correlations, and there is a zone with weaker correlations in between. There is therefore little evidence of the NAO state being a meaningful indicator of wet or dry conditions in Central Europe, including the European Alps. Other large scale circulation indices explaining European climate variability include the Arctic Oscillation (Thompson & Wallace, 1998), the Scandinavian Pattern (Bueh & Nakamura, 2007), the El Niño Southern Oscillation (Brönnimann, 2007) and the East Atlantic/Western Russia Pattern (EAWR, introduced by Barnston & Livezey (1987) as the Eurasian Pattern type 2). The latter is related to drought inducing atmospheric circulation, as shown by Ionita (2014) who concluded that mid-winter to late spring precipitation is strongly impacted by the EAWR teleconnection. Similarly, Kingston et al. (2015) found that, while the NAO is an important driver of Northern European droughts, the EAWR is more important for other regions.

For the Alpine region, Efthymiadis et al. (2007) found precipitation variability in the Southeastern Greater Alpine Region (GAR) to be forced by the NAO, while the EAWR was more important for the Northwestern GAR. The NAO influence seems to vary considerably over time (Brunetti et al., 2006). Scherrer et al. (2016) showed the NAO to be of little influence for precipitation in Switzerland, the Eastern Atlantic Blocking pattern to be important for the northern slopes of the Alps, and the Eastern Atlantic pattern to be relevant for the southern

slopes. The specific atmospheric processes forcing the development of drought conditions in the Greater Alpine Region, however, are not fully understood.

The purpose of this chapter therefore is to explore the atmospheric mechanisms controlling droughts in the GAR in the past 200 years. The specific aims of this chapter are: (i) quantifying the relationship between precipitation deficit during drought events and atmospheric circulation anomalies on a daily basis; (ii) evaluating seasonal differences between atmospheric forcing and soil moisture feedback, (iii) understanding the atmospheric drivers of the exceptionally dry decades of the 1860s and 1940s; and (iv) assessing these in the context of possible future climate change. We address these aims by making use of recently published data on the space-time extent of meteorological drought events in the GAR back to 1801 (Haslinger & Blöschl, 2017) and a reconstruction of daily weather types back to 1763 tailored to precipitation in the Alpine region (Schwander et al., 2017), thus going significantly beyond existing research.

4.2 Data and Methods

We use a subset of the Haslinger & Blöschl, (2017, HB17 hereafter) dataset on meteorological drought events in the GAR. The data set consists of a total of 663 events; we only use the top 5% (34 events) in terms of their drought severity. Table 4.1 gives the main event characteristics, including dimensionless mean drought intensity and severity as derived by HB17. These event characteristics were calculated by assessing the extent of spatially contiguous precipitation anomalies (decedence of the 0.2 quantile) tracked along time to detect space-time drought regions. The corresponding spatial average over the GAR of precipitation, average precipitation deficit and accumulated precipitation deficit are also shown. The average precipitation deficit is the difference between average precipitation during the event and the climatological mean (1801-2010) precipitation. The accumulated precipitation deficit is the average precipitation deficit multiplied by the duration. The event durations used here are two months longer than those given in HB17 because they were based on a 3-month moving average leading to somewhat too short events. In order to cover the entire drought period at higher resolution, we added one month at the beginning and the end of the event. The seasonal assignment is based on the stratified mean drought intensity of the cold season (NDJFMA) and the warm season (MJJASO), with the higher drought intensities giving the season in which the drought was most pronounced. The peak is defined as the month with the highest drought intensity.

The relationship between droughts in the GAR and continental scale atmospheric weather patterns is investigated by use of the circulation type classification CAP7 (Schwander et al., 2017). Circulation types (CT) are a limited number of representative, stationary patterns of the continuum of the atmospheric circulation and are frequently used to investigate their relationship with surface climate variables (Philipp et al., 2010). The choice of a certain CT classification depends on the parameter of interest and the number of classes defined therein

as well as on the method and the spatial domain used for the classification (Beck & Philipp, 2010; Philipp et al., 2016).

For this study CAP7 (Schwander et al., 2017) was chosen, which was developed for the Central European region (Schwander et al., 2017, Figure 1 therein) and therefore matches with the region of interest of this study very well. The classification contains seven different circulation types that have been determined by principal component analysis in the reference period from 1960-2000, followed by temporal clustering. A reconstruction of CAP7 in daily resolution is available back to the year 1763, and a subset for the 1801–2010 period is used in the current study.

Figure 4.1 shows the main characteristics of the CTs. The original CT labels of 1-3, 4-5 and 6-7 of Schwander et al. (2017) has been changed to D1, D2 and D3 for the dry CTs with anticyclonic dominance over Central Europe, N1 and N2 for the neutral (weak pressure gradient) CTs and W1 and W2 for the wet CTs, respectively (c.f. Table 4.2). The average mean sea level pressure (Figure 4.1a) clearly indicates the anticyclonic features over Central Europe of the three dry CTs. They differ in terms of the location of the anticyclone center. The center of D1 is located right over the Alps, that of D2 is shifted towards the British Isles inducing easterly flows and the center of D3 is located over the Balkans generating westerly flows towards the Alps. D2 and D3 show no pronounced annual cycle of monthly frequency and precipitation, in contrast to D1 which exhibits the strongest annual cycle of all CTs with high frequencies in winter (e.g. 10 days per month on average in December) and nearly no occurrence in summer. N1 exhibits prevailing Northeasterly flows induced by low pressure patterns in the central and eastern Mediterranean and high pressure over the eastern Atlantic. In contrast, N2 is zonally flow dominated (West-southwest) with low pressure over the British Isles and high pressure in the eastern Balkans. The monthly frequencies during the year of N1 and N2 are similar, peaking during the warm season, but the average monthly precipitation does not vary during the year. The two wet CTs exhibit widespread low pressure across Central Europe. W1 shows prevailing meridional, northerly flows while W2 shows more zonal, westerly flows south of the Alps. Monthly frequencies vary with W1 being more frequent in spring and summer, and W2 being more frequent in autumn and winter to early spring.

Table 4.1 Drought event characteristics. Mean drought intensity and drought severity are dimensionless measures of space-time precipitation anomalies (see Haslinger & Blöschl, 2017), where drought severity is mean drought intensity times the duration; average precipitation is the observed precipitation averaged over the GAR divided by the duration in days, average precipitation deficit is the average precipitation divided by the climatological mean for the months under consideration, accumulated deficit is the average precipitation deficit times the duration in days.

Event	Date	Duration [months]	Season	Peak	mean drought intensity [-]	drought severity [-]	average precipitation [mm/d]	average precipitation deficit [mm/d]	accumulated precipitation deficit [mm]
1822	Jan 1822 - Aug 1822	8	cold	Mar 1822	776	4655	2.27	-0.53	-127
1832	Apr 1832 - Nov 1832	8	warm	Sep 1832	765	4589	2.53	-0.69	-167
1834	Feb 1834 - Jul 1834	6	cold	Mar 1834	1679	6715	1.92	-0.94	-169
1835	Jul 1834 - Feb 1835	8	cold	Oct 1834	858	5145	2.25	-0.70	-167
1852	Dec 1851 - Jul 1852	8	cold	Apr 1852	1027	6159	2.08	-0.67	-162
1854	Oct 1853 - Jun 1854	9	cold	Mar 1854	952	6666	2.40	-0.46	-123
1858	Sep 1857 - Apr 1857	8	cold	Jan 1858	1234	7403	2.00	-0.81	-195
1861	Nov 1860 - Dec 1861	14	warm	Sep 1861	652	7819	2.48	-0.48	-201
1865	Feb 1865 - Jul 1865	6	warm	May 1865	1573	6291	1.97	-0.89	-161
1866	Jul 1865 - Feb 1866	8	cold	Dec 1866	864	5186	2.35	-0.60	-144
1870	Dec 1869 - Sep 1870	10	warm	Apr 1870	1040	8322	2.40	-0.44	-131
1872	Jul 1871 - May 1872	11	cold	Sep 1871	553	4977	2.52	-0.37	-121
1874	Oct 1873 - Jun 1874	9	cold	Jan 1874	855	5985	2.36	-0.50	-134
1880	Oct 1879 - Mar 1880	6	cold	Feb 1880	1180	4719	1.68	-1.05	-188
1882	Oct 1881 - Jun 1882	9	cold	Dec 1881	1074	7517	2.16	-0.70	-188
1884	Apr 1883 - Sep 1884	18	cold	Feb 1884	429	6856	2.65	-0.37	-201
1890	Nov 1889 - Apr 1890	6	cold	Jan 1890	1119	4477	1.87	-0.77	-139
1898	Sep 1897 - Mar 1898	7	cold	Dec 1897	882	4412	2.42	-0.39	-81
1909	Aug 1908 - May 1909	10	cold	Nov 1908	727	5814	2.23	-0.64	-191
1921	Aug 1920 - Feb 1922	19	cold	Oct 1921	977	16610	2.24	-0.69	-394
1925	Sep 1924 - Mar 1925	7	cold	Dec 1924	1121	5605	2.18	-0.63	-133
1946	Jul 1945 - Jan 1947	19	warm	Apr 1946	438	7442	2.55	-0.42	-239
1947	Apr 1947 - Nov 1947	8	warm	Sep 1947	1130	6777	2.38	-0.84	-202
1949	Sep 1948 - Apr 1949	8	cold	Jan 1949	1419	8513	1.79	-1.02	-244
1952	Feb 1952 - Sep 1952	8	warm	Jun 1952	855	5130	2.56	-0.38	-90
1953	Aug 1953 - Feb 1954	7	cold	Nov 1953	1197	5984	2.16	-0.77	-161
1962	May 1962 - Jan 1963	9	warm	Jul 1962	920	6442	2.65	-0.43	-117
1971	Apr 1971 - Dec 1971	9	warm	Sep 1971	840	5877	2.42	-0.73	-196
1976	Dec 1975 - Aug 1976	9	warm	May 1976	773	5410	2.22	-0.57	-155
1985	Jul 1985 - Dec 1985	6	cold	Sep 1985	1299	5197	2.27	-0.90	-163
1989	Jul 1988 - Mar 1989	9	cold	Dec 1988	729	5106	2.27	-0.60	-161
1990	Jul 1989 - Mar 1990	9	cold	Nov 1989	1037	7258	2.36	-0.51	-137
1993	Nov 1992 - Jul 1993	9	cold	Feb 1993	830	5808	2.46	-0.37	-101
2003	Jan 2003 - Sep 2003	9	warm	Mar 2003	1535	10742	1.87	-0.99	-268

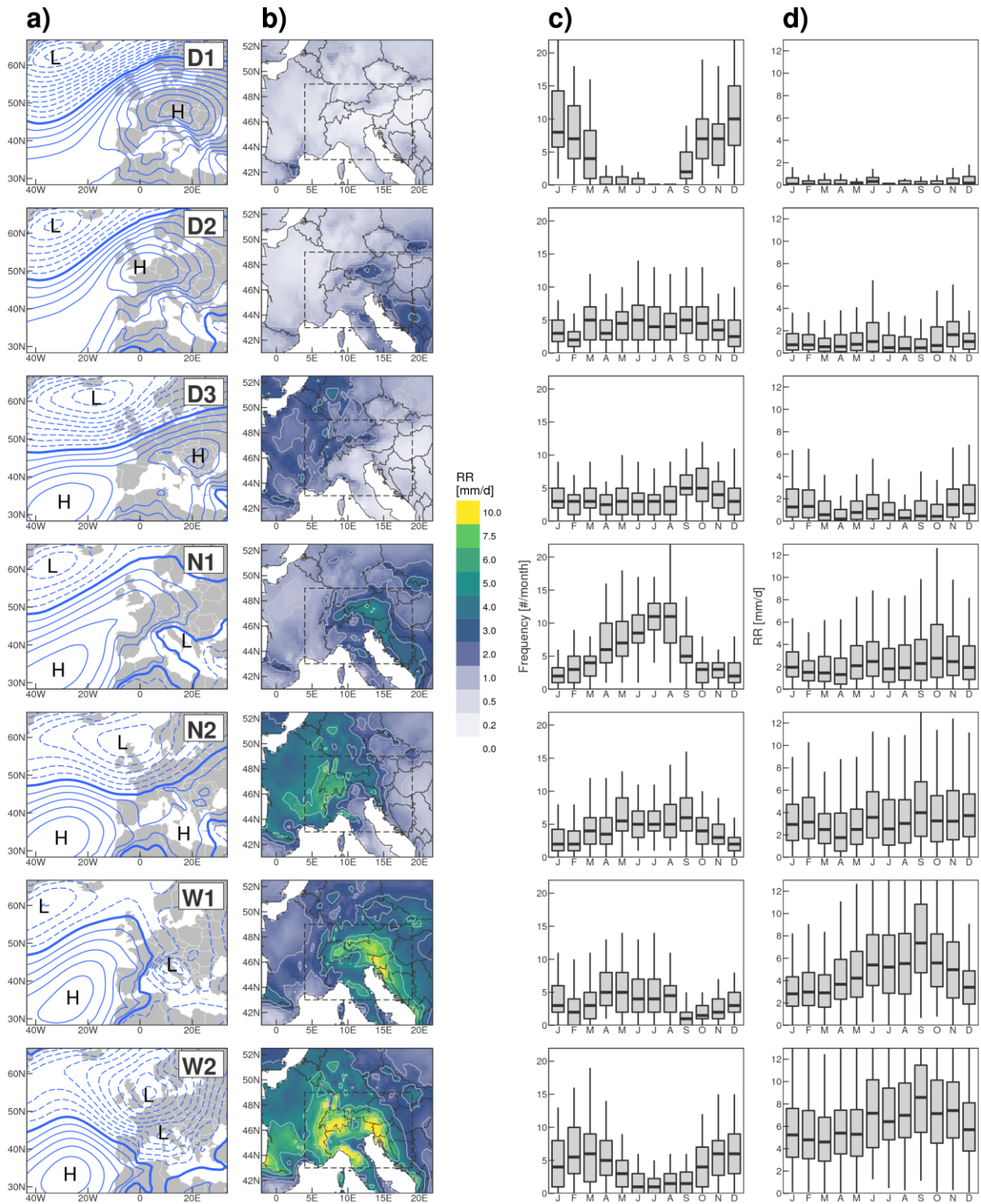


Figure 4.1 Characteristics of the (Schwander et al., 2017) circulation types (CT): mean sea level pressure based on 20CR, 1950-2009 (a), average precipitation based on E-OBS data, 1950-2009 (b), monthly frequency (days per month) (c) and mean daily precipitation sum averaged over the GAR based on E-OBS data, 1950-2009 (d).

Table 3.2 Characteristics of the (Schwander et al., 2017) circulation types (CT). RR indicates precipitation.

Abbreviation	Synoptic characteristics	cyclonic / anticyclonic	Prevailing Flow	Average RR [mm/d]	Frequency Peak [month]
D1	High pressure over Central Europe	anticyclonic	-	0.5	Dec
D2	Indifferent Easterly flow	anticyclonic	E	1.3	Jul
D3	Westerly flow over Northern Europe	anticyclonic	W	1.4	Sep
N1	Indifferent Northeasterly flow	indifferent	NE	2.7	Aug
N2	West-southwesterly flow, cyclonic, flat pressure	indifferent	WSW	3.6	Sep
W1	Northerly flow, cyclonic	cyclonic	N	4.9	Apr
W2	Westerly flow over Southern Europe, cyclonic	cyclonic	WC	6.4	Feb

The precipitation (RR) in Table 4.1 has been derived from the GAR gridded monthly precipitation dataset (Efthymiadis et al., 2006) over the period 1801-2010 (updated by HB17). Air temperatures have been derived from an updated version of the GAR gridded monthly temperature dataset (Chimani et al., 2013) over the period 1801-2010. In addition we used daily mean temperature and precipitation grids from the E-OBS database (Haylock et al., 2008) from 1950-2010. Since we compare the E-OBS data with the monthly GAR data, a bias correction of both temperature and precipitation is necessary. We consider the GAR data as the reference since it served as the basis for the drought event detection by HB17. In a first step the E-OBS data was bi-linearly interpolated onto the GAR-grid. Next we added a correction term to the daily temperature grids and applied a multiplicative correction term to the daily precipitation grids. These correction terms were estimated from the monthly biases of the E-OBS precipitation totals and temperature means with respect to the GAR-data.

We also used data (500 hPa geopotential height, mean sea level pressure, 300 hPa wind speed) from the 20th Century Reanalysis project (20CR, Compo et al., 2011) from 1851-2010 as well as the NOAA Extended Reconstructed Sea Surface Temperature (SST) V4 (Huang et al., 2015). Finally, we used three atmospheric and oceanic circulation indices: the monthly North Atlantic Oscillation Index (NAO, Jones et al., 1997), a reconstruction of the monthly Eastern Atlantic/Western Russia Index (EAWR, Poirier et al., 2017), and the monthly Atlantic Multidecadal Oscillation Index (AMO, Enfield et al., 2001).

The analysis in this chapter is based on two main metrics. The first is the frequency anomaly of anticyclonic CTs (ACT), which is calculated for every single drought event as

$$ACT_{ANOM} = \frac{f_{event}}{f_{elim}} \quad (4.1)$$

where ACT_{ANOM} is the frequency anomaly of the ACTs (D1, D2, D3) for a particular drought event, f_{event} is the observed frequency of ACTs during that event and f_{clim} is the long term (1801-2010) climatological mean frequency of ACTs. Values above (below) unity indicate more (fewer) days with ACTs than the climatological mean.

The second metric is termed precipitation efficiency (RR_{eff}) of a day with respect to the circulation type c of the day. It is calculated as

$$RR_{eff} = \frac{RR_{OBS}}{RR_{CT}} \quad (4.2)$$

$$\overline{RR_{CT}}(c, m) = \frac{1}{n} \sum_{i=1}^n RR(c, m) \quad c \in [1; 7] \quad m \in [1; 12] \quad (4.3)$$

where RR_{OBS} is the observed average precipitation over the GAR on a given day, and $\overline{RR_{CT}}$ is the mean average daily precipitation over the GAR for the particular circulation type c during the respective month m of the year. Values above (below) unity indicate more (less) precipitation on that particular day than expected from the climatological mean for the month of year and CT.

RR_{CT} is calculated from the bias corrected daily E-OBS fields (1950-2009) using equation 4.3, where n is the number of times CT c is observed in month m during the 1950-2009 period, and $RR(c, m)$ is the respective precipitation on that days. Precipitation efficiency could also be assessed on a daily basis where daily precipitation data is available, but in this chapter we mostly use event-based precipitation efficiency averaged over the whole duration of a given event. Only for the analysis of precipitation efficiency in relation to preceding soil moisture conditions during summer the analysis was conducted on a daily basis, but only for the 1950-2009 time period where E-OBS data is available.

The relationships between average precipitation deficit during drought events, ACT anomaly and large scale atmospheric and oceanic indices were assessed by simple and multiple ordinary least squares linear regression models (c.f. Wilks, 2011) on an event basis, but also seasonally stratified.

4.3 Results

4.3.1 Drought driver #1: Atmospheric circulation

One would, quite obviously, expect drought events to be associated with an above average frequency of dry CTs. The frequency anomalies of the CTs during drought events (Figure 4.2a) indeed change from positive to negative, as one moves from dry to wet CTs. D1 shows a median anomaly of 1.5, indicating a 50% frequency increase from the mean, in contrast to W1 and W2 which show an about 30% decrease. The spread of the boxplots is rather large, suggesting that some drought events have a below average frequency of dry CTs. The frequency anomalies of the Anticyclonic CTs (D1, D2 and D3, ACTs thereafter) of the drought events are significantly correlated with the average precipitation deficits (Figure 4.2b) (F-test of linear regression with p -value < 0.01), and a linear regression model explains 38% of the variance of the precipitation deficit (see Table 4.3).

Table 4.3 lists the variance of average precipitation deficit (averaged over the duration of the event and over the GAR) explained by regressions with the frequency anomaly of ACTs, and the Index values of the NAO, the EAWR, and the AMO and various combinations of them, both on a seasonal basis and per event. No significant collinearity was found among the different indices, the variance inflation factor is < 2 for all variables. For the seasonal stratification subsets of events which cover the respective season entirely are used (e.g. for an event stretching from January to May, spring is used for the seasonal assessment as it is fully covered (March-April-May), winter is not considered, since December is no drought month). ACT anomaly shows the largest explained variances in winter (0.50) and spring (0.66) and considerably lower values in autumn (0.37) and summer (0.15). NAO and AMO have very low predictive skill with explained variances ranging between 0.00 and 0.14. In contrast, the EAWR shows values of up to 0.57 (spring), which is nearly the explained variance obtained from the ACT anomaly. This may be due to the resemblance of the pressure patterns associated with the positive phase of the EAWR (c.f. Ionita, 2014) and the pressure patterns of D1 and D2. However, on an event basis (i.e., neglecting the season), the explained variance is considerably lower (0.16).

If multiple predictors are considered, the explained variance increases to 0.80 in spring using ACT anomaly and AMO as predictors, and even up to 0.92 if all four predictors are used. In winter these values are somewhat lower (e.g. 0.65 for ACT anomaly and AMO, and 0.76 for all four predictors).

In summer there are no significant relationships with different predictor combinations, although they also tend to rise (0.47 using all four predictors). In autumn the explained variances are low as well, but at least two significant relationships arise, one with a combination of ACT anomaly + NAO (explained variance 0.40) and ACT anomaly + EAWR (explained variance 0.38).

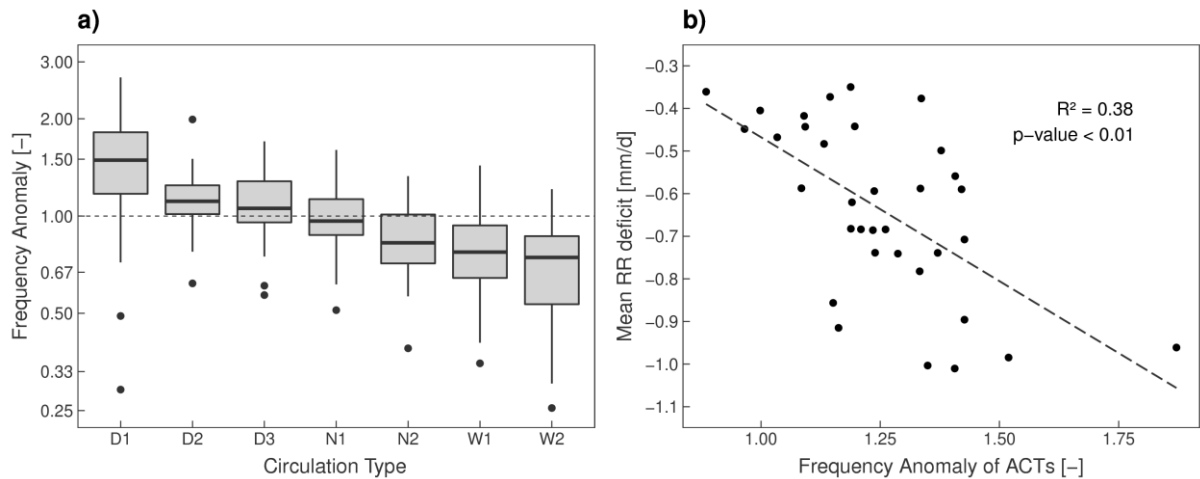


Figure 4.2 Circulation Type (CT) frequency anomalies (number of CT occurrences with respect to the long term mean 1801-2010) of individual drought events (a), and linear regression of frequency of Anticyclonic CTs (ACT anomaly, D1, D2, D3) with respect to the long term mean against the mean RR deficit during drought events (b).

These results highlight the importance of circulation anomalies as the main drivers of RR deficit in the cold season, whereas other effects may take over during the warm season, particularly during summer (JJA).

Table 4.3 Explained variances of mean precipitation deficit by different predictors (ACT anomaly, NAO-Index, EAWR-Index and AMO-Index) and predictor combinations on an event basis and on a seasonal basis (subsets of events which cover respective seasons entirely are used).

Note: Significance of the correlations at the 5% and 10% levels are indicated by ** (bold print) and *, respectively.

Predictor	Season				Event
	Winter (DJF)	Spring (MAM)	Summer (JJA)	Autumn (SON)	
ACT anomaly	0.50**	0.66**	0.15	0.37**	0.38**
NAO	0.13	0.00	0.12	0.02	0.00
EAWR	0.51**	0.57**	0.16	0.24*	0.16**
AMO	0.01	0.01	0.14	0.06	0.00
ACT anomaly, NAO	0.57**	0.70**	0.27	0.40**	0.41**
ACT anomaly, EAWR	0.63**	0.76**	0.27	0.38**	0.40**
ACT anomaly, AMO	0.65**	0.80**	0.45	0.41*	0.44**
EAWR, NAO	0.56**	0.51**	0.28	0.24	0.05
EAWR, AMO	0.58**	0.50**	0.19	0.26	0.10
ACT anomaly, EAWR, NAO	0.65**	0.82**	0.40	0.40*	0.40**
ACT anomaly, EAWR, NAO, AMO	0.76**	0.92**	0.47	0.41	0.50**

The circulation anomalies quantified by the circulation type classification are of course embedded in the larger scale (North Atlantic/European) flow patterns and also resemble to some extent the particular CTs. For instance, CTs D3 and N2 depict a likewise NAO+ phase with westerly flow and meridional pressure gradients, whereas CT D2 is like an EAWR+ pattern with high pressure near the British Isles. As noted by Ionita (2014) and Kingston et al. (2015) the EAWR pattern, which is a zonal pressure pattern showing positive pressure anomalies in NW-Europe during its positive phase, is related to droughts in Europe, which is in line with our findings for the GAR in winter and spring (Table 4.3). Other authors have suggested that the NAO is an important driver for European scale droughts (Hannaford, et al., 2011; López-Moreno & Vicente-Serrano, 2008), however, this relationship does not unfold for the GAR, as can be seen from the rather low precipitation deficit variance explained by NAO (Table 4.3). To better understand the interrelationships between these two large scale circulation patterns, the NAO and the EAWR, and the implications for the weather in the GAR, Figure 4.3 displays the atmospheric flow conditions (z500 anomalies and jet stream wind speed) intended for distinct NAO and EAWR conditions. This means that only those months are considered and averaged where the NAO and/or EAWR phase is below (NAO-, EAWR-) or above (NAO+, EAWR+) one standard deviation on order to get more distinct differences of the atmospheric flow.

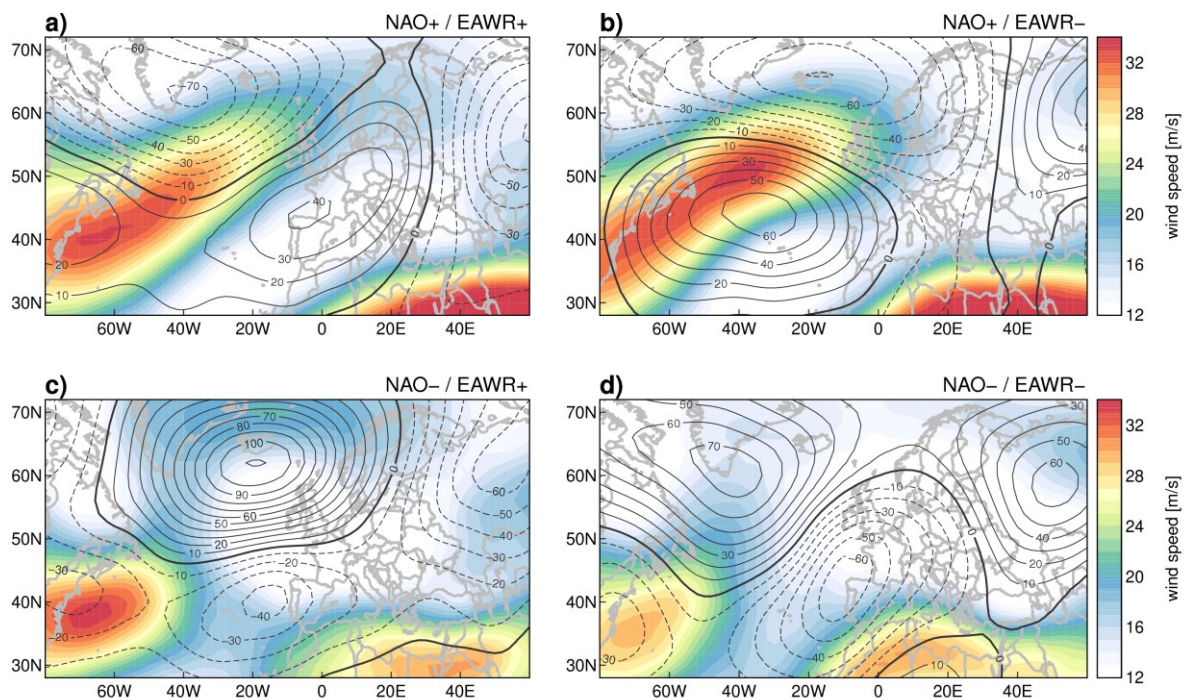


Figure 4.3 Geopotential height at 500 hPa (z500) anomalies (contours, solid line = positive anomalies, dashed line = negative anomalies) and jet stream wind speeds at 300 hPa (color shading) stratified by combined NAO/EAWR phases, NAO+/EAWR- (NAO-/EAWR+) indicates index values above (below) 1 standard deviation in winter/spring (JFMAM).

Figure 4.3a shows the conditions for both NAO and EAWR in its positive mode. Due to the positive NAO, prominent meridional pressure gradients emerge over the North Atlantic with a particular active jet stream region. The prevailing flow is from Southwest over the British Isles towards Scandinavia, and positive Geopotential height at 500 hPa (z_{500}) anomalies emerge in Southwestern and Central Europe. These patterns generate wet conditions in Northern Europe, whereas Central Europe (including the GAR) and the Mediterranean are rather dry. This is also reflected by the similarity of this circulation pattern to the average circulation patterns of D1 (see Figure 1), the driest CT. On the other hand, if the NAO is in its positive mode and the EAWR is negative (Figure 4.3b) the prevailing flow has no south component when reaching Europe, thus approaching straight from the West with an even more enhanced jet stream over the North Atlantic, and the z_{500} anomalies being negative over Central Europe. The reason for this pattern is the negative phase of the EAWR which is associated with negative pressure anomalies around the Eastern Atlantic, favoring a direct westerly flow. These subtle differences of the atmospheric flows have profound implications for generating precipitation in the GAR. The modulation of the flow direction of the jet stream downstream of the transect where the NAO-Index is calculated (pressure difference between Gibraltar and Southwest Iceland) in a strong positive NAO phase is modulated by the EAWR phase and thus drives the cyclonic activity in Central Europe and determines dry or non-dry conditions in similarly positive NAO phases.

Negative NAO and positive EAWR conditions (Figure 4.3c) are associated with reduced zonal flow over Europe and positive z_{500} anomalies over the North Atlantic and blocking like conditions over Northwestern Europe, which resembles the circulation patterns of D2 (see Figure 4.1). As illustrated by Ionita (2014), the jet stream splits up during these situations over the North Atlantic and merges towards the South with the subtropical jet and the Northern streak being far deflected towards Iceland and the Norwegian Sea. This enhanced meridional flow and absence of jet stream activity is well related to dry conditions in much of Europe and the GAR (Ionita, 2014). Finally, if both circulation modes are in their negative phase, meridional flow in combination with cyclonic activity over Western and Central Europe prevails, leading to wet conditions in this respect (Figure 4.3d).

4.3.2 Drought driver #2: Precipitation efficiency

As demonstrated above, anticyclonic circulation anomalies explain much of the variability of precipitation deficit during the drought events. However, this is only the case in winter and spring. In autumn and summer, other drivers are more important.

We therefore hypothesize that the combined effect of a circulation anomaly in combination with reduced precipitation efficiency, is driving an observed RR deficit. It could either result from a positive ACT anomaly alone with wet CTs, however bringing sufficient precipitation

but being outnumbered by the precipitation deficit of ACTs (RR efficiency ~ 1). Or it could occur at normal ACT conditions when wet CTs bring insufficient precipitation (RR efficiency < 1). This in turn leads to the assumption that a RR deficit is larger the larger the spread between ACT anomaly (> 1) and precipitation efficiency (< 1).

Figure 4.4 shows the ACT anomaly (circles) and precipitation efficiency (triangles) for every event, with the color shading indicating a warm season event (red) or a cold season event (blue), and the color intensity indicating the mean RR deficit during this event. For each event mean drought intensities were estimated for that part of the event that fell into a season (cold season from November to April, warm season from May to October) and the event was assigned to the season with the highest intensity.

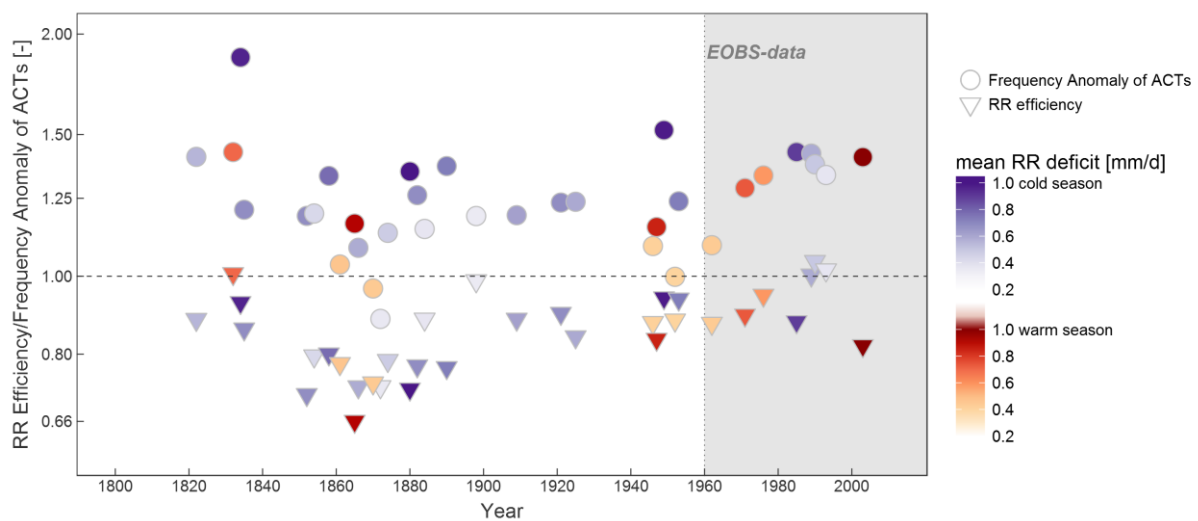


Figure 4.4 Frequency anomaly of ACTs and precipitation (RR) efficiency during drought events. Red (blue) patches indicate frequency anomaly (precipitation efficiency) by the location along the y-axis (log10), the color shading gives the mean RR deficit during the event.

When interpreting the results one has to keep in mind that the mean precipitation per CT and month used for estimating precipitation efficiency (Eq. 4.2) is based on the time period 1961-2010 (E-OBS data). During this period, eight events were observed, four in each season. The cold season events are characterized by ACT anomalies above 1.25 (mean ACT anomaly 1.39) and a mean precipitation efficiency of 0.99. This means that these events are driven mainly by circulation anomalies. For events in the warm season, the mean ACT anomaly is 1.28 and the mean precipitation efficiency is 0.88, which is considerably lower than the respective values of the cold season events. The lower values of precipitation efficiency in summer are likely related to soil moisture-precipitation feedbacks during the summer months (c.f. Seneviratne et al., 2010). Due to the convective characteristics of summer time precipitation formation, local conditions of moisture sources (soil) are of higher importance, which in turn leads to lower precipitation efficiency if soil moisture states are already low from preceding spring (Koster et al., 2017; van der Linden et al., 2018). This process was of particular importance in the 2003

event which started in late winter, exhibited positive ACT anomalies during spring (1.94 in MAM) leading to soil moisture deficits in early summer and then through a soil moisture atmosphere coupling to considerably low precipitation efficiency (0.54 in JJA).

Before 1960, similar patterns emerge. The events during the 1940s and 1950s show lower precipitation efficiencies than average (< 1) during warm season events and higher ACT anomalies than average (> 1) during cold season events. The second half of the 19th century (1851-1900), however, is characterized by substantially lower RR efficiencies for both warm and cold season events (mean precipitation efficiency of 0.78 from 1851-1900). The ACT anomalies vary substantially from less than 0.9 to almost 1.5. In the 1860s, ACT anomalies were particularly low; two events had even fewer ACTs than expected from the climatology. The RR efficiencies in this time period were the lowest in the entire data set. Interestingly, these strong anomalies occur in both seasons, which implies that this finding does not support the above hypothesis of higher precipitation efficiency anomalies during warm season events being due to a soil moisture - precipitation coupling.

In order to better understand this coupling we analyzed the precipitation efficiency in summer (JJA) as a function of the circulation characteristics and the soil moisture conditions. We used the Climatic Water Balance (CWB) on a 3 month (90 days, right sided) time scale averaged over the GAR as a large scale proxy for soil moisture conditions (Herold et al., 2016; Müller & Seneviratne, 2012; Whan et al., 2015). The CWB is calculated from the E-OBS daily fields of precipitation and a Hargreaves estimate of potential evapotranspiration from minimum and maximum air temperature (Hargreaves, 1975; Hargreaves & Allen, 2003). For every day-of-year during the summer months (JJA, 92 days in total) the 10th percentile of the CWB is determined from the empirical cumulative distribution function. By extracting days where the CWB is below this threshold we retrieve those where the CWB is an extremely dry state compared to the long term (1961-2010) mean. The precipitation efficiency of the subsequent days is displayed in Figure 4.5, stratified by CT.

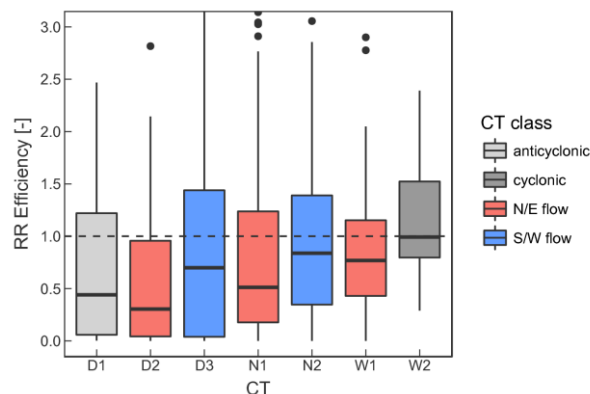


Figure 4.5 Daily precipitation efficiency in summer (JJA) stratified by CT using only those days when the preceding (one day before the actual day) accumulated 90-day CWB was below the 10th percentile (extremely dry conditions).

The lowest RR efficiencies occur for D1 and D2, although D1 is not very frequent in summer (see Figure 4.1) so this estimate has to be treated with caution. The precipitation efficiency of D2 is much lower than that of D3. Similarly, the precipitation efficiency of N1 is lower than that of N2 and also lower than those of W1 and W2. The differences arise from the prevailing flow conditions, which are predominantly westerly for the less sensitive CTs (D3, N2) and northerly to easterly for the more sensitive CTs (D2, N1, W1). CTs D3 and N2 are circulation patterns where large scale zonal flow with distinct pressure gradients allows large scale moisture transport from the Atlantic. On the other hand D2, N1 and W1 show a flatter pressure distribution, less zonal and enhanced meridional flow, favoring the formation of local convection and thus being more sensitive to preceding soil moisture conditions.

Table 4.4 The summers of 1962 and 2003 in comparison (precipitation, precipitation efficiency, temperature) stratified by CT; particularly large differences between variables of those two summers are highlighted by bold print.

CT	D2 (E)		D3 (W)		N1 (NE)		N2 (WSW)		W1 (N)		W2 (WC)	
	1962	2003	1962	2003	1962	2003	1962	2003	1962	2003	1962	2003
Precipitation [mm/d]	0.4	0.1	0.3	0.6	1.2	1.2	2.2	1.5	4.8	4.1	5.1	7.3
Precipitation eff. [-]	0.28	0.08	0.21	0.72	0.42	0.47	0.62	0.37	0.81	0.69	0.68	0.92
Temperature [°C]	18.3	21.8	18.7	23.4	16.6	20.7	19.7	21.3	16.1	20.3	17.3	20.9

The 2003 event is in many respects a benchmark event (Laaha et al., 2017) for future climate change conditions, as we expect it was primarily driven by reduced precipitation efficiency due to a negative soil moisture-precipitation feedback (Black et al., 2004; Fink et al., 2004). However, as reported by HB17, the summer of 2003 was topped by the summer of 1962 in terms of average precipitation deficit, with the remarkable difference that 1962 was cooler than average (-0.4 °C). From a process perspective, the soil moisture precipitation feedback is tied to an increasing sensible heat flux over time at the expense of latent heat flux, forcing temperatures to rise and convection to be suppressed (Seneviratne et al., 2010). But this was not the case in the summer of 1962. Table 4.4 shows a summary of average precipitation (RR), precipitation efficiency and temperature stratified by CTs for both summers. The precipitation efficiency for D2 (most sensitive to soil moisture precipitation feedback, see Figure 5) in 2003 was much lower (0.08) than that in 1962 (0.28). In contrast, the CTs less sensitive to soil moisture precipitation feedbacks exhibit lower RR efficiencies during the 1962 summer, e.g. 0.21 for D3 (2003: 0.72) and 0.68 for W2 (2003: 0.92).

These differences are related to the atmospheric circulation and regional sea surface temperature (SST) anomaly patterns as illustrated in Figure 4.6. In 1962 (Figure 4.6a) a dominant westerly flow approached Central Europe counteracting the weak high pressure anomalies in Southern Europe and the Mediterranean. In contrast, summer 2003 (Figure 4.6b) shows an extensive high pressure system over Western and Central Europe, blocking the

moisture supply from the Atlantic and therefore driving the local soil moisture precipitation feedback. The SST anomalies were strongly positive over vast areas across the North Atlantic, except for the area of persistent cyclonic activity south of Greenland. The SST patterns were quite different in 1962. The North Atlantic was rather cool, and in particular the North and Baltic Seas showed strong negative anomalies. Such patterns seem to significantly influence the precipitation efficiency of D3, N2 and W2, as less moisture is transported from these source regions due to cooler atmospheric and oceanic conditions. Comparing the precipitation efficiency of W2 dependent on warm (+1 °C anomaly) versus cold (-1 °C anomaly) conditions in the Atlantic and the North Sea (20° W-10° E and 40° N-60° N) revealed a mean precipitation efficiency of 1.01 for warm SSTs and 0.72 for cool SSTs, highlighting the importance not only of local soil moisture precipitation feedback altering precipitation efficiency but also large scale SST patterns.

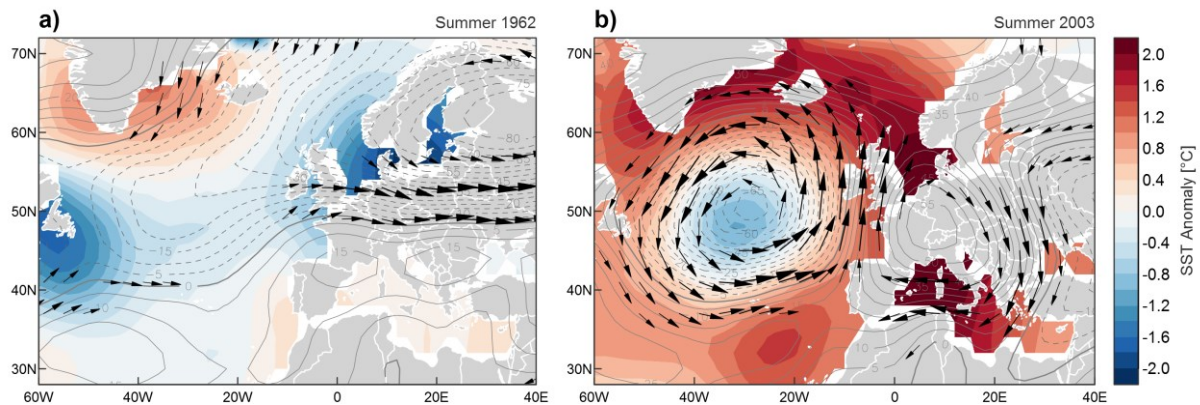


Figure 4.6 Sea surface temperature (SST) anomalies (color shading), geopotential height anomalies at 500 hPa (contours, 5 hPa interval) and 500 hPa wind speeds (arrows) during the summer of 1962 (a) and 2003 (b).

4.3.3 Similarities and differences of the drought decades of the 1860s and 1940s

The outstanding drought decades of the 1860s and 1940s have previously been explored either with a meteorological drought focus (Briffa et al., 2009; Brunetti et al., 2006; Haslinger & Blöschl, 2017; van der Schrier et al., 2006; van der Schrier et al., 2007) or a hydrological focus (Pekarova et al., 2006) with less emphasis on the atmospheric drivers. In order to get a better understanding of the general precipitation characteristics we shift our focus from the detected drought events to a broader view of the entire precipitation distribution.

Figure 4.7 compares the anomalies of two mean seasonal precipitation quantiles (0.2 and 0.8) aggregated to decades. This is done by at first estimating the seasonal 0.2 and 0.8 quantiles from the empirical cumulative distribution of the entire time period (1801-2010) and then estimating the seasonal 0.2 and 0.8 quantiles for every decade. The anomaly is the relative deviation of the seasonal quantiles of a decade from the long term (1801-2010) quantiles. Figure

4.7a shows the seasonal distribution of the long term 0.2 quantile (RRq20, dry tail). The graph points to a minimum in winter (DJF) and a maximum in summer (JJA), as would be expected, as rainfall in the GAR is summer dominated (Parajka et al., 2009). The respective seasonal anomalies per decade of RRq20 (Figure 4.7b) show that the winters (DJF) of the 1860 and 1940s were not the driest on record. In contrast, the spring (MAM) anomalies are rather pronounced, particularly in the 1940s, which is also the case for the summer and autumn anomalies. On average over the seasons (Fig. 4.7c), the 1940s were exceptional in terms of RRq20 anomalies, but the 1860s less so.

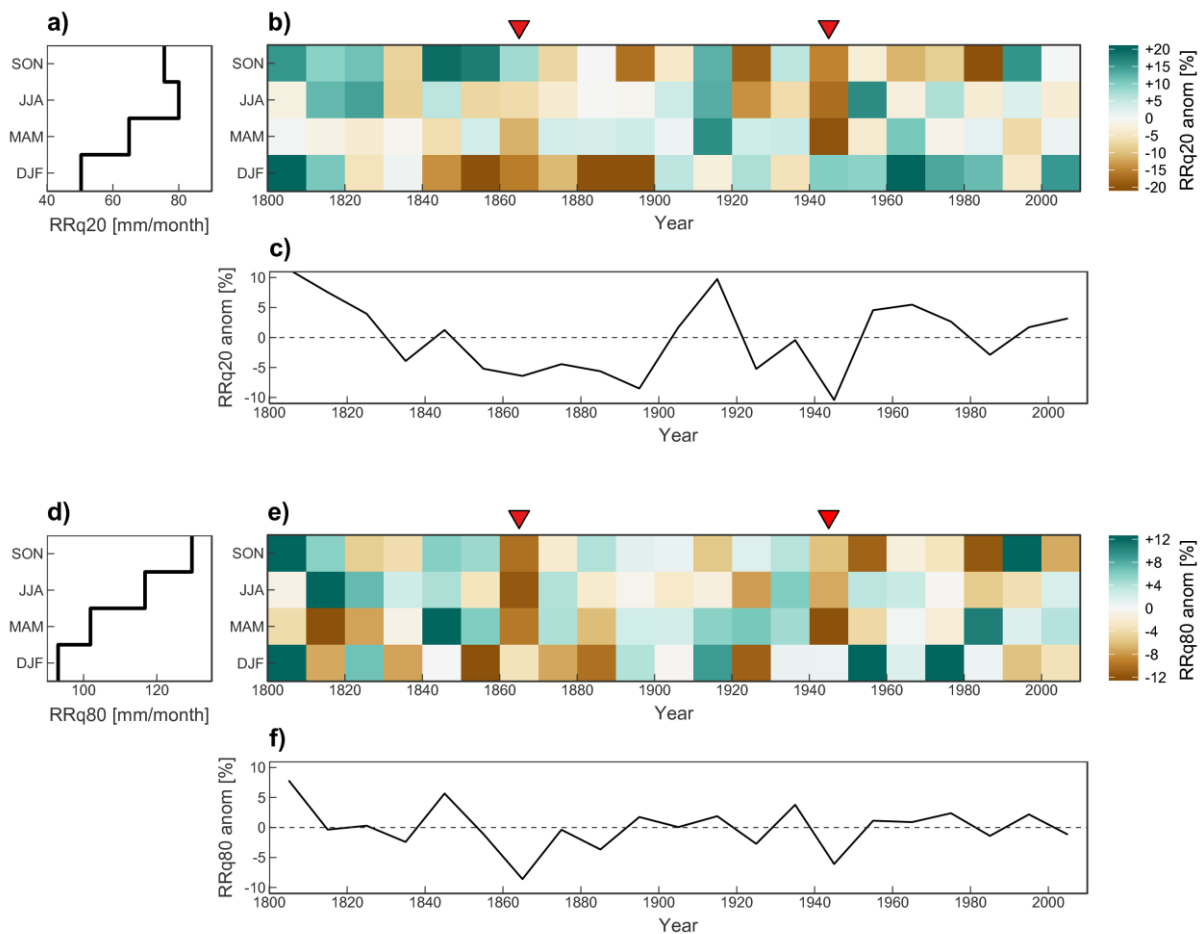


Figure 4.7 Long term (1801-2010) monthly 0.2 quantile (dry tail) precipitation stratified by season (a), anomalies (wrt. 1801-2010) of the decadal monthly 0.2 quantile precipitation stratified by season (b) and for the entire year (c); Analogous plots for the 0.8 quantile (wet tail) (d, e, f). All estimates are averages over the GAR. Red arrows indicate outstanding drought decades.

The wet tail of the distribution (0.8 precipitation quantile, RRq80) in Figure 4.7d shows gradually increasing precipitation from winter to autumn. The anomalies (Fig. 4.7e,f) are characterized by high fluctuations during the winter, but the strongest anomalies do not occur the 1860s and 1940s. However, in spring negative anomalies are pronounced in the 1860s and

particularly large in the 1940s. The summers are similar, although the signal in the 1860s was much stronger than that in the 1940s. This result is in line with findings of HB17 who found drought events with longer durations during the 1860s, which is a consequence of the absence of extraordinarily wet months. This is not the case for the 1940s events which show, on average, shorter durations through event break-ups caused by extraordinarily wet months.

It seems that spring is the key season for understanding the emergence of outstanding drought decades as it showed the strongest anomalies throughout the last 200 years for both the wet and dry tail quantiles. General circulation characteristics are displayed in Figure 8 as of the 500 hPa geopotential height anomalies (z_{500} , upper level) and the mean sea level pressure anomalies (slp, surface level) during extended springs (FMAM) of the 1860s (1861-1875) (Fig. 4.8a) and the 1940s (1941-1955) (Fig. 4.8b). First of all, the two pressure patterns look quite different, implying rather different atmospheric driving mechanisms. The 1860s are characterized by weak upper level blocking in the Norwegian Sea and generally positive z_{500} anomalies in Southwestern Europe, contrasting with two negative anomaly areas south of Greenland and over Scandinavia. As can be seen in Figure 4, events during the 1860s show a weak circulation forcing; the frequency anomalies of anticyclonic CTs are relatively low (1.04 average), some events show even less ACTs compared to the climatology. This is confirmed by the negative pressure anomalies over the GAR (Figure 4.8b).

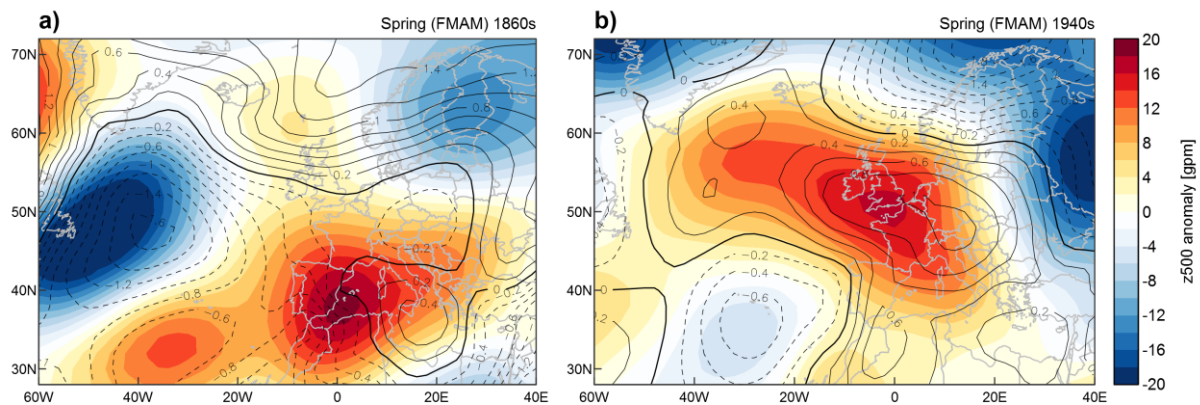


Figure 4.8 Geopotential height at 500 hPa anomaly (color shading) and mean sea level pressure anomaly (contours) over Europe and the North Atlantic in extended spring (FMAM) with respect to the long term mean (1851-2010) for the 1860s (1861-1875) and the 1940s (1941-1955).

Additional analyses (not shown) suggest that the 1860s springs were characterized by frequent and persistent cyclonic CTs (W1 and W2). This counterintuitive behavior might be explained by a recurring circulation regime as illustrated by a daily sequence (17 to 21 February, 1870) of sea level pressure maps in Figure 4.9. The circulation is characterized by a strong blocking over Iceland and cyclonic activity over the Azores, resembling a negative NAO-mode which is very similar to the mean state during the 1860s (see Fig. 4.8a). On the second day of the sequence (18 February) a low pressure system emerged over Scandinavia, propagating southwards towards the GAR during the following days with its center reaching the Adriatic Sea on 21

February. This cyclone track is rather uncommon given its area of generation and track evolution. In a recent analysis, Hofstätter et al. (2017) showed that these cyclone track types are rare, and precipitation totals in Central Europe associated with these tracks are lower than those of the other track types. Other examples of these circulation characteristics were identified by visual inspection of the sea level pressure fields during droughts in spring in the 1860s (not shown) which suggest that these are responsible for dry conditions even though cyclonic activity is present.

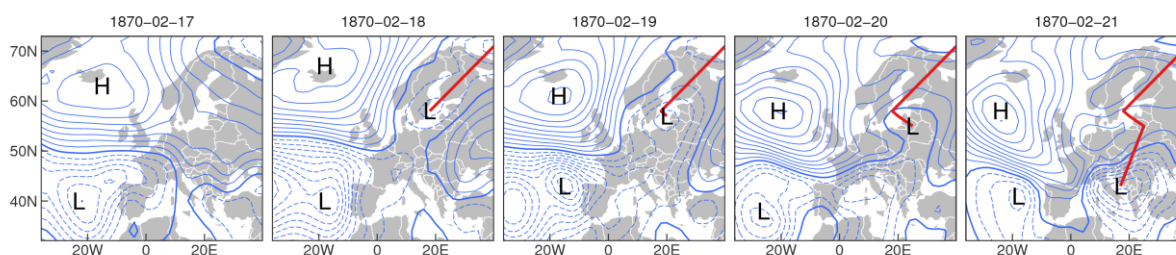


Figure 4.9 Daily sequence of mean sea level pressure over Europe and the North Atlantic (17 to 21 February, 1870), the main high (H) and low (L) pressure systems and the track of a low pressure system entering Central Europe from the Northeast (red).

The anomalous pressure patterns as shown in Figure 4.9 could be due to surface-atmosphere feedback processes in the higher latitude North Atlantic. Reconstructions of sea ice concentrations in the North Atlantic show a distinct peak of maximum sea ice extent during the 1860s and 1870s (Macias Fauria et al., 2010; Vinje, 2001; Lamb, 1995). Corresponding to the positive sea level pressure anomalies north of the British Isles (Figure 4.9) these anomalies might be caused by the large scale sea ice concentration during late winter/early spring, inducing a thermal high at the surface and weak blocking in the mid-troposphere (500 hPa).

Compared to the 1860s (Figure 4.8a), the spring atmospheric circulation characteristics of the 1940s (Figure 4.8b) differ significantly. The 1940s exhibit a pronounced positive pressure anomaly both at the surface and the upper level stretching from Ireland towards Southwestern and Central Europe, which strongly resembles a positive EAWR mode. This dominant anticyclonic and therefore likely dry situation is also confirmed by the large negative anomalies of the dry tail precipitation quantile (Figure 4.7b, 4.7c).

Analysing the EAWR in spring (Figure 4.10a) reveals an expectedly local maximum of the positive phase during the 1940s with the multidecadal evolutions of both the EAWR and the AMO (30-year Gaussian filter, thick lines in Figure 4.10a) seem similar. During 1900-1920 and 1970-1980 both indices are in negative phases, and during 1940-1960 they are in positive phases. The evolution of the EAWR seems therefore tied to SST in the North Atlantic, consistent with the association of cold North Atlantic SSTs and an enhanced Siberian High (and therefore a negative EAWR pattern) found by Wang et al. (2011).

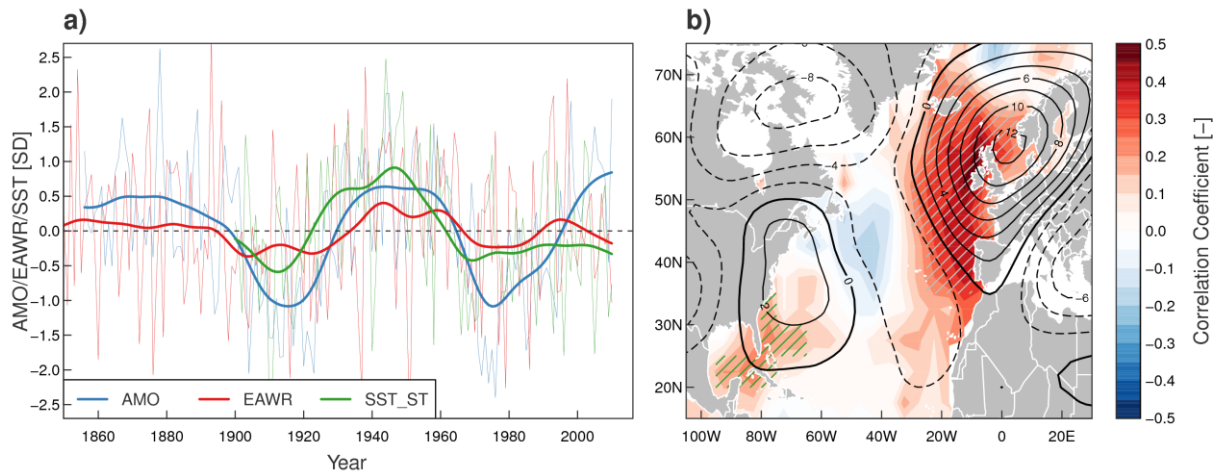


Figure 4.10 Time series of average late winter/spring (JFMAM) standardized Atlantic Multidecadal Oscillation Index (AMO, blue), the Eastern Atlantic/Western Russia Index (EAWR, red) and the detrended Sea surface temperature (SST) in the western subtropical Atlantic (60-80W and 20-40N, green) and 30-year Gaussian filtered time series (thick lines) (a); correlation between the EAWR and SST (color shaded areas) and 500 hPa geopotential height anomaly during the positive phase of the EAWR (contours), the hatched areas indicate significant (p -value < 0.05) correlation, the colors of the hatches (green, grey) indicate different causalities of the correlations (see text for details).

Using a Stationary Wave Model, Lim (2015) showed that positive SST anomalies in the western subtropical Atlantic result in diabatic heating in the mid-troposphere which in turn results in a Rossby-type wave that resembles the features of the EAWR. This causal chain is in good agreement with the time series of the EAWR (red) and the detrended SST in the subtropical western Atlantic (green) both peaking in the 1940s (Figure 4.10a). EAWR and the SSTs are significantly correlated in the subtropical western Atlantic (Fig. 10b), which is in good agreement with Lim (2015), and also in the mid-latitude eastern Atlantic. However, these two regions differ in terms of the mechanisms behind the correlations. As shown by Lim (2015) the positive SSTs in the western subtropical Atlantic and vorticity transients near the Atlantic jet region ($\sim 40^\circ\text{N}$, $\sim 40^\circ\text{W}$) are the forcings for a positive EAWR pattern, but other regions in the North Atlantic like east of 30°W and north of 40°N are clearly no forcing region, which indicates that the strong positive correlations between the EAWR and SSTs in Figure 10b (grey hatching) is a response to high pressure over Northwestern Europe induced prevailing southerly winds.

In the summer season (JJA) there is a similar signal as in spring, with the wet tail anomaly being more important in the 1860s and the dry tail anomaly more important in the 1940s (Figure 4.7b and 4.7e). We also found that positive frequency anomalies of anticyclonic CTs are not able to explain much of the observed rainfall deficit variability during droughts in summer (Table 4.3), however, certain CTs are more sensitive to preceding soil moisture conditions than others (Figure 4.5). A comparison of the relative frequencies of the sensitive CTs (D2, N1 and W1; N/E flow) with the less sensitive CTs (D3, N2; S/W flow) during summer is given in Figure 4.11. The 1860s and 1940s show a pronounced signal of an enhanced frequency of N/E flow CTs at the expense of S/W flow CTs. This means that the general flow

conditions are dominated by CTs that are characterised by flatter pressure gradients, potentially allowing for local convection, which in turn implies less large scale advection and thus less moisture transport from the Atlantic as a main moisture source. These atmospheric circulation conditions in combination with low soil moisture conditions from the preceding spring might drive a positive feedback which allows for a substantial build-up of precipitation deficit.

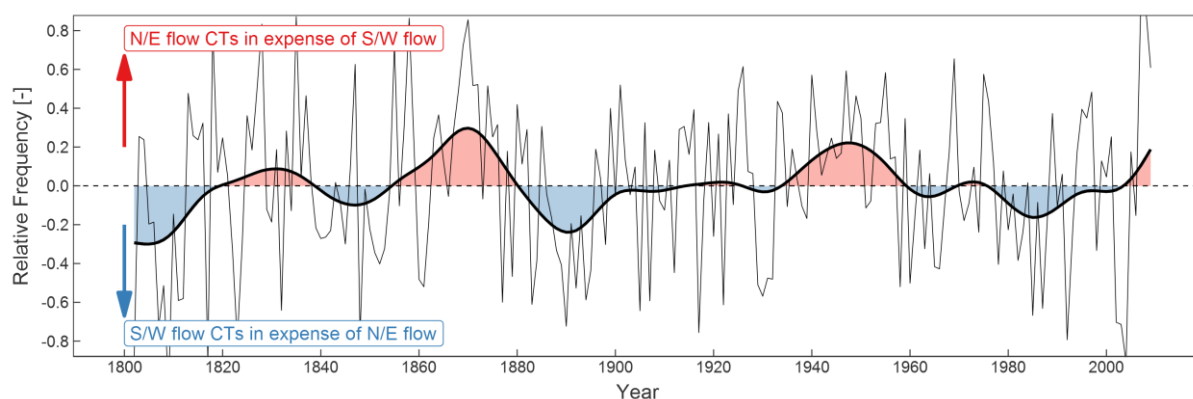


Figure 4.11 Time series of summer (JJA) relative frequency difference between north and easterly flows CTs (N1, D2, W1) and south and westerly flow CTs (N2, D3) (thin black line), and 30-year Gaussian filter (thick black line). Positive frequencies indicate enhanced N/E flows at the expense of S/W flows, negative frequencies indicate enhanced S/W flows.

4.4 Discussion

4.4.1 General remarks

For assessing the drivers behind the major drought events occurring in the GAR during the last 210 years we distinguish between atmospheric circulation and precipitation efficiency. Considering driver #1 (atmospheric circulation) we found that positive ACT anomalies (enhanced anticyclonic activity over Central Europe) are, not surprisingly, a main driver of drought conditions as noted by Kingston et al. (2015) and Trnka et al. (2009). More than one third (38%) of the variability of average event precipitation deficit can be explained by ACT anomaly. However, in winter and spring the explained variance is even higher, whereas there is no significant correlation in summer. These findings are consistent with other studies (e.g. Hannaford et al., 2011) that are based on large scale atmospheric indicators such as NAO.

A joint analysis of the ACT anomalies and their embedding in the large scale atmospheric flow in this chapter suggests that there is no correlation between the NAO and average rainfall deficit in any season, but there is a significant correlation with the EAWR in winter and spring. Ionita (2014) highlighted the relevance of the EAWR for explaining dryness and wetness in Central and Eastern Europe, which is confirmed here for the Greater Alpine Region.

We also found that driver #2 (precipitation efficiency) has a significant effect on precipitation deficit build-up. Precipitation efficiency gives the ratio between observed precipitation and expected precipitation for a particular time of year (e.g. month) and weather situation (CT). We hypothesize that precipitation efficiency is lower in summer if preceding soil moisture conditions are low and the atmospheric circulation shows weak pressure gradients enabling the formation of local convection and thunderstorms.

Our results confirm this hypothesis due to two aspects, the generally lower precipitation efficiency for local convection allowing CTs (c.f. Figure 4.5) and that the events peaking in the warm season show generally lower precipitation efficiency compared to cold season drought events in the recent 60 years. Although soil moisture - precipitation feedbacks are not straightforward to identify (Koster et al., 2017; Tuttle & Salvucci, 2017) our findings are in line with other publications (Findell et al., 2011; Guillod et al., 2015) which found evidence for a positive feedback during the warm season. Considering moisture sources for the Alpine region in particular, using a Lagrangian moisture source diagnostics model, Sodemann & Zubler (2009) found that there are distinct differences between seasons, with winter precipitation being mostly driven by large scale advection (continental moisture recycling < 10%) and summer precipitation showing considerably higher continental recycling rates of up to 50%. However, as the two driest summers during the last 210 years (1962 and 2003) show (Fig. 6), the soil moisture precipitation feedback is not necessarily the only driver modulating precipitation efficiency. Pronounced negative SST anomalies in the Eastern North Atlantic and the North Sea are most likely the reason for reduced precipitation efficiency in the summer of 1962, particularly for the CTs associated with North/Western advection due to reduced precipitable water content of the atmosphere. The North Sea was rather cool in summer of 1962, showing the second largest negative SST anomalies from 1950 to 2010, which highlights the special character of this summer drought.

The 1860s and 1940s are highlighted in the literature as decades with exceptional drought conditions in the GAR. Haslinger & Blöschl (2017) found that these time periods show highest intensities of precipitation deficit in a joint space-time assessment. These results are confirmed by van der Schrier et al. (2007) who analyzed soil moisture variability using the Palmer Drought Severity Index and concluded that the time periods from the 1850s to the 1870s and the 1940s to the early 1950s stand out as persistent and exceptionally dry periods. And also through a hydrological assessment these were found to be outstanding decades concerning streamflow anomalies in Central Europe (Pekarova et al., 2006). So far, little has been known on the drivers behind the 1860s and 1940s, although the necessity considering fundamental drought understanding is highlighted in Haslinger & Blöschl (2017).

In this study we are able to show that the drivers controlling the outstanding drought decade of the 1940s can be well explained by the processes associated with the other drought events in the entire 210 year period. The time period from 1940-1955 was dominated by a strongly positive anomalies of the EAWR in the late winters and springs, induced by positive SST anomalies in the western subtropical Atlantic (Lim, 2015). These were followed by positive

frequency anomalies during the summers of CTs that are sensitive to soil moisture-precipitation feedbacks, resulting in an enhanced frequency of droughts during this period. On the other hand, the processes driving the droughts of the 1860s are not as straightforward to understand. The most counterintuitive aspect is that ACT anomalies show no strong indication of enhanced anticyclonic activity. Moreover, some events show even less ACTs than the climatological mean. This signal is strongest during springs, when unusual cyclone tracks moving towards the GAR from the Northeast. Recent studies relating precipitation amounts to cyclone tracks (Hofstätter et al., 2016; Hofstätter et al., 2018) in the Alpine region found that this kind of tracks has been rather rare during recent decades and that the associated precipitation has been extremely low. The global background climate during the 1860s marked the end of the Little Ice Age which was rather different from the recent decades. It was a rather cold period throughout the Northern Hemisphere, with vast sea ice formation in the North Atlantic (Lamb, 1995; Vinje, 2001). The strongly positive sea level pressure anomalies during the springs of the 1860s in the North Atlantic found here may in fact have been due to sea ice formation altering the surface energy balance and inducing a thermal high near the surface. These anomalies reaching to the upper level (500 hPa) troposphere have likely blocked the westerly flows and therefore initiated the southwestward propagation of cyclones from the low pressure area over Scandinavia and Western Russia. Coupled atmosphere-ocean models could be used to further examine these potential mechanisms in future studies.

In addition, the analysis of the droughts in the 1860s also points towards some limitations of the methods applied in this chapter related to the concept of precipitation efficiency. The concept is likely applicable for the time period when the mean CT precipitation was estimated from E-OBS data, since the comparison between ACT anomaly and precipitation efficiency showed higher (lower) impact of the circulation in the cold (warm) season. But when going further back in time towards the 19th century equals a departure from the recent climate to rather different climate states which comes along with a diversification of processes controlling precipitation efficiency through altered atmospheric circulation dynamics (e.g. exceptionally low precipitation efficiency during Little Ice Age peak in the 1860s). The second limitation is the static concept of CT classifications which did not account for the antecedent atmospheric conditions, and thus the dynamics, of the circulation. The 1860s showed the lowest precipitation efficiency in the last 210 years, most likely due to the large number cyclones approaching the GAR from the Northeast and thus advecting little precipitation. However, these features are not accounted for, since the CT classification only classifies a given pressure pattern, but does not account for the previous conditions. These findings have profound implications for climate reconstructions in general. Most of the methods assume a stationary relationship between climate and proxy, and also for the use of CTs for reconstructing precipitation further back in time. The relationship between CT in a given month and the mean precipitation identified in recent times may not be applicable to the more distant past when different climate states occurred.

4.4.2 Implications for understanding future climate change

As pointed out by Mishra & Singh (2010), it is very important to understand historical droughts on regional scales to be able to better assess future drought processes in the wake of global climate change, since drought projections are associated with considerable uncertainty (see Haslinger et al. (2016) for the GAR). Over the last two centuries no trends in meteorological droughts (precipitation deficits) have been observed in the GAR (Haslinger & Blöschl, 2017), although soil moisture droughts have increased due to enhanced potential evapotranspiration associated with increasing temperatures, solar radiation and vegetation activity (Duethmann & Blöschl, 2018; van der Schrier et al., 2007). The results of this chapter suggest that the 1860s are not likely to occur in the near future, as they were closely related to the cool climate at the end of the Little Ice Age around 1850 (Matthews & Briffa, 2005) resulting in strong anomalies of the atmospheric circulation, particularly in spring.

On the other hand, the 1940s were forced by a particularly strong positive EAWR pattern in spring with its origin in positive SST anomalies in the subtropical western Atlantic and subsequent positive frequency anomalies in the summers of CTs that are sensitive to soil moisture - precipitation feedbacks. These mechanisms could likely happen in the near future, if ocean and atmospheric circulation dynamics favor enhanced warming in the western subtropical Atlantic, thus driving a positive EAWR phase. Although the outstanding drought decades of the 1860s and 1940s were rather different in terms of their drivers, they do highlight the importance of spring as the most influential season with regards to decadal-scale drought conditions. This finding has also been recently highlighted by van der Linden et al. (2018). Moreover, in both outstanding drought decades there was a similar above average frequency of N/E flow CTs in summer, which are more sensitive to soil moisture-precipitation feedbacks, at the expense of S/W flow CTs, enhancing the drought signal through reduced precipitation efficiency.

It is not clear whether this summer circulation regime would have developed regardless of preceding dry springs, or if it is a direct consequence of the preceding dry springs. The latter would have profound implications for future climate change, since springs are expected to become dryer (van der Linden et al., 2018) in Central Europe. On the other hand, Gagen et al., (2016) suggests that the storm track variability during the summers of the last millennium and its link to meridional temperature gradients (MTG) over Europe has not been driven by external forcing (e.g. aerosols, greenhouse gases) but has rather been a result of internal variability. They also identified two MTG extremes in the recent past, one during the 1910s with steep MTGs resulting in wet conditions and one during the 1940s with very weak MTGs triggering the 1940s outstanding drought decade.

4.5 Conclusions

In the present study we investigated the atmospheric drivers of extreme meteorological drought events in the Greater Alpine Region during the past 210 years using a daily atmospheric circulation type reconstruction tailored to the Alpine region. Our results suggest positive EAWR conditions as the main large scale atmospheric pattern related to anticyclonic circulation and therefore drought in winter and spring, while the NAO has no significant impact. In summer a positive soil moisture precipitation feedback is detected, which is strongest during weak pressure gradient local convection permitting circulation types. The events of the outstanding dry decades of the 1860s and 1940s were triggered by strong precipitation anomalies during spring and enhanced through soil moisture precipitation feedbacks during summer. The dry springs of the 1860s were caused by circulation characteristics that were quite different from those of recent decades as a consequence of the last peak of the Little Ice Age and the related large extent of the Arctic sea ice. The dry springs of the 1940s were related to positive sea surface temperature anomalies in the western subtropical Atlantic, triggering distinct Rossby wave trains leading to persistent positive EAWR circulation patterns. Future research will investigate drought development during the warm season in more detail, particularly the transition from spring (circulation dominated) to summer (feedback dominated), since there is evidence of a feedback not only between soil moisture and convective precipitation but also with the atmospheric circulation.

5. Summary and Conclusions

The aim of this doctoral thesis was to enhance the knowledge regarding the emergence of droughts (expressed as precipitation deficit) in space and time in the Greater Alpine Region (GAR) of Europe and to assess their atmospheric controls across different spatial scales over the past two centuries.

The following research questions are addressed:

- 1) What are the spatial patterns of droughts (expressed as precipitation deficit) on predefined time scales?
- 2) How can the space-time emergence of drought events be detected and how have drought features (frequency, duration, intensity and severity) changed over time?
- 3) What are the atmospheric drivers of drought events on various spatial scales?

These research questions are addressed in three chapters of this thesis. Chapter 2 explores the spatial characteristics of droughts and their changes over time using a traditional approach (Vincente-Serrano et al., 2012). We utilized gridded precipitation data to assess abnormally dry states in space which could subsequently lead to soil moisture, streamflow or groundwater drought. To account for the different time scales on which these effects may arise, the precipitation values are accumulated by a moving window approach over 3 month (3M), 6 month (6M) and 12 month (12M) time scales, similar to the procedure to calculate the Standardized Precipitation Index (SPI) on different accumulation time scales (see McKee et al., 1993). Instead of using the SPI, quantiles are used for setting up a drought threshold (0.2), since distribution fitting may introduce large uncertainties at the tails of the distribution. Contiguous areas below this quantile threshold in the GAR are detected as drought areas, and their severity is assessed by relating the average deviation from the threshold to the size of the drought area. A k-means clustering approach is applied to classify the spatial characteristics of the drought areas.

The long term perspective of more than 200 years of drought occurrence in the GAR revealed that the time periods of the 1850s to the 1870s and the 1940s were driest, as they exhibited both highest drought area frequencies and severities. Assessing the similarity between drought areas using k-means clustering shows three dominant sub-regions of drought occurrence which are different from previous regionalizations for the GAR (e.g. Auer et al., 2007). The Main Alpine Ridge appears to be a major climatic divide for droughts, which does not only apply to daily or monthly accumulation scales (c.f. Böhm et al., 2003) but also to multi-monthly time scales. An east/west dipole is also distinguishable but is less prominent. The frequency of drought area occurrence does not exhibit trends, but multidecadal variations are pronounced, particularly for high accumulation time scales. Interestingly, these variations over time manifest themselves differently in space. The north and west were more drought

prone in the middle of the 19th century, whereas the east of the GAR shows higher drought area frequency in the last decades. These findings highlight the importance of internal climate variability which seems to significantly impact long term spatial precipitation characteristics. This in turn implies that the general warming trend in the GAR (Auer et al., 2007) has either had no detectable effect on drought patterns in space, or has been masked by other non-linear and seasonally dependent processes. Caution is needed when interpreting these findings in the light of global climate change and trends of subsequent drought stages (agricultural and hydrological drought). Land surface processes come strongly into play which are directly linked to a warming trend due to increasing evapotranspiration (Duethmann and Blöschl, 2018).

The analysis of the space-time dynamics of drought development in Chapter 2 is hampered by the need for prescribing the three accumulation time scales, which are reflected in the resulting drought areas. It would be interesting to assess the duration, intensity and its seasonality as well as the spatial characteristics of drought periods without prescribing time scales to get a more objective understanding of its underlying processes. Therefore a new method of drought detection is proposed in Chapter 3 which allows for an objective analysis of drought characteristics, including drought duration, average intensity and severity. It is based on a connectivity approach where connected space-time elements of below threshold precipitation (similar to Chapter 2) are connected to a coherent region, i.e. the space-time drought event.

The skill of the method is demonstrated by examining well-known extreme droughts such as the 2003 event (Fink et al., 2004; Wetter et al., 2014), the 1921 event (Brooks and Glasspoole, 1922) and the 1946 event (Brazdil et al., 2016). The results on the temporal evolution of droughts during the last two centuries is in close agreement with previous studies that have tagged the 1940s and the period from 1850 to 1880 (the 1860s period) as drought prone time periods (e.g. van der Schrier et al., 2007; Lloyd-Hughes, 2012; Lloyd-Hughes and Saunders, 2002). With this new method it is possible to clearly distinguish these two periods from their spatio-temporal features. The 1860s show the highest values in both severity and mean intensity as well as in frequency of the major (top 5%) droughts. At the same time, the analysis of frequency stratified by duration revealed that this period shows a peak in the occurrence of long (> 6 months) droughts. In contrast, the 1940s show only slightly lower mean intensities, but severity did not peak. This is related to the low frequency of long droughts, while short (< 4 months) and intermediate (4-6 months) events show rather high frequencies. The seasonal patterns revealed a major shift of the extreme droughts from a winter/spring dominated regime in the 1860s towards an autumn regime in the 1960s, whereas the period around the 1940s shows no strong seasonality. There does not seem to exist a significant relationship between the temperature increase in the GAR and drought characteristics, although previous studies (van der Schrier et al., 2006; van der Schrier et al., 2007; Dai, 2011) did report increasing drought conditions over Central Europe during recent decades due to rising potential evapotranspiration. Trends of changing weather patterns in the mid-latitudes over the last

decades (Weusthoff, 2011) point towards an increased frequency of high pressure weather patterns over Central Europe, but this does not seem to manifest itself in more severe or more frequent droughts. Yet a significant shift in the temperature anomalies during summer droughts dependent on the spring preconditions (wet/dry) is found. Mueller and Seneviratne (2012) identified a positive relationship between preceding negative SPI values and the occurrence of hot days in Europe and other parts of the world. These and our findings suggest that soil moisture - temperature coupling is of major importance for drought development in the warm season, as it could increase drought stress through enhanced evapotranspiration.

This new dataset of objectively detected space-time drought events paved the way for an in-depth investigation of the atmospheric drivers of the extreme drought events in the last two centuries in Chapter 4. A Circulation Type (CT) classification tailored for the Alpine Region and precipitation (Schwander et al., 2017) as well as several other circulation indices (NAO, AMO, EAWR, ...) are utilized to link observed extreme drought events with atmospheric and oceanic patterns. Atmospheric circulation conditions expressed as positive Anticyclonic CT anomalies (enhanced anticyclonic activity over Central Europe) are found to be a main driver of drought conditions, which has already been noted by Kingston et al. (2015) and Trnka et al. (2009). More than one third (38%) of the variability of average event precipitation deficit can be explained by Anticyclonic CT anomaly. In winter and spring the explained variance is even higher, whereas there is no significant correlation in summer. These results point towards precipitation efficiency as another driver, which has a significant impact on precipitation deficit development. Precipitation efficiency represents the ratio between observed precipitation and expected precipitation for a particular time of year (e.g. month) and weather situation (CT). The results show generally lower precipitation efficiencies for local convection favouring CTs and events, with the peak deficit in the warm season exhibiting lower precipitation efficiency than the cold season drought events in the recent 60 years.

So far, little has been known about the drivers behind the drought decades of the 1860s and the 1940s, although the need for furthering fundamental drought understanding has been highlighted by Haslinger and Blöschl (2017). The drivers of the outstanding drought decade of the 1940s can be well explained by the processes associated with the other drought events in the entire 210 year period. The time period from 1940-1955 was dominated by strongly positive anomalies of the EAWR index in the late winters and springs, induced by positive sea surface temperature anomalies in the western subtropical Atlantic, followed by positive frequency anomalies of CTs sensitive to soil moisture-precipitation feedbacks. On the other hand, the processes driving the droughts of the 1860s are not as straightforward to understand. The global background climate during the 1860s marked the end of the Little Ice Age, a rather cold period throughout the Northern Hemisphere, with vast sea ice formation in the North Atlantic (Lamb, 1995; Vinje, 2001). The strongly positive sea level pressure anomalies during the springs of the 1860s in the North Atlantic found here may in fact have been due to sea ice formation altering the surface energy balance and inducing a thermal high near the surface, blocking the westerly flows towards Europe. This circulation feature may favour a rather

unusual southwestward propagation of cyclones from the low pressure area over Scandinavia and Western Russia.

Although the outstanding drought decades of the 1860s and 1940s were rather different in terms of their drivers, they do highlight the importance of spring as the most influential season with regards to decadal-scale drought conditions. Moreover, in both drought decades a similar above average frequency of soil moisture-precipitation feedback sensitive CTs occurred in summer, enhancing the drought signal through reduced precipitation efficiency.

However, it is not clear whether this summer circulation regime would have developed regardless of preceding dry springs, or if the atmospheric circulation is a direct consequence of the soil moisture deficit. The latter would have profound implications for future climate change, since springs are expected to become dryer (van der Linden et al., 2018) in Central Europe. Future research should explore the drought development during the warm season in more detail, particularly the transition from spring (circulation dominated) to summer (feedback dominated), since there is evidence of a feedback not only between soil moisture and convective precipitation but also with the atmospheric circulation. Furthermore, future climate projections in the Alpine Region tend to be most uncertain in their warm season precipitation signal, suggesting a further need for enhanced process understanding to better assess the robustness of climate model projections.

Chapter 2 is based on the following publication:

Haslinger K, Holawe F, Blöschl G (2018) Spatial characteristics of precipitation shortfalls in the Greater Alpine Region – a data-based analysis from observations. *Theoretical and Applied Climatology*. doi: 10.1007/s00704-018-2506-5

Klaus Haslinger conceived the study, conducted the analysis, designed the figures and wrote the text, Franz Holawe contributed to the text and analysis, Günter Blöschl contributed to the text, analysis and overall study design.

Chapter 3 is based on the following publication:

Haslinger K, Blöschl G (2017) Space-Time Patterns of Meteorological Drought Events in the European Greater Alpine Region Over the Past 210 Years. *Water Resources Research* 53:9807–9823. doi: 10.1002/2017WR020797

Klaus Haslinger conceived the study, conducted the analysis, designed the figures and wrote the text, Günter Blöschl contributed to the text, analysis and overall study design.

Chapter 4 is based on the following publication:

Haslinger K, Hofstätter M, Kroisleitner C, Schöner W, Laaha G, Holawe F, Blöschl G (2018) Disentangling drivers of meteorological droughts in the European Greater Alpine Region during the last two centuries. under review for *Journal of Geophysical Research – Atmospheres*

Klaus Haslinger conceived the study, conducted the analysis, designed the figures and wrote the text, Michael Hofstätter, Christine Kroisleitner, Wolfgang Schöner, Gregor Laaha, Franz Holawe contributed to the text and analysis, Günter Blöschl contributed to the text, analysis and overall study design.

References

- Abegg B, Jetté-Nantel S, Crick F, de Montfalcon A (2007) Climate change impacts and adaptation in winter tourism. In: Agrawala S (ed) *Climate Change in the European Alps: Adapting Winter Tourism and Natural Hazards Management*. OECD Publishing, Paris, France
- Andreadis KM, Clark EA, Wood AW, Hamlet AF, Lettenmaier DP (2005) Twentieth-Century Drought in the Conterminous United States. *J Hydrometeorol* 6:985–1001. doi: 10.1175/JHM450.1
- Auer I, Böhm R, Jurković A, Lipa W, Orlik A, Potzmann R, Schöner W, Ungersböck M, Matulla C, Briffa K, Jones P, Efthymiadis D, Brunetti M, Nanni T, Maugeri M, Mercalli L, Mestre O, Moisselin J-M, Begert M, Müller-Westermeier G, Kveton V, Bochnicek O, Stastny P, Lapin M, Szalai S, Szentimrey T, Cegnar T, Dolinar M, Gajic-Capka M, Zaninovic K, Majstorovic Z, Nieplova E (2007) HISTALP – historical instrumental climatological surface time series of the Greater Alpine Region. *Int J Climatol* 27:17–46. doi: 10.1002/joc.1377
- Auer I, Böhm R, Jurković A, Orlik A, Potzmann R, Schöner W, Ungersböck M, Brunetti M, Nanni T, Maugeri M, Briffa K, Jones P, Efthymiadis D, Mestre O, Moisselin J-M, Begert M, Brazdil R, Bochnicek O, Cegnar T, Gajić-Čapka M, Zaninović K, Majstorović Ž, Szalai S, Szentimrey T, Mercalli L (2005) A new instrumental precipitation dataset for the greater alpine region for the period 1800-2002. *Int J Climatol* 25:139–166. doi: 10.1002/joc.1135
- Barnston AG, Livezey RE (1987) Classification, Seasonality and Persistence of Low-Frequency Atmospheric Circulation Patterns. *Mon Weather Rev* 115:1083–112. doi: 10.1175/1520-0493(1987)115<1083:CSAPOL>2.0.CO;2
- Beck C, Philipp A (2010) Evaluation and comparison of circulation type classifications for the European domain. *Phys Chem Earth Parts ABC* 35:374–387. doi: 10.1016/j.pce.2010.01.001
- Beniston M (2009) Trends in joint quantiles of temperature and precipitation in Europe since 1901 and projected for 2100. *Geophys Res Lett* 36:L07707. doi: 10.1029/2008GL037119
- Bishop CM (1995) *Neural networks for pattern recognition*. Clarendon Press; Oxford University Press, Oxford: New York
- Black E, Blackburn M, Harrison G, Hoskins B, Methven J (2004) Factors contributing to the summer 2003 European heatwave. *Weather* 59:217–223. doi: 10.1256/wea.74.04
- BILkNÖ (1866) *Blätter des Vereins für Landeskunde von Niederösterreich*
- Böhm R, Auer I, Brunetti M, Maugeri M, Nanni T, Schöner W (2001) Regional temperature variability in the European Alps: 1760-1998 from homogenized instrumental time series. *Int J Climatol* 21:1779–1801. doi: 10.1002/joc.689
- Böhm R, Auer I, Schöner W, Ganekind M, Gruber C, Jurković A, Orlik A, Ungerböck M (2009) Eine neue Website mit instrumentellen Qualitäts-Klimadaten für den Großraum Alpen zurück bis 1760. *Wiener Mitteilungen* 216:7–20
- Böhm R, Auer I, Schöner W, Ungerböck M, Huhle C, Nanni T, Brunetti M, Maugeri M, Mercalli L, Gajic-Capka M, Zaninović K, Szalai S, Szentimrey T, Cegnar T, Bochnicek O, Begert M, Mestre O, Moisselin J-M, Müller-Westermeier G, Majstorović Ž (2003) Der Alpine Niederschlagsdipol – ein dominierendes Schwankungsmuster der Klimavariabilität in den Scales 100 km – 100 Jahre. *Terra Nostra* 6:61–65
- Bradford RB (2000) Drought Events in Europe. In: Vogt JV, Somma F (eds) *Drought and Drought Mitigation in Europe*. Springer Netherlands, Dordrecht, pp 7–20

-
- Brázdil R, Raška P, Trnka M, Zahradníček P, Valášek H, Dobrovolný P, Řezníčková L, Treml P, Stachoň Z (2016) The Central European drought of 1947: causes and consequences, with particular reference to the Czech Lands. *Clim Res* 70:161–178. doi: 10.3354/cr01387
- Briffa KR, van der Schrier G, Jones PD (2009) Wet and dry summers in Europe since 1750: evidence of increasing drought. *Int J Climatol* 29:1894–1905. doi: 10.1002/joc.1836
- Brönnimann S (2007) Impact of El Niño-Southern Oscillation on European climate. *Rev Geophys* 45:RG3003. doi: 10.1029/2006RG000199
- Brönnimann S, Fischer AM, Rozanov E, Poli P, Compo GP, Sardeshmukh PD (2015) Southward shift of the northern tropical belt from 1945 to 1980. *Nat Geosci* 8:969–974. doi: 10.1038/ngeo2568
- Brooks CEP, Glasspoole J (2007) The drought of 1921. *Q J R Meteorol Soc* 48:139–168. doi: 10.1002/qj.49704820205
- Brunetti M, Lentini G, Maugeri M, Nanni T, Auer I, Böhm R, Schöner W (2009) Climate variability and change in the Greater Alpine Region over the last two centuries based on multi-variable analysis. *Int J Climatol* 29:2197–2225. doi: 10.1002/joc.1857
- Brunetti M, Maugeri M, Nanni T, Auer I, Böhm R, Schöner W (2006) Precipitation variability and changes in the greater Alpine region over the 1800–2003 period. *J Geophys Res* 111:D11107. doi: 10.1029/2005JD006674
- Bueh C, Nakamura H (2007) Scandinavian pattern and its climatic impact. *Q J R Meteorol Soc* 133:2117–2131. doi: 10.1002/qj.173
- Burke EJ, Brown SJ (2008) Evaluating Uncertainties in the Projection of Future Drought. *J Hydrometeorol* 9:292–299. doi: 10.1175/2007JHM929.1
- Cai W, Zhang Y, Chen Q, Yao Y (2015) Spatial Patterns and Temporal Variability of Drought in Beijing-Tianjin-Hebei Metropolitan Areas in China. *Adv Meteorol* 2015:1–14. doi: 10.1155/2015/289471
- Chimani B, Matulla C, Böhm R, Hofstätter M (2013) A new high resolution absolute temperature grid for the Greater Alpine Region back to 1780. *Int J Climatol* 33:2129–2141. doi: 10.1002/joc.3574
- Compo GP, Whitaker JS, Sardeshmukh PD, Matsui N, Allan RJ, Yin X, Gleason BE, Vose RS, Rutledge G, Bessemoulin P, Brönnimann S, Brunet M, Crouthamel RL, Grant AN, Groisman PY, Jones PD, Kruk MC, Kruger AC, Marshall GJ, Maugeri M, Mok HY, Nordli ø., Ross TF, Trigo RM, Wang XL, Woodruff SD, Worley SJ (2011) The Twentieth Century Reanalysis Project. *Q J R Meteorol Soc* 137:1–28. doi: 10.1002/qj.776
- Dai A (2011) Characteristics and trends in various forms of the Palmer Drought Severity Index during 1900–2008. *J Geophys Res* 116:D12115. doi: 10.1029/2010JD015541
- Dai A (2013) Increasing drought under global warming in observations and models. *Nat Clim Change* 3:52–58. doi: 10.1038/nclimate1633
- Dai A, Trenberth KE, Qian T (2004) A Global Dataset of Palmer Drought Severity Index for 1870–2002: Relationship with Soil Moisture and Effects of Surface Warming. *J Hydrometeorol* 5:1117–1130. doi: 10.1175/JHM-386.1
- De Bono A, Peduzzi P, Kluser S, Giuliani G (2004) Impacts of summer 2003 heat wave in Europe. United Nations Environment Programme, Nairobi, Kenya
- Duethmann D, Blöschl G (2018) Why has catchment evaporation increased in the past 40 years? A data-based study in Austria. *Hydrol Earth Syst Sci Discuss* 1–24. doi: 10.5194/hess-2018-129

-
- Efthymiadis D, Jones PD, Briffa KR, Auer I, Böhm R, Schöner W, Frei C, Schmidli J (2006) Construction of a 10-min-gridded precipitation data set for the Greater Alpine Region for 1800–2003. *J Geophys Res* 111:D01105. doi: 10.1029/2005JD006120
- Efthymiadis D, Jones PD, Briffa KR, Böhm R, Maugeri M (2007) Influence of large-scale atmospheric circulation on climate variability in the Greater Alpine Region of Europe. *J Geophys Res* 112:D12104. doi: 10.1029/2006JD008021
- Enfield DB, Mestas-Nuñez AM, Trimble PJ (2001) The Atlantic Multidecadal Oscillation and its relation to rainfall and river flows in the continental U.S. *Geophys Res Lett* 28:2077–2080. doi: 10.1029/2000GL012745
- Findell KL, Gentine P, Lintner BR, Kerr C (2011) Probability of afternoon precipitation in eastern United States and Mexico enhanced by high evaporation. *Nat Geosci* 4:434–439. doi: 10.1038/ngeo1174
- Fink AH, Brücher T, Krüger A, Leckebusch GC, Pinto JG, Ulbrich U (2004) The 2003 European summer heatwaves and drought -synoptic diagnosis and impacts: European heatwave - impacts. *Weather* 59:209–216. doi: 10.1256/wea.73.04
- Fleig AK, Tallaksen LM, Hisdal H, Stahl K, Hannah DM (2010) Inter-comparison of weather and circulation type classifications for hydrological drought development. *Phys Chem Earth* 35:507–515. doi: <https://doi.org/10.1016/j.pce.2009.11.005>
- Gagen MH, Zorita E, McCarroll D, Zahn M, Young GHF, Robertson I (2016) North Atlantic summer storm tracks over Europe dominated by internal variability over the past millennium. *Nat Geosci* 9:630–635. doi: 10.1038/ngeo2752
- García-Herrera R, Díaz J, Trigo RM, Luterbacher J, Fischer EM (2010) A Review of the European Summer Heat Wave of 2003. *Crit Rev Environ Sci Technol* 40:267–306. doi: 10.1080/10643380802238137
- García-Herrera R, Hernández E, Barriopedro D, Paredes D, Trigo RM, Trigo IF, Mendes MA (2007) The Outstanding 2004/05 Drought in the Iberian Peninsula: Associated Atmospheric Circulation. *J Hydrometeorol* 8:483–498. doi: 10.1175/JHM578.1
- Guillod BP, Orlowsky B, Miralles DG, Teuling AJ, Seneviratne SI (2015) Reconciling spatial and temporal soil moisture effects on afternoon rainfall. *Nat Commun* 6:6443. doi: 10.1038/ncomms7443
- Giuntoli I, Renard B, Vidal JP, Bard A (2013), Low flows in France and their relationship to large-scale climate indices. *J Hyd* 482:105–118. doi: <https://doi.org/10.1016/j.jhydrol.2012.12.038>
- Hannaford J, Lloyd-Hughes B, Keef C, Parry S, Prudhomme C (2011) Examining the large-scale spatial coherence of European drought using regional indicators of precipitation and streamflow deficit. *Hydrol Process* 25:1146–1162. doi: 10.1002/hyp.7725
- Hargreaves G (1975) Moisture Availability and Crop Production. *Trans ASAE* 18:0980–0984. doi: 10.13031/2013.36722
- Hargreaves GH, Allen RG (2003) History and Evaluation of Hargreaves Evapotranspiration Equation. *J Irrig Drain Eng* 129:53–63. doi: 10.1061/(ASCE)0733-9437(2003)129:1(53)
- Haslinger K, Blöschl G (2017) Space-Time Patterns of Meteorological Drought Events in the European Greater Alpine Region Over the Past 210 Years. *Water Resour Res* 53:9807–9823. doi: 10.1002/2017WR020797
- Haslinger K, Koffler D, Schöner W, Laaha G (2014) Exploring the link between meteorological drought and streamflow: Effects of climate-catchment interaction. *Water Resour Res* 50:2468–2487. doi: 10.1002/2013WR015051

-
- Haslinger K, Schöner W, Anders I (2016) Future drought probabilities in the Greater Alpine Region based on COSMO-CLM experiments – spatial patterns and driving forces. *Meteorol Z* 25:137–148. doi: 10.1127/metz/2015/0604
- Haylock MR, Hofstra N, Klein Tank AMG, Klok EJ, Jones PD, New M (2008) A European daily high-resolution gridded data set of surface temperature and precipitation for 1950–2006. *J Geophys Res* 113:D20119. doi: 10.1029/2008JD010201
- Heim R (2002) A Review of Twentieth-Century Drought Indices Used in the United States. *Bull Am Meteorol Soc* 83:1149–1165. doi: 10.1175/1520-0477(2002)083<1149:AROTDI>2.3.CO;2
- Held IM, Soden BJ (2006) Robust Responses of the Hydrological Cycle to Global Warming. *J Clim* 19:5686–5699. doi: 10.1175/JCLI3990.1
- Hennig C (2007) Cluster-wise assessment of cluster stability. *Comput Stat Data Anal* 52:258–271. doi: 10.1016/j.csda.2006.11.025
- Herold N, Kala J, Alexander LV (2016) The influence of soil moisture deficits on Australian heatwaves. *Environ Res Lett* 11:064003. doi: 10.1088/1748-9326/11/6/064003
- Hoerling M, Eischeid J, Perlwitz J, Quan X, Zhang T, Pegion P (2012) On the Increased Frequency of Mediterranean Drought. *J Clim* 25:2146–2161. doi: 10.1175/JCLI-D-11-00296.1
- Hofstätter M, Chimani B, Lexer A, Blöschl G (2016) A new classification scheme of European cyclone tracks with relevance to precipitation. *Water Resour Res* 52:7086–7104. doi: 10.1002/2016WR019146
- Hofstätter M, Lexer A, Homann M, Blöschl G (2018) Large-scale heavy precipitation over central Europe and the role of atmospheric cyclone track types. *Int J Climatol* 38:e497–e517. doi: 10.1002/joc.5386
- Huang B, Banzon VF, Freeman E, Lawrimore J, Liu W, Peterson TC, Smith TM, Thorne PW, Woodruff SD, Zhang H-M (2015) Extended Reconstructed Sea Surface Temperature Version 4 (ERSST.v4). Part I: Upgrades and Intercomparisons. *J Clim* 28:911–930. doi: 10.1175/JCLI-D-14-00006.1
- Huntington TG, Weiskel PK, Wolock DM, McCabe GJ (2018) A new indicator framework for quantifying the intensity of the terrestrial water cycle. *J Hydrol* 559:361–372. doi: 10.1016/j.jhydrol.2018.02.048
- Intergovernmental Panel on Climate Change (ed) (2012) *Managing the risks of extreme events and disasters to advance climate change adaptation: special report of the Intergovernmental Panel on Climate Change*. Cambridge University Press, New York, NY
- Ionita M (2014) The Impact of the East Atlantic/Western Russia Pattern on the Hydroclimatology of Europe from Mid-Winter to Late Spring. *Climate* 2:296–309. doi: 10.3390/cli2040296
- Ionita M, Tallaksen LM, Kingston DG, Stagge JH, Laaha G, Van Lanen HAJ, Scholz P, Chelcea SM, Haslinger K (2017) The European 2015 drought from a climatological perspective. *Hydrol Earth Syst Sci* 21:1397–1419. doi: 10.5194/hess-21-1397-2017
- Isotta FA, Frei C, Weilguni V, Perčec Tadić M, Lassègues P, Rudolf B, Pavan V, Cacciamani C, Antolini G, Ratto SM, Munari M, Micheletti S, Bonati V, Lussana C, Ronchi C, Panettieri E, Marigo G, Vertačnik G (2014) The climate of daily precipitation in the Alps: development and analysis of a high-resolution grid dataset from pan-Alpine rain-gauge data. *Int J Climatol* 34:1657–1675. doi: 10.1002/joc.3794
- Jenicek M, Seibert J, Zappa M, Staudinger M, Jonas T (2016) Importance of maximum snow accumulation for summer low flows in humid catchments. *Hydrol Earth Syst Sci* 20:859–874. doi: 10.5194/hess-20-859-2016

-
- Jones PD, Hulme M (1996) Calculating regional climatic time series for temperature and precipitation: methods and illustrations. *Int J Climatol* 16:361–377. doi: 10.1002/(SICI)1097-0088(199604)16:4<361::AID-JOC53>3.0.CO;2-F
- Jones PD, Jonsson T, Wheeler D (1997) Extension to the North Atlantic oscillation using early instrumental pressure observations from Gibraltar and south-west Iceland. *Int J Climatol* 17:1433–1450. doi: 10.1002/(SICI)1097-0088(19971115)17:13<1433::AID-JOC203>3.0.CO;2-P
- Kaufman L, Rousseeuw PJ (2005) Finding groups in data: an introduction to cluster analysis. Wiley, Hoboken, N.J
- Kendon M, Marsh T, Parry S (2013) The 2010–2012 drought in England and Wales. *Weather* 68:88–95. doi: 10.1002/wea.2101
- Kingston DG, Lawler DM, McGregor GR (2006) Linkages between atmospheric circulation, climate and streamflow in the northern North Atlantic: research prospects. *Prog Phys Geogr* 30:143–174. doi: 10.1191/0309133306pp471ra
- Kingston DG, Stagge JH, Tallaksen LM, Hannah DM (2015) European-Scale Drought: Understanding Connections between Atmospheric Circulation and Meteorological Drought Indices. *J Clim* 28:505–516. doi: 10.1175/JCLI-D-14-00001.1
- Koster RD, Betts AK, Dirmeyer PA, Bierkens M, Bennett KE, Déry SJ, Evans JP, Fu R, Hernandez F, Leung LR, Liang X, Masood M, Savenije H, Wang G, Yuan X (2017) Hydroclimatic variability and predictability: a survey of recent research. *Hydrol Earth Syst Sci* 21:3777–3798. doi: 10.5194/hess-21-3777-2017
- Laaha G, Gauster T, Tallaksen LM, Vidal J-P, Stahl K, Prudhomme C, Heudorfer B, Vlnas R, Ionita M, Van Lanen HAJ, Adler M-J, Caillouet L, Delus C, Fendekova M, Gailliez S, Hannaford J, Kingston D, Van Loon AF, Mediero L, Osuch M, Romanowicz R, Sauquet E, Stagge JH, Wong WK (2017) The European 2015 drought from a hydrological perspective. *Hydrol Earth Syst Sci* 21:3001–3024. doi: 10.5194/hess-21-3001-2017
- Lamb HH (1995) *Climate, history, and the modern world*, 2nd ed. Routledge, London ; New York
- Lavers D, Prudhomme C, Hannah DM (2013) European precipitation connections with large-scale mean sea-level pressure (MSLP) fields. *Hydrol Sci J* 58:310–327. doi: 10.1080/02626667.2012.754545
- Lim Y-K (2015) The East Atlantic/West Russia (EA/WR) teleconnection in the North Atlantic: climate impact and relation to Rossby wave propagation. *Clim Dyn* 44:3211–3222. doi: 10.1007/s00382-014-2381-4
- Linderholm HW, Folland CK, Walther A (2009) A multicentury perspective on the summer North Atlantic Oscillation (SNAO) and drought in the eastern Atlantic Region. *J Quat Sci* 24:415–425. doi: 10.1002/jqs.1261
- Lloyd-Hughes B (2012) A spatio-temporal structure-based approach to drought characterisation. *Int J Climatol* 32:406–418. doi: 10.1002/joc.2280
- Lloyd-Hughes B, Saunders MA (2002) A drought climatology for Europe. *Int J Climatol* 22:1571–1592. doi: 10.1002/joc.846
- López-Moreno JI, Vicente-Serrano SM (2008) Positive and Negative Phases of the Wintertime North Atlantic Oscillation and Drought Occurrence over Europe: A Multitemporal-Scale Approach. *J Clim* 21:1220–1243. doi: 10.1175/2007JCLI1739.1
- Macias Fauria M, Grinsted A, Helama S, Moore J, Timonen M, Martma T, Isaksson E, Eronen M (2010) Unprecedented low twentieth century winter sea ice extent in the Western Nordic Seas since A.D. 1200. *Clim Dyn* 34:781–795. doi: 10.1007/s00382-009-0610-z

-
- Matthews JA, Briffa KR (2005) The 'little ice age': re-evaluation of an evolving concept. *Geogr Ann Ser Phys Geogr* 87:17–36. doi: 10.1111/j.0435-3676.2005.00242.x
- McKee T, Doesken N, Kleist J (1993) The Relationship of Drought Frequency and Duration Times Scales. American Meteorological Society. *Am Meteorol Soc 8th Conf Appl Climatol* 17-22 January 1993 179–184.
- Mishra AK, Singh VP (2010) A review of drought concepts. *J Hydrol* 391:202–216. doi: 10.1016/j.jhydrol.2010.07.012
- Mueller B, Seneviratne SI (2012) Hot days induced by precipitation deficits at the global scale. *Proc Natl Acad Sci* 109:12398–12403. doi: 10.1073/pnas.1204330109
- Naresh Kumar M, Murthy CS, Sessa Sai MVR, Roy PS (2009) On the use of Standardized Precipitation Index (SPI) for drought intensity assessment. *Meteorol Appl* 16:381–389. doi: 10.1002/met.136
- Nester T, Kirnbauer R, Parajka J, Blöschl G (2012) Evaluating the snow component of a flood forecasting model. *Hydrol Res* 43:762–779. doi: 10.2166/nh.2012.041
- Palmer W C (1965) *Meteorological Drought*. U.S. Department of Commerce, Washington, D. C.
- Parajka J, Blaschke AP, Blöschl G, Haslinger K, Hepp G, Laaha G, Schöner W, Trautvetter H, Viglione A, Zessner M (2016) Uncertainty contributions to low-flow projections in Austria. *Hydrol Earth Syst Sci* 20:2085–2101. doi: 10.5194/hess-20-2085-2016
- Parajka J, Blöschl G (2008) The value of MODIS snow cover data in validating and calibrating conceptual hydrologic models. *J Hydrol* 358:240–258. doi: 10.1016/j.jhydrol.2008.06.006
- Parajka J, Kohnová S, Merz R, Szolgay J, Hlavčová K, Blöschl G (2009) Comparative analysis of the seasonality of hydrological characteristics in Slovakia and Austria / Analyse comparative de la saisonnalité de caractéristiques hydrologiques en Slovaquie et en Autriche. *Hydrol Sci J* 54:456–473. doi: 10.1623/hysj.54.3.456
- Parry S, Hannaford J, Lloyd-Hughes B, Prudhomme C (2012) Multi-year droughts in Europe: analysis of development and causes. *Hydrol Res* 43:689–706. doi: 10.2166/nh.2012.024
- Patel NR, Chopra P, Dadhwal VK (2007) Analyzing spatial patterns of meteorological drought using standardized precipitation index. *Meteorol Appl* 14:329–336. doi: 10.1002/met.33
- Pekarova P, Miklanek P, Pekar J (2006) Long-term trends and runoff fluctuations of European rivers. climate variability and change – hydrological impacts. In: *Proceedings of the Fifth FRIEND World Conference, Havana*. IAHS, Havana
- Philipp A, Bartholy J, Beck C, Ericum M, Esteban P, Fettweis X, Huth R, James P, Jourdain S, Kreienkamp F, Krennert T, Lykoudis S, Michalides SC, Pianko-Kluczynska K, Post P, Álvarez DR, Schiemann R, Spekat A, Tymvios FS (2010) Cost733cat – A database of weather and circulation type classifications. *Phys Chem Earth Parts ABC* 35:360–373. doi: 10.1016/j.pce.2009.12.010
- Philipp A, Beck C, Huth R, Jacobeit J (2016) Development and comparison of circulation type classifications using the COST 733 dataset and software. *Int J Climatol* 36:2673–2691. doi: 10.1002/joc.3920
- Poirier C, Tessier B, Chaumillon É, Bertin X, Fruergaard M, Mouazé D, Noël S, Weill P, Wöppelmann G (2017) Decadal changes in North Atlantic atmospheric circulation patterns recorded by sand spits since 1800 CE. *Geomorphology* 281:1–12. doi: 10.1016/j.geomorph.2016.12.028
- Pongrácz R, Bogardi I, Duckstein L (2003) Climatic forcing of droughts: a Central European example. *Hydrolog Sci J* 48:39–50. doi: <https://doi.org/10.1623/hysj.48.1.39.43480>

-
- Rousseeuw PJ (1987) Silhouettes: A graphical aid to the interpretation and validation of cluster analysis. *J Comput Appl Math* 20:53–65. doi: 10.1016/0377-0427(87)90125-7
- Samaniego L, Kumar R, Zink M (2013) Implications of Parameter Uncertainty on Soil Moisture Drought Analysis in Germany. *J Hydrometeorol* 14:47–68. doi: 10.1175/JHM-D-12-075.1
- Scherrer SC, Begert M, Croci-Maspoli M, Appenzeller C (2016) Long series of Swiss seasonal precipitation: regionalization, trends and influence of large-scale flow. *Int J Climatol* 36:3673–3689. doi: 10.1002/joc.4584
- Schwander M, Brönnimann S, Delaygue G, Rohrer M, Auchmann R, Brugnara Y (2017) Reconstruction of Central European daily weather types back to 1763. *Int J Climatol* 37:30–44. doi: 10.1002/joc.4974
- Schwarb M (2000) The Alpine precipitation climate: Evaluation of a high-resolution analysis scheme using comprehensive rain-gauge data. Swiss Federal Institute of Technology (ETH)
- Seneviratne SI, Corti T, Davin EL, Hirschi M, Jaeger EB, Lehner I, Orlowsky B, Teuling AJ (2010) Investigating soil moisture–climate interactions in a changing climate: A review. *Earth-Sci Rev* 99:125–161. doi: 10.1016/j.earscirev.2010.02.004
- Seneviratne SI, Lüthi D, Litschi M, Schär C (2006) Land–atmosphere coupling and climate change in Europe. *Nature* 443:205–209. doi: 10.1038/nature05095
- Sheffield J, Andreadis KM, Wood EF, Lettenmaier DP (2009) Global and Continental Drought in the Second Half of the Twentieth Century: Severity–Area–Duration Analysis and Temporal Variability of Large-Scale Events. *J Clim* 22:1962–1981. doi: 10.1175/2008JCLI2722.1
- Sheffield J, Wood EF (2007) Characteristics of global and regional drought, 1950–2000: Analysis of soil moisture data from off-line simulation of the terrestrial hydrologic cycle. *J Geophys Res* 112:D17115. doi: 10.1029/2006JD008288
- Sheffield J, Wood EF (2008) Global Trends and Variability in Soil Moisture and Drought Characteristics, 1950–2000, from Observation-Driven Simulations of the Terrestrial Hydrologic Cycle. *J Clim* 21:432–458. doi: 10.1175/2007JCLI1822.1
- Sheffield J, Wood EF (2011) Drought: past problems and future scenarios. Earthscan, London ; Washington, DC
- Sheffield J, Wood EF, Roderick ML (2012) Little change in global drought over the past 60 years. *Nature* 491:435–438. doi: 10.1038/nature11575
- Sodemann H, Zubler E (2009) Seasonal and inter-annual variability of the moisture sources for Alpine precipitation during 1995–2002. *Int J Climatol* 30:947–961. doi: 10.1002/joc.1932
- Soja G, Züger J, Knoflacher M, Kinner P, Soja A-M (2013) Climate impacts on water balance of a shallow steppe lake in Eastern Austria (Lake Neusiedl). *J Hydrol* 480:115–124. doi: 10.1016/j.jhydrol.2012.12.013
- Soulé PT (1990) Spatial patterns of multiple drought types in the contiguous United States: a seasonal comparison. *Clim Res* 1:13–21
- Spinoni J, Antofie T, Barbosa P, Bihari Z, Lakatos M, Szalai S, Szentimrey T, Vogt J (2013) An overview of drought events in the Carpathian Region in 1961–2010. *Adv Sci Res* 10:21–32. doi: 10.5194/asr-10-21-2013
- Spinoni J, Naumann G, Carrao H, Barbosa P, Vogt J (2014) World drought frequency, duration, and severity for 1951–2010. *Int J Climatol* 34:2792–2804. doi: 10.1002/joc.3875
- Spinoni J, Naumann G, Vogt JV, Barbosa P (2015) The biggest drought events in Europe from 1950 to 2012. *J Hydrol Reg Stud* 3:509–524. doi: 10.1016/j.ejrh.2015.01.001

-
- Stagge JH, Kohn I, Tallaksen LM, Stahl K (2015a) Modeling drought impact occurrence based on meteorological drought indices in Europe. *J Hydrol* 530:37–50. doi: 10.1016/j.jhydrol.2015.09.039
- Stagge JH, Tallaksen LM, Gudmundsson L, Van Loon AF, Stahl K (2015b) Candidate Distributions for Climatological Drought Indices (SPI and SPEI). *Int J Climatol* 35:4027–4040. doi: 10.1002/joc.4267
- Svoboda M, LeCompte D, Hayes M, Heim R, Gleason K, Angel J, Rippey B, Tinker R, Palecki M, Stooksbury D, Miskus D, Stephens S (2002) The Drought Monitor. *Bull Am Meteorol Soc* 83:1181–1190. doi: 10.1175/1520-0477-83.8.1181
- Tallaksen LM (ed) (2006) *Hydrological drought: processes and estimation methods for streamflow and groundwater*, 1. ed., Reprint. Elsevier, Amsterdam
- Thompson DWJ, Wallace JM (1998) The Arctic oscillation signature in the wintertime geopotential height and temperature fields. *Geophys Res Lett* 25:1297–1300. doi: 10.1029/98GL00950
- Trenberth KE, Dai A, van der Schrier G, Jones PD, Barichivich J, Briffa KR, Sheffield J (2014) Global warming and changes in drought. *Nat Clim Change* 4:17–22. doi: 10.1038/nclimate2067
- Trnka M, Kyselý J, Možný M, Dubrovský M (2009) Changes in Central-European soil-moisture availability and circulation patterns in 1881–2005. *Int J Climatol* 29:655–672. doi: 10.1002/joc.1703
- Tsakiris G, Vangelis H (2005) Establishing a Drought Index Incorporating Evapotranspiration. *Eur Water* 9:9
- Tuttle SE, Salvucci GD (2017) Confounding factors in determining causal soil moisture-precipitation feedback. *Water Resour Res* 53:5531–5544. doi: 10.1002/2016WR019869
- van den Dool HM, Saha S, Johansson A (2000) Empirical Orthogonal Teleconnections. *J Clim* 13:1421–1435. doi: 10.1175/1520-0442(2000)013<1421:EOT>2.0.CO;2
- van der Linden EC, Haarsma RJ, van der Schrier G (2018) Resolution-dependence of future European soil moisture droughts. *Hydrol Earth Syst Sci Discuss* 1–31. doi: 10.5194/hess-2018-226
- van der Schrier G, Barichivich J, Briffa KR, Jones PD (2013) A scPDSI-based global data set of dry and wet spells for 1901–2009. *J Geophys Res Atmospheres* 118:4025–4048. doi: 10.1002/jgrd.50355
- van der Schrier G, Briffa KR, Jones PD, Osborn TJ (2006) Summer Moisture Variability across Europe. *J Clim* 19:2818–2834. doi: 10.1175/JCLI3734.1
- van der Schrier G, Efthymiadis D, Briffa KR, Jones PD (2007) European Alpine moisture variability for 1800–2003. *Int J Climatol* 27:415–427. doi: 10.1002/joc.1411
- Van Lanen HAJ, Laaha G, Kingston DG, Gauster T, Ionita M, Vidal J-P, Vlnas R, Tallaksen LM, Stahl K, Hannaford J, Delus C, Fendekova M, Mediero L, Prudhomme C, Rets E, Romanowicz RJ, Gailliez S, Wong WK, Adler M-J, Blauhut V, Caillouet L, Chelcea S, Frolova N, Gudmundsson L, Hanel M, Haslinger K, Kireeva M, Osuch M, Sauquet E, Stagge JH, Van Loon AF (2016) Hydrology needed to manage droughts: the 2015 European case. *Hydrol Process* 30:3097–3104. doi: 10.1002/hyp.10838
- Van Loon AF (2015) *Hydrological drought explained: Hydrological drought explained*. Wiley Interdiscip Rev Water 2:359–392. doi: 10.1002/wat2.1085
- Van Loon AF, Van Huijgevoort MHJ, Van Lanen HAJ (2012) Evaluation of drought propagation in an ensemble mean of large-scale hydrological models. *Hydrol Earth Syst Sci* 16:4057–4078. doi: 10.5194/hess-16-4057-2012

-
- Vicente-Serrano SM (2006) Differences in Spatial Patterns of Drought on Different Time Scales: An Analysis of the Iberian Peninsula. *Water Resour Manag* 20:37–60. doi: 10.1007/s11269-006-2974-8
- Vicente-Serrano SM, Beguería S, López-Moreno JI (2010) A Multiscalar Drought Index Sensitive to Global Warming: The Standardized Precipitation Evapotranspiration Index. *J Clim* 23:1696–1718. doi: 10.1175/2009JCLI2909.1
- Vicente-Serrano SM, Beguería S, Lorenzo-Lacruz J, Camarero JJ, López-Moreno JI, Azorin-Molina C, Revuelto J, Morán-Tejeda E, Sanchez-Lorenzo A (2012) Performance of Drought Indices for Ecological, Agricultural, and Hydrological Applications. *Earth Interact* 16:1–27. doi: 10.1175/2012EI000434.1
- Vicente-Serrano SM, García-Herrera R, Barriopedro D, Azorin-Molina C, López-Moreno JI, Martín-Hernández N, Tomás-Burguera M, Gimeno L, Nieto R (2016) The Westerly Index as complementary indicator of the North Atlantic oscillation in explaining drought variability across Europe. *Clim Dyn* 47:845–863. doi: 10.1007/s00382-015-2875-8
- Vinje T (2001) Anomalies and Trends of Sea-Ice Extent and Atmospheric Circulation in the Nordic Seas during the Period 1864–1998. *J Clim* 14:255–267. doi: 10.1175/1520-0442(2001)014<0255:AATOSI>2.0.CO;2
- Wang X, Wang C, Zhou W, Wang D, Song J (2011) Teleconnected influence of North Atlantic sea surface temperature on the El Niño onset. *Clim Dyn* 37:663–676. doi: 10.1007/s00382-010-0833-z
- Wells N, Goddard S, Hayes MJ (2004) A Self-Calibrating Palmer Drought Severity Index. *J Clim* 17:2335–2351. doi: 10.1175/1520-0442(2004)017<2335:ASPDSI>2.0.CO;2
- Western AW, Blöschl G, Grayson RB (1998) How well do indicator variograms capture the spatial connectivity of soil moisture? *Hydrol Process* 12:1851–1868. doi: 10.1002/(SICI)1099-1085(19981015)12:12<1851::AID-HYP670>3.0.CO;2-P
- Western AW, Blöschl G, Grayson RB (2001) Toward capturing hydrologically significant connectivity in spatial patterns. *Water Resour Res* 37:83–97. doi: 10.1029/2000WR900241
- Wetter O, Pfister C, Werner JP, Zorita E, Wagner S, Seneviratne SI, Herget J, Grünwald U, Luterbacher J, Alcoforado M-J, Barriendos M, Bieber U, Brázdil R, Burmeister KH, Camenisch C, Contino A, Dobrovolný P, Glaser R, Himmelsbach I, Kiss A, Kotyza O, Labbé T, Limanówka D, Litzenburger L, Nordl Ø, Pribyl K, Retsö D, Riemann D, Rohr C, Siegfried W, Söderberg J, Spring J-L (2014) The year-long unprecedented European heat and drought of 1540 – a worst case. *Clim Change* 125:349–363. doi: 10.1007/s10584-014-1184-2
- Weusthoff T (2011) Weather Type Classification at MeteoSwiss – Introduction of new automatic classifications schemes. *MeteoSchweiz*, Zurich, Switzerland
- Whan K, Zscheischler J, Orth R, Shongwe M, Rahimi M, Asare EO, Seneviratne SI (2015) Impact of soil moisture on extreme maximum temperatures in Europe. *Weather Clim Extrem* 9:57–67. doi: 10.1016/j.wace.2015.05.001
- Wilhite DA, Glantz MH (1985) Understanding: the Drought Phenomenon: The Role of Definitions. *Water Int* 10:111–120. doi: 10.1080/02508068508686328
- Wilks DS (2011) *Statistical methods in the atmospheric sciences*, 3rd ed. Elsevier/Academic Press, Amsterdam ; Boston
- Zargar A, Sadiq R, Naser B, Khan FI (2011) A review of drought indices. *Environ Rev* 19:333–349. doi: 10.1139/a11-013
- Zhai J, Huang J, Su B, Cao L, Wang Y, Jiang T, Fischer T (2017) Intensity–area–duration analysis of droughts in China 1960–2013. *Clim Dyn* 48:151–168. doi: 10.1007/s00382-016-3066-y